



HAL
open science

Contribution to fluorescence microscopy, 3D thick samples deconvolution and depth-variant PSF

Elie Maalouf

► **To cite this version:**

Elie Maalouf. Contribution to fluorescence microscopy, 3D thick samples deconvolution and depth-variant PSF. Other. Université de Haute Alsace - Mulhouse, 2010. English. NNT : 2010MULH2458 . tel-00594247

HAL Id: tel-00594247

<https://theses.hal.science/tel-00594247>

Submitted on 19 May 2011

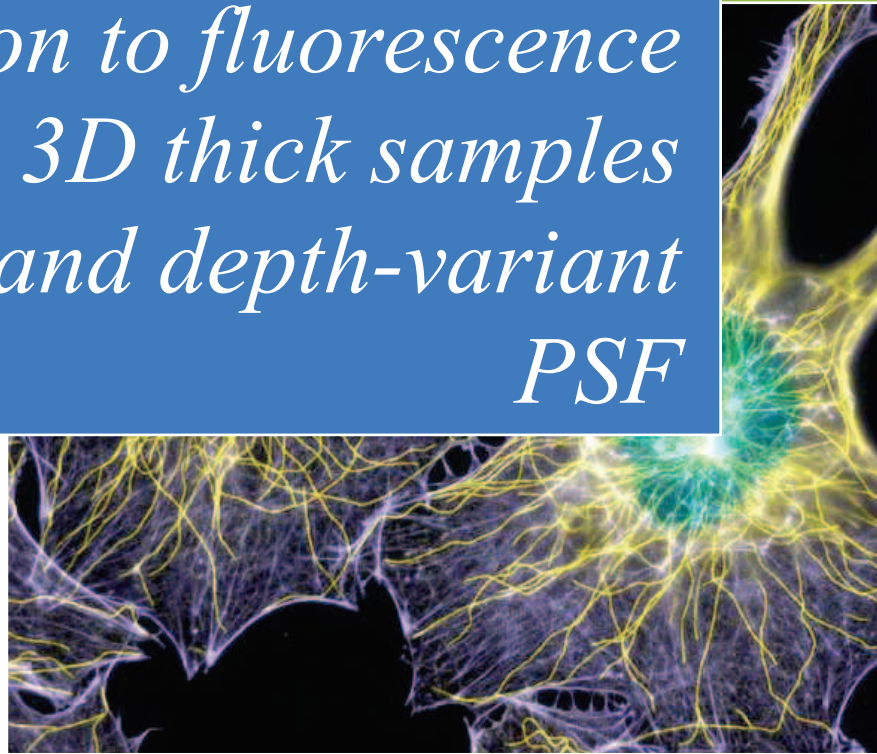
HAL is a multi-disciplinary open access archive for the deposit and dissemination of scientific research documents, whether they are published or not. The documents may come from teaching and research institutions in France or abroad, or from public or private research centers.

L'archive ouverte pluridisciplinaire **HAL**, est destinée au dépôt et à la diffusion de documents scientifiques de niveau recherche, publiés ou non, émanant des établissements d'enseignement et de recherche français ou étrangers, des laboratoires publics ou privés.



Defended
The
20th of December
2010

*Contribution to fluorescence
microscopy, 3D thick samples
deconvolution and depth-variant
PSF*



THESIS

*to fulfill the requirements
for the degree of
Ph.D. in Signal
Treatment – E.E.A
from
Haute Alsace University*

Supervised by:
DIETERLEN Alain
COLICCHIO Bruno

Presented by:
MAALOUF Elie.

JURY :

*Mme Laure Blanc-Féraud, Directrice de
recherche au CNRS, rapporteur*

*M. François Goudail, Professeur des universités
à l'Institut d'Optique Graduate School / LCFIO,
équipe Spectro-Imagerie, rapporteur*

*M. Eric Thiebaut, CRAL/CNRS-UMR 5574,
observatoire de Lyon, rapporteur*

*M. Yves Usson, Chargé de Recherche au
laboratoire TIMC, UMR5525 à Grenoble*

*M. Michel Hassenforder, Professeur des
Universités à l'UHA*

*M. Bruno Colicchio, Maître de Conférences à
l'UHA, co-encadrant de thèse*

*M. Alain Dieterlen, Professeur des Universités
à l'UHA, Directeur de thèse*

Joy in looking and comprehending is nature's most beautiful gift.

Albert Einstein

ACKNOWLEDGEMENTS

I would like to express firstly my sincerest gratitude to Prof. Alain DIETERLEN for believing in my abilities and for his guidance, despite his busy engagement, in the scientific work or in resolving the even more challenging administrative problems. None of this work could be done without the constant support and friendship of Bruno Colicchio, to whom I can't but to offer an eternal gratitude and enormous respect as a mentor, friend and colleague.

I thank also the Alsace region for financing my thesis during three years, and I offer this work as a small contribution for the advancement of science in Alsace and France.

I thank my parents for their uninterrupted support and total trust in me, which always gave me the needed force to keep going and always go further; my brothers for their financial and moral help; my sister for being my confidence and advisor in the strange world of human relationships.

My life as a graduate student wouldn't be easy to bear without the support of my colleagues, whom I consider as my second family, and I thank Olivier Haeberlé (with the French é) for his constructive critics, Matthieu Debailleul for his support and explanations about optics, Damien Lefloch for his most treasured friendship and the countless interesting conversations we had, Merdan Sarmis and Jerome dhollande for their repetitive "positive attitude" shots. Not to forget Sacha Bernet, Bertrand Simon, Christophe Cudel, Sophie Kohler, Arnaud De Meyer and Jonathan Bailleul.

ABBREVIATIONS

2D:	Two dimensions
3D:	Three dimensions
COSM:	Computational Optical Sectioning Microscopy
DIC:	Differential Interference Contrast
DIV:	Depth InVariant
DV:	Depth Variant
EMMA:	Evolutionary Merging Mask Algorithm
FFT:	Fast Fourier Transform
GPU:	Graphical Processing Unit
IMMSI:	Imagerie Microscopique Multidimensionnelle et Systèmes d'Information
JNI:	Java Native Interface
JVC:	Jansson-Van Cittert
JVM:	Java Virtual Machine
LLS:	Linear Least Square
LUT:	LookUp table
MAP:	Maximum A Posteriori
MIPS:	Modélisation Intelligence Processus Systèmes
ML-EM:	Maximum-Likelihood Expectation-Minimisation
MPL:	Maximum-Penalized-Likelihood
OTF:	Optical Transfer Function
PALM:	Photo-Activated Localization Microscopy
POCS:	Projection Onto Convex Sets
PSF:	Point Spread Function
RLLS:	Regularized Linear Least Square
SIM:	Structured Illumination Microscopy
SNR:	Signal to Noise Ratio
STED:	Stimulated Emission Depletion
STORM:	STochastic Optical Reconstruction Microscopy
TIRF:	Total Internal Reflection Fluorescence

TABLE OF FIGURES

Chapter 1

Fig. 1: Jablonski Diagram of fluorescence phenomenon.....	6
Fig. 2: COSM (Computational Optical Sectioning Microscopy) acquiring process.....	6
Fig. 3: BX51 Commercial wide field fluorescence microscope (Olympus).....	7
Fig. 4: The object image is a collection of multiple point-like light sources images.....	8
Fig. 5: Image formation illustration in a wide field microscope.....	8
Fig. 6: Theoretical PSF and a measured PSF.....	9
Fig. 7 : OTF (Optical Transfer function) of a wide field microscope.....	9
Fig. 8: Image formation illustration in a confocal microscope.....	11
Fig. 9: Selectively excite fluophores using the evanescent light. (from Nikon).....	13
Fig. 10: STED principle. (From Zeiss ressource center).....	15
Fig. 11: PALM single-molecule localization procedure.....	16
Fig. 12: PALM single-molecule localization along the optical axis.....	17
Fig. 13 : Structured illumination Microscopy principle.....	18

Chapter 2

Fig. 1: PSF calculated for a wide field microscope at different depths.....	37
Fig. 2: Example of a mask.....	41
Fig. 3: Example of a set of 6 masks for a deconvolution with 6 PSF.....	42
Fig. 4: synthetic objects and the acquisitions simulation.....	43
Fig. 5: Intensity profiles into the object space and in the image space (beads).....	44
Fig. 6: Intensity profiles into the object space and in the image space (parallelepiped).....	44
Fig. 7: Correlation coefficient variations between a reference PSF and each PSF at different depths.....	46
Fig. 8: Restoration using LLS in the depth invariance PSF assumption Vs Restoration using EMMA associated with LLS algorithm and 7 PSF at different depths.....	47
Fig. 9: Intensity profiles of Restoration using LLS and the depth invariance PSF assumption and restoration using EMMA associated with LLS algorithm and 7 PSF (beads).....	48
Fig. 10: Intensity profiles of restoration using LLS and restoration using EMMA associated with LLS algorithm and 7 PSF (parallelepiped).....	48
Fig. 11: Restoration using Lucy-Richardson with the depth invariance PSF assumption and Restoration using EMMA associated with Lucy-Richardson method and 7 PSF.....	50
Fig. 12: Intensity profiles of Restoration using LR and the depth invariance assumption and restoration using EMMA associated with LLS algorithm and 7 PSF (beads).....	51
Fig. 13: Intensity profiles of restoration using LR and restoration using EMMA associated with LLS algorithm and 7 PSF (parallelepiped).....	51
Fig. 14: Automatic iteration number for iterative algorithms associated with EMMA.....	54

Chapter 3

Fig. 1: The mapping transform between Cartesian coordinate of an image to polar coordinates	61
Fig. 2: 3D PSF representation.....	63
Fig. 3: Zernike polynomials in the unit circle for various order and repetition	64
Fig. 4: Four Zernike moments variations over the 17th plane and the 32, along the depth.	66
Fig. 5: Reconstruction of a PSF at 0 μ m of depth using pseudo-3D Zernike moments up to order 45.	68
Fig. 6: Reconstruction of a PSF at 10 μ m of depth using pseudo-3D Zernike moments up to order 45.	69
Fig. 7: Correlation coefficient as function of polynomial fitting order used (1-8).	70
Fig. 8: Correlation coefficient as a function of PSF depth, between Interpolated PSF and calculated one.	71
Fig. 9: Correlation coefficient as a function of PSF depth between used PSF and calculated one	72
Fig. 10: Interpolated PSF at 7 μ m using 6 known PSF.....	72
Fig. 11: The changes in the refractive index of the imaging medium can affect how light rays are captured by the objective. (Used from www.microscopyu.com - nikon).	73
Fig. 12: Effect of temperature variation of 10 $^{\circ}$ c over a PSF at 1 μ m	74
Fig. 13: Theoretical PSF and Interpolated PSF at 18 $^{\circ}$ c. and 30 $^{\circ}$ c.	74

Chapter 4

Fig. 1: Deconvolution with a non-invariant assumption using Lucy-Richardson	79
Fig. 2: Calculated PSF at 5 μ m with 20dB SNR (central planes).	80
Fig. 3: Normalized intensities profiles of original object vs. depth invariant deconvolution result	80
Fig. 4: Result of EMMA deconvolution associated with Lucy-Richardson	81
Fig. 5: Normalized intensities profiles comparing EMMA deconvolution with the original objects	81
Fig. 6: Zernike interpolation process	82
Fig. 7: EMMA deconvolution result using Lucy-Richardson with Zernike interpolation	83
Fig. 8: Normalized intensities profiles comparing an EMMA deconvolution using prior Zernike interpolation with the original object (5 PSF input).	83
Fig. 9: Acquired data showing isolated beads for PSF extraction and aggregates assimilated to cells phantoms.	85
Fig. 10: Extracted PSF at relative depth of 4 μ m and 25.75 μ m.....	85
Fig. 11: Extracted object, shown as an average intensity projections (along Z and Y).	86
Fig. 12: Interpolated PSF at relative depth 18.25 μ m compared to the measured one.....	87
Fig. 13: Interpolated PSF at relative depth 22.75 μ m compared to the measured one.....	87
Fig. 14: Intensity profiles comparing the measured PSF at 18.25 μ m and the interpolated one.....	88
Fig. 15: Intensity profiles comparing the measured PSF at tposition 22.75 μ m and the interpolated one....	88
Fig. 16: Histogram of the acquired image background.....	89
Fig. 17: The original object shown in intensity average projection mode and 3D surface view mode.	90
Fig. 18: Result of a deconvolution using LLS in a PSF non-invariance assumption.	91
Fig. 19: Result of EMMA deconvolution associated with LLS algorithm	92
Fig. 20: Deconvolution result using EMMA associated with LLS after using zernike interpolation.	93

Conclusion

Fig. 1: PSF set acquired using a microscope.....	96
--	----

Table of Contents

<i>Acknowledgements</i>	III
<i>TABLE OF FIGURES</i>	V
<i>Introduction</i>	1
1. <i>Amelioration in 3D optical fluorescence microscopy</i>	5
1.1 <i>Introduction</i>	5
1.2 <i>Hardware modifications</i>	11
1.2.1. <i>Diffraction limited amelioration</i>	11
1.2.2. <i>High resolution solutions</i>	14
1.2.3. <i>Discussion on hardware enhancement techniques</i>	18
1.3 <i>Deconvolution techniques</i>	19
1.3.1 <i>Direct inversion methods</i>	20
1.3.2 <i>Iterative methods</i>	23
1.3.3 <i>Blind deconvolution</i>	29
1.4 <i>Conclusion</i>	31
1.5 <i>References</i>	33
2. <i>Space variant PSF deconvolution</i>	36
2.1. <i>Introduction</i>	36
2.2. <i>PSF non-invariance</i>	37
2.3. <i>available Non-Invariance solutions</i>	38
2.4. <i>EMMA – Evolutive Merging Masks Algorithm</i>	40
2.4.1. <i>Merging Mask</i>	40
2.5. <i>Test and results</i>	42
2.5.1. <i>Restoration</i>	45
2.5.2. <i>EMMA Optimization</i>	52
2.6. <i>Conclusion</i>	55
2.7. <i>References</i>	56
3. <i>Zernike interpolation</i>	57
3.1. <i>Introduction</i>	57
3.2. <i>PSF extraction methods</i>	58
3.3. <i>PSF representation with Zernike Moments</i>	59
3.3.1. <i>General moment theory</i>	59
3.3.2. <i>Zernike moments descriptors</i>	60
3.3.3. <i>Describing PSF with Zernike moments</i>	63

3.4.	<i>Analysis of moments variations</i>	65
3.5.	<i>Polynomial Fitting and interpolation</i>	67
3.6.	<i>Discussion and results</i>	68
3.6.1.	<i>Pseudo-3D reconstruction</i>	68
3.6.2.	<i>Fitting order</i>	69
3.6.3.	<i>Interpolation</i>	71
3.7.	<i>Zernike Interpolation for other optical parameters:</i>	73
3.8.	<i>Conclusion and perspective</i>	75
3.9.	<i>References:</i>	76
4.	<i>EMMA-Zernike combination (simulation and practical application)</i>	78
4.1.	<i>Introduction</i>	78
4.2.	<i>Simulation</i>	78
4.3.	<i>Acquired data application</i>	84
4.3.1.	<i>Sample preparation</i>	84
4.3.2.	<i>Acquisition</i>	84
4.3.3.	<i>Zernike interpolation test</i>	86
4.3.4.	<i>Image restoration testS</i>	89
4.4.	<i>Conclusion</i>	94
5.	<i>Conclusion and perspectives</i>	95
	<i>Scientific works</i>	98
	<i>International conferences</i>	98
	<i>National conferences</i>	98
	<i>Posters</i>	98
	<i>Publications</i>	98

INTRODUCTION

*CONCERN FOR MAN AND HIS FATE MUST ALWAYS FORM THE
CHIEF INTEREST OF ALL TECHNICAL ENDEAVORS. NEVER
FORGET THIS IN THE MIDST OF YOUR DIAGRAMS AND
EQUATIONS.*

ALBERT EINSTEIN

Since the birth of optical microscopy, using visible light and a set of lenses, many techniques were developed in the last decades in order to increase the contrast and the resolution of the object, giving birth to different specialized optical microscopes. In the 80's a technique called "fluorescence microscopy" has spread widely in reason of practical biologic applications, relying on the fluorescence phenomena to acquire only structures of interests.

The Fluorescent light microscope is used to observe living cells, allowing the biologists to study their mechanisms. Furthermore, the imaging of translucent specimen permits to record a series of optical sections, that can be combined computationally in order to visualize the three dimensional structures of the sample. The spatial resolution of optical microscopes is limited as the microscope acts as a low pass filter, which introduces blur in the resulting image. As a matter of fact in a 3D acquisition, the intensities spreading from the out-of-focus light coming from neighbor planes are recorded in the in-focus plane. The 3D imaging process can be mathematically modeled as a convolution product of the real object and the system's Point Spread Function (the system's impulse response). Many techniques have been investigated to reduce the blurring effect and gain in resolution, either by modifying the hardware design or by applying imagery treatment techniques. The later, is known as deconvolution techniques, a kind of inverse problem. Deconvolution is a computational technique used to reverse the effects of intensities spreading, but the ill-posed nature of the deconvolution problem leads to a non-unique solution. A variety of methods were developed, considering more or less prior knowledge on the restored object and different noise statistics. In most methods, the PSF is assumed to be shift invariant into the object space, allowing the use of Toeplitz matrix representation of the PSF or the use of fast Fourier transform (FFT) to perform fast convolution process, permitting their use in commercial systems. This assumption cannot be maintained, especially with thick data, as the PSF presents large variations with depth.

Introduction

When the system is non-invariant and the specimen is thick, the use of deconvolution methods that take into account the PSF variation, is limited by the processing time and the knowledge of a PSF for each position in the volume.

In theory, all methods based on the use of a convolution product can be applied, using a non-invariant convolution kernel by doing a spatial point-to-point convolution. However with the increase of the 3D data volume, the computation load would be extremely heavy and the processing time won't be acceptable without the use of a super-calculator, hence all developed methods cannot hold the non-invariance condition.

The second problem is a practical limitation. A mathematical model permits to calculate a PSF for any position in the volume, but don't incorporate all system's aberration and the deconvolution is affected by this approximation. Meanwhile a measured PSF is hard to obtain at any position, and their usual limited number is not enough in order to perform a non-invariant deconvolution.

In practice, a deconvolution method that takes into account the non-invariance condition should:

- use a limited set of acquired PSF.
- have an acceptable processing time using laboratories every day computers.
- be adapted to the image acquisition conditions
- use well established deconvolution algorithms, stable and known by users.

In this context, the aim of this thesis is to give a practical approach to the non-invariance problem in fluorescence imagery deconvolution. We propose to ameliorate the imagery treatment techniques by taking into account the PSF variation, using any classical methods, without modification of the later. We also propose a method which interpolates PSF using few measured ones giving the ability to obtain PSF at any position needed, yielding better estimation when using our space-varying PSF deconvolution algorithm or the first proposed method.

To expose this work, the manuscript is divided into four chapters. The first chapter presents an overview of hardware ameliorations and computational techniques that can ameliorate the contrast and the resolution of a fluorescence microscope. The hardware amelioration techniques can be easily understood if the fluorescence microscope is decomposed into two functional blocks: the illumination block and the detection block. Then the amelioration

Introduction

techniques can be classified according to the concerned block. Classical deconvolution methods are also presented as a prerequisite for the proposed method. Classical deconvolution algorithms (LLS, Lucy-Richardson, Jansson-Van Cittert) are implemented as an ImageJ plugins coupled with JNI (Java Native Interface) to optimize computation speed. These deconvolution methods are usable with the proposed EMMA (Evolutive Merging Mask Algorithm) whose principle is exposed in the second chapter.

The second chapter details the novel method to adapt all non-blind deconvolution algorithms presented in the first chapter, without any modification, to be a solution for non-invariance problem. We propose a simple, but efficient method, that when associated with any deconvolution algorithm and a set of PSF at different positions, it becomes an effective solution for the depth variant PSF deconvolution. It is shown that this approach gives the flexibility to choose the algorithm for the existing data accordingly to the application needs. Tests are performed using two algorithms representing a direct inversion and an iterative one. These tests are carried on simulated data having the advantage of knowing the original object, hence the possibility to quantify the restoration quality. It is also shown that the restored image quality highly depend on the number of PSF used by the process. The EMMA method can either use a single PSF, transforming the case into a classical space invariant deconvolution, or up till a PSF for each slice which yield the best results.

The chapter three presents a PSF interpolation method based on Zernike moments and polynomial fitting. The method is tested on synthetic data with and without noise. As measuring PSF at various depths can be a complicated task, some techniques attempt to adjust the parameters of a mathematical model to be as close as possible to the actual measurement values by recovering data from an experimental PSF, others propose a simplified model with a restrained set of parameters that can be adjusted using few measured PSF. Nevertheless, measuring the PSF is still the method of choice to capture the maximum of the true system's aberrations, many authors propose various methods to achieve variant PSF measurements but these techniques offer a limited number of randomly positioned PSF. In order to obtain more relatively accurate PSF from a limited number of known ones at a variable depth, we propose an interpolation technique that allows the estimation of PSF at various positions. This technique provides the necessary PSF for optimal deconvolution results in a non-invariance assumption using a minimal number of measured PSF.

As a simple interpolation technique may not be accurate enough in order to reflect the true aberration changes of the PSF, the proposed method quantifies the variation of the PSF by decomposing the image into a set of descriptors representing the PSF properties using Zernike moments. This technique allows also studying the variation of PSF along the depth.

Introduction

Furthermore Zernike interpolation may also be used to study and interpolate other parameter's variation, such as emission wavelength or oil refractive index. As an example, the technique is applied on immersion oil refractive index change with the temperature using simulated data.

In chapter 4, the complete framework including non-invariant deconvolution and PSF interpolation is conducted on real acquired data. The interpolation technique is tested with measured PSFs using 100nm fluo-beads imbedded in polymers. The beads sample was designed in collaboration with the Mulhouse DPG (Département de Photochimie Générale) during a previous thesis in MIPS laboratory (Arnaud De Meyer). We acquired PSF at various depths using this special sample; these beads were used to validate the Zernike interpolation process. Interpolated PSF are compared with the measured one using qualitative and quantitative methods. EMMA is then associated with Zernike interpolation process and the entire solution is validated over simulated and measured data; Cells phantom-like object is extracted from the same sample as the PSF and are used to validate EMMA and EMMA-Zernike interpolation solution, where qualitative comparisons are performed and we show that a better resolution is obtained. The EMMA-Zernike interpolation solution was implemented as ImageJ PlugIn and associated with LLS (Preza) algorithm.

We conclude on the EMMA capabilities: the algorithm offers a simple and efficient solution for depth variant PSF deconvolution. The results quality depend on the number of known PSF used, their quality and their spreading along the object's depth. It is not always possible to acquire enough PSF that satisfy those requirements, in such cases, Zernike interpolation become a complementary solution to obtain satisfactory results. The entire proposed image processing techniques was evaluated in this work combining EMMA and Zernike interpolation on simulated data using restrained PSF number with a low SNR, and also on measured data. Some future works are proposed. First, some optimization could be expected from the use of advanced numerical methods in order to compute higher order of Zernike moments. We will propose also to apply the interpolation of PSF on other microscope setting parameters modifying the PSF.

1. AMELIORATION IN 3D OPTICAL FLUORESCENCE MICROSCOPY

A PERFECTION OF MEANS, AND CONFUSION OF AIMS,
SEEMS TO BE OUR MAIN PROBLEM.
ALBERT EINSTEIN

1.1 INTRODUCTION

Optical microscopy was designed around year 1600; using visible light and a set of lenses, it magnifies objects of interests at the micrometer scale invisible by the naked eye.

Over the years, many techniques were developed in order to increase the contrast and the resolution of the object, giving birth to different specialized optical microscopes. The contrast in this context is defined as the ability to differentiate between what is considered as the objects of interest (signal) and what is not (the background). As for resolution it is defined as the ability to of the imaging system to resolve fine details in the observed object.

In the 80's a technique called "fluorescence microscopy" has spread widely in reason of practical biologic applications. The fluorescence microscopy relies on the fluorescence phenomena to acquire only structures of interests, naturally fluorescent, or marked by fluorophores, rendering this technique a powerful functional imaging system. The fluorescence is a phenomenon in which a substance emits light of a certain wavelength only under and during stimulation or excitation by chromatic light or other forms of electromagnetic radiations (Fig. 1). Usually the emitted light has a greater wavelength than the excitation one, according to Stokes's law.

Chapter 1

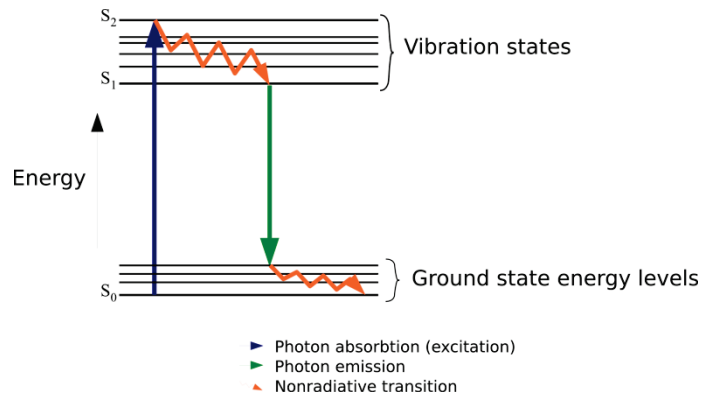


FIG. 1: A JABLONSKI DIAGRAM OF FLUORESCENCE PHENOMENON

Each fluorophore is characterized by its absorption (excitation) and emission spectrum which make it possible to make multiple and specific marking of many sites of interest using different fluorophores and to choose between them using a set of filters.

The fluorescence microscope by design is a 2D acquisition system. The specimen under study is excited using an excitation block and the emitted light is recorded using a detection block. By moving the focal plane along the Z axis, across the specimen, one can record a set of 2D digital images and render them as a 3D representation of the specimen. This technique is called the Computational Optical Sectioning Microscopy (COSM - Fig. 2). The axial sweeping can be made either by moving the object or by moving the objective, generally with a piezoelectric device.

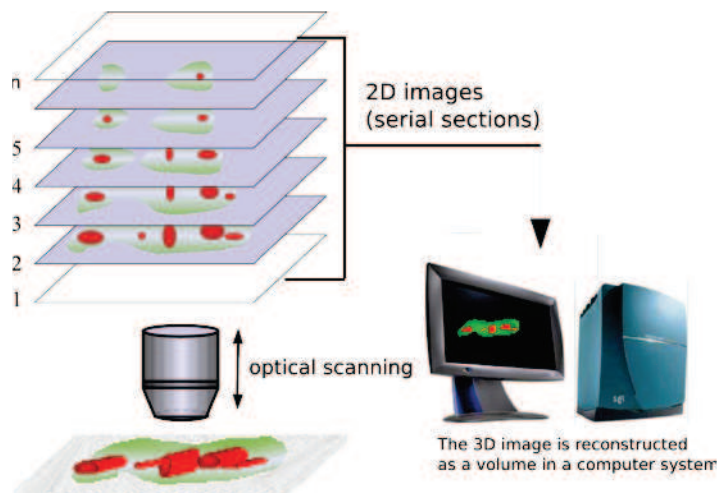


FIG. 2: COSM (COMPUTATIONAL OPTICAL SECTIONING MICROSCOPY) ACQUIRING PROCESS

Chapter 1

The basic most common setup of fluorescence microscopy is illustrated in Fig. 3, (Wide Field fluorescence microscopy). The entire specimen volume is excited at the same time using a mercury lamp producing incoherent white light and a set of filters allowing the choice of the excitation wavelength; a dichroic mirror reflects the excitation light onto the specimen and let through the emitted light by fluorescence, this light is selected by the filters set in the detection block and recorded using a CCD camera.

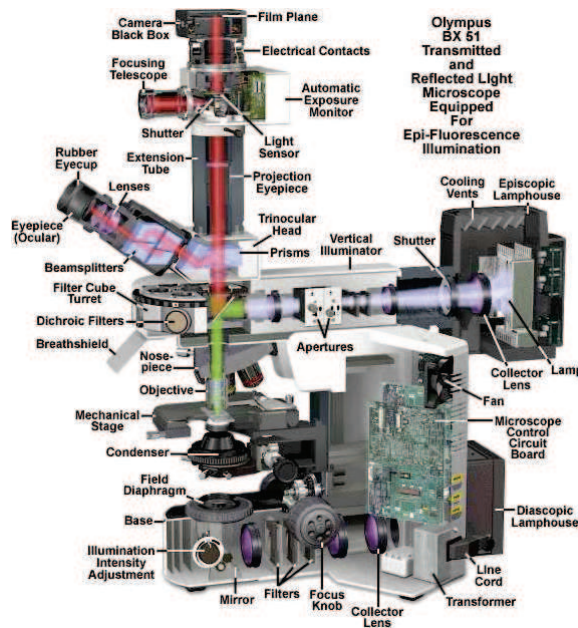


FIG. 3: BX51 COMMERCIAL WIDE FIELD FLUORESCENCE MICROSCOPE (OLYMPUS)

The images acquired using fluorescence microscopes (2D or 3D) suffer from blurring effect. This drawback may not be important when studying the specimen only from a functional point of view, but it may become a problem for quantitative studying of the specimen morphology as its real intensities localization can be more or less modified by the optical system. In order to understand the blurring phenomena and ameliorate the acquired data one should study and examine the image formation process while a 3D acquisition in such optical system.

As the object is seen as a result of fluorescence emission, then it can be considered as a collection of independent punctual light sources emitting an incoherent monochromatic light, thereby the image is the sum of the images of these punctual light sources (Fig. 4).

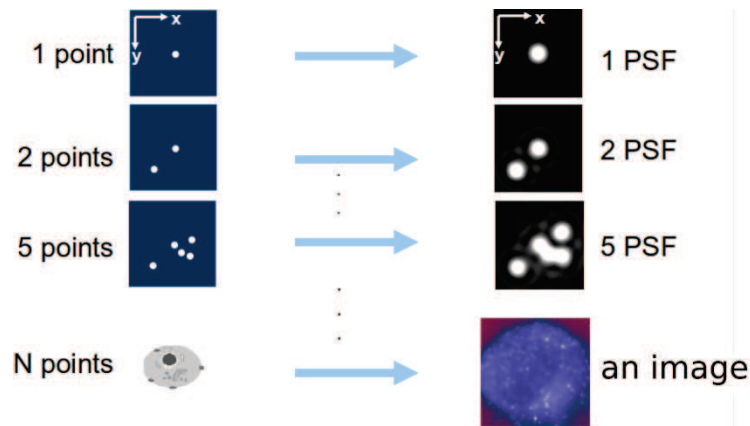


FIG. 4: THE OBJECT IMAGE IS A COLLECTION OF MULTIPLE POINT-LIKE LIGHT SOURCES IMAGES

The image of a point source is never a point, the reason is that the finite numerical aperture of the objective lens fails to collect all of the light emitted from the point source and consequently cannot form a perfect image, moreover the objective aperture introduces diffraction patterns into the image. The acquired image is blurred by the contribution of light from the out of focus sections as illustrated by Fig. 5.

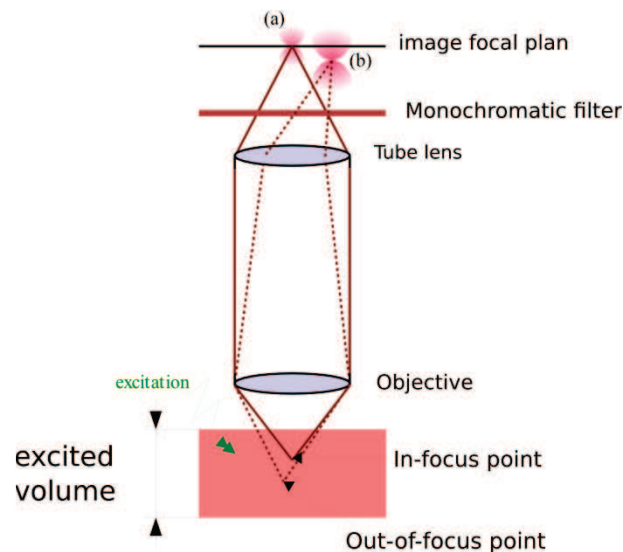


FIG. 5: IMAGE FORMATION ILLUSTRATION IN A WIDE FIELD MICROSCOPE. EFFECT OF OUT-OF-FOCUS POINTS ON IMAGE FORMATION IN THE FOCAL PLANE.

Thereby instead of having a clean point-like image, one record the transfer function of the optical system also known as the Point Spread Function (PSF) of the system. In 3D, the PSF have the shape of a double cone structure modulated by diffraction ring pattern and having their apexes united at the point source, rendering an hourglass shape. Fig. 6 shows a measured PSF (Fig. 6, a'), b') with a wide field microscope having an oil immersed objective with 100X magnification, numerical aperture of 1.4, oil refractive index of 1.515 and emission wavelength of 515nm; the beads used have a diameter of 200nm.

Next to it (Fig. 6, b, b')) one can see a calculated PSF with same parameters using the Gibson-Lani model.

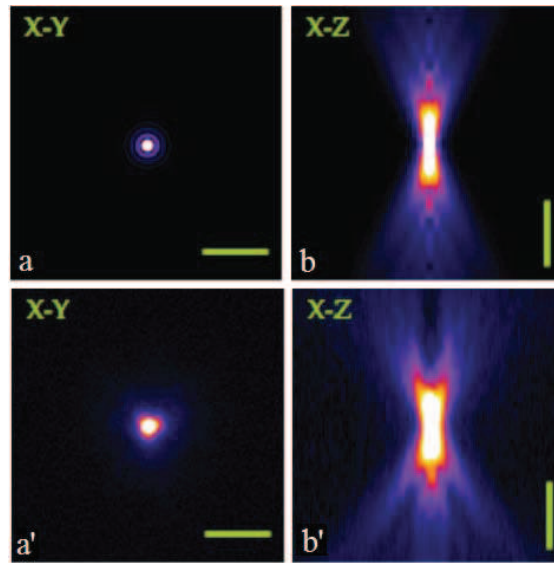


FIG. 6: THEORETICAL PSF ($a - b$) CALCULATED USING GIBSON AND LANNI MODEL FOR A WIDE FIELD MICROSCOPE AND A MEASURED PSF ($a' - b'$)

The Fourier transform of a PSF represents the frequencies recorded by the optical system and is called the Optical Transfer Function (OTF). The Fig. 7 shows the OTF of a wide field fluorescence microscope, one can notice the limited set of frequencies along the lateral axis due to the limited numerical aperture of the objective, as for the optical axis one can notice a large set of missing frequencies called the missing cone, which will have a strong repercussion on the axial resolution.

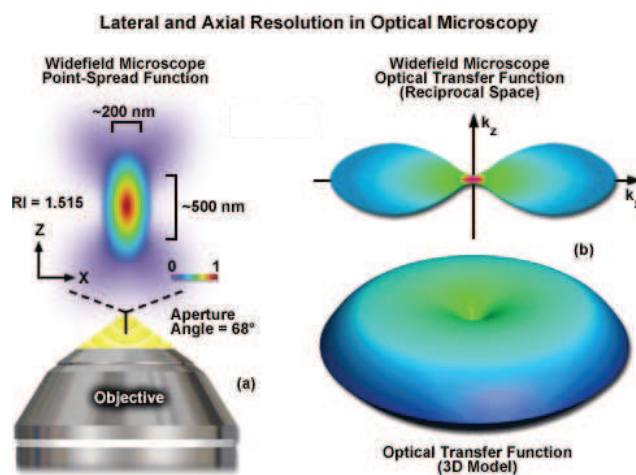


FIG. 7 : OTF (OPTICAL TRANSFER FUNCTION) OF A WIDE FIELD MICROSCOPE. ONE CAN NOTICE THE MISSING CONE OF FREQUENCIES. (FROM ZEISS RESSOURCE CENTER)

Mathematically the 3D acquired image can be modeled as a convolution

$$g(s) = \int_{\Omega} h(s, s-t) f(t) dt + n(s) \quad (1.1)$$

Where the spatial coordinates are $s \in \mathfrak{R}^3$ and $t \in \mathfrak{R}^3$, Ω is a closed region containing the image domain. The function g is the measured image; usually known only for certain discrete values of s . the image $g(s)$ is the result of blurring the unknown true image with the PSF $h(s)$ in addition to some noise.

Many techniques have been investigated to reduce the blurring effect and gain in resolution, either by modifying the hardware design or by applying imagery treatment techniques. Along this chapter we will discuss, in an overview, these hardware changes and software techniques that can ameliorate the contrast and the resolution in the fluorescence microscopy.

The aim of this thesis is to ameliorate the imagery treatment techniques by taking into account the PSF variation into the object space, a parameter rarely taken into consideration by the classical techniques. We also propose a method which interpolates PSF using few measured ones which yield a better estimation when using a space-varying PSF deconvolution algorithm.

In this first section we present an overview of various fluorescence microscope modifications and different numerical techniques for image restoration.

1.2 HARDWARE MODIFICATIONS

In order to ameliorate the acquired data quality using the hardware means, one should try to reduce the system's PSF size (the ideal case being a point like) by limiting the contribution of the out of focus slices or capturing more frequencies in Fourier domain.

1.2.1. DIFFRACTION LIMITED AMELIORATION

1.2.1.1 CONFOCAL MICROSCOPE

In 1953, Marvin Minsky described the principles of confocal microscopy [1], but the first commercial confocal microscope didn't exist until late 1980[2].

The confocal microscope illuminates with a focused laser beam to stimulate only a limited part of the specimen, and a symmetrically arranged point detector in the detection block, called the pinhole, is used to exclude out-of-focus background fluorescence from detection. Fig. 8 illustrates such system.

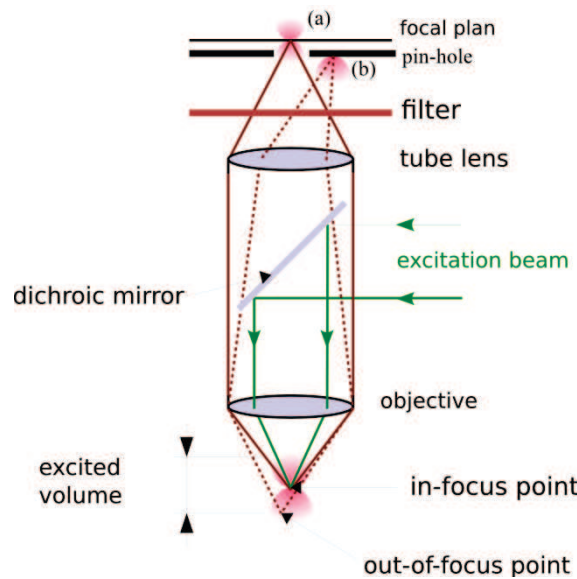


FIG. 8: IMAGE FORMATION ILLUSTRATION IN A CONFOCAL MICROSCOPE. THE EXCITED VOLUME IS REDUCED AND A PIN-HOLE REJECTS THE OUT-OF-FOCUS LIGHT.

The excitation beam is focused through the optical system thereby it is also subject to diffraction and the stimulation point is a diffraction pattern, then the effective PSF of the microscope is actually the product of the diffraction patterns for illumination and detection. In a general assumption, the illumination and detection patterns are identical and the resulting PSF is the detection PSF squared. This quadratic dependency on the intensity reduces the size of the central spot, furthermore the convolution in the Fourier domain expands the optical bandwidth of spatial frequencies.

In practice, the illumination and detection patterns are not really identical (the emission and detection wavelengths are not the same) and the detector is not point-like [3], thereby the multiplication result is not actually a squared PSF.

By design the confocal microscope needs to scan the entire specimen in order to acquire a full image, making a 3D acquisition a lengthy process not suitable for imaging live cells in evolution. The potentially high power excitation laser beam generates fluorescence along his path through the specimen and thus produces photobleaching¹ and phototoxicity² problems, furthermore the penetration depth is limited by absorption of excitation energy along the beam path and by specimen scattering of both the excitation and emission photons.

1.2.1.2 TWO-PHOTON EXCITATION MICROSCOPY

To provide a 3D optical sectioning without absorption above and below the plane of focus, a relatively old theoretical concept in quantum optics called the Two-photon excitation has been used.

The concept of tow photon microscopy is first described by Maria Goeppert-Mayer in her doctoral dissertation in 1931. The two photon excitation concept relies on the fact that one can induce a fluorescence event in a fluophore using a simultaneous absorption of two photons in a single quantum event, where each photon has the half required energy for a normal single photon excitation. As the energy of a photon is inversely proportional to its wavelength, the wavelength of the two absorbed photons must be about twice that required for one-photon excitation. The two photon excitation is achieved by focusing a single pulsed laser through the microscope optics, the laser flux achieve a high spatial density in the focal point (the photon get more crowded) and the probability of two photons interacting simultaneously with a single fluorophore increases. The laser focal point is the only location along the optical path where there is significant occurrence of two-photon excitation, which reduces the photobleaching and the phototoxicity in the specimen and also the background light participation [4].

The high wavelength used in two-photon microscope reduces the absorption in the specimen which mean higher penetration in thick samples, but as the focal spot is still diffraction-limited, the two-photon microscope would have a slighter less resolution than single photon. Like the confocal microscope, the two-photon microscope is slow while acquiring 3D images but is less destructive to the living cells with higher penetration and more contrast [5].

¹ Photobleaching is the photochemical destruction of a fluorophore

² Phototoxicity is a phenomenon, where illuminating a fluorescent molecule causes the selective death of the cells expressing it.

1.2.1.3 TOTAL INTERNAL REFLECTION FLUORESCENCE MICROSCOPY

The use of conventional fluorescence microscopy to study molecular events that take place in cellular surfaces, such as cell adhesion, binding of cells by hormones or membrane dynamics, produces images overwhelmed by the background fluorescence due to the much larger population of non-bound molecules.

The solution was developed by Daniel Axelrod in the early 1980s and it was called the total internal reflection fluorescence microscopy (TIRF). A TIRF microscope uses evanescent wave to selectively illuminate and excite fluorophores in a restricted region of the specimen immediately adjacent to the glass-water interface. The evanescent wave is generated only when the incident light is totally reflected at the glass-water interface. The evanescent electromagnetic field decays exponentially from the interface, and thus penetrates to a depth of only approximately 100 nm into the sample medium (Fig. 9).

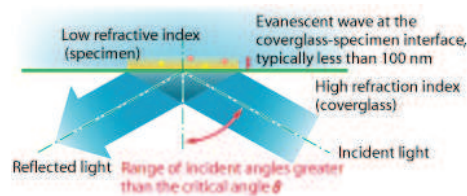


FIG. 9: SELECTIVELY EXCITE FLUOPHORES USING THE EVANESCENT LIGHT. (FROM NIKON)

Note, however, that the region visualized is at least a few hundred nanometers [6]. TIRF can also be used to observe the fluorescence of a single molecule, making it an important tool of biophysics and quantitative biology.

1.2.1.4 4PI MICROSCOPY:

The 4Pi Microscope is a laser scanning fluorescence microscope with an improved axial resolution up to 100-150 nm, it was designed by Stefan Hell in 1992[7] and demonstrated experimentally in 1994[8].

The focal spot size decreases with the microscope's aperture angle in other words, with the size of the spherical wavefront that is produced by the objective lens. The regular objective lens, even of the largest aperture, produces just a segment of a spherical wavefront producing a spot having a longer size in the optical axis than the diameter in the lateral axis. By contrast, if one can produce a full spherical wavefront of a solid angle of 4π , it would lead to an improvement of spatial resolution in the z-direction.

The 4pi microscope uses two opposing objectives lenses which both are focused to the same geometrical location. Also the difference in optical paths lengths through each of the two objective lenses is carefully aligned to be minimal. By doing this, the solid angle

that is used for illumination and detection is increased and approaches the ideal case of 4π [9].

The 4pi microscope have three operating modes depending on the mode of illumination and detection used, in the type A the coherent superposition of the excitation light is used to increase the resolution, the emitted light is either detected from one side or incoherently from both sides. In the type B only the emitted light is interfering when in the type C both excitation and emitted light are allowed to interfere leading to the highest possible resolution increase.

Practically, the highest angular aperture is about 140° for an objective lens, which corresponds to about 1.3π , thereby light is not collected from all sides, leading to so-called side lobes in the point spread function. One can reduce these side lobes effects using image [10] and, more effectively, using two-photon excitation [11]. Acquiring an image using the 4pi microscope needs many difficult preparations and fine tuning of the system making it difficult to be used by non-specialists. This technique is currently commercialized (Leica TCS 4Pi) but poorly used.

1.2.2. HIGH RESOLUTION SOLUTIONS

The techniques exposed up till now enhance the contrast of the acquired images and the resolution, mainly in the lateral axis but they are still diffraction-limited. To be able to detect closely separated identical probes, one need to selectively activate and photobleach fluorophores.

1.2.1.5 STIMULATED EMISSION DEPLETION MICROSCOPY

The Stimulated Emission Depletion microscopy (STED) uses the stimulated emission to bypass the diffraction limit. If an excited dye molecule is irradiated with light of similar wavelength compared to the fluorescence light, it can immediately return to the ground state and emits a photon of exactly the same wavelength and momentum of the light used. Fluorescent dyes can therefore be switched off by additional irradiation of a red-shifted de-excitation beam, and the light originating from the spontaneous decay and from the stimulated emission can be separated from the fluorescent light by using color filters.

This idea was published in 1994 by Stefan Hell [12] and a first experimental realization was demonstrated in 1999 [13].

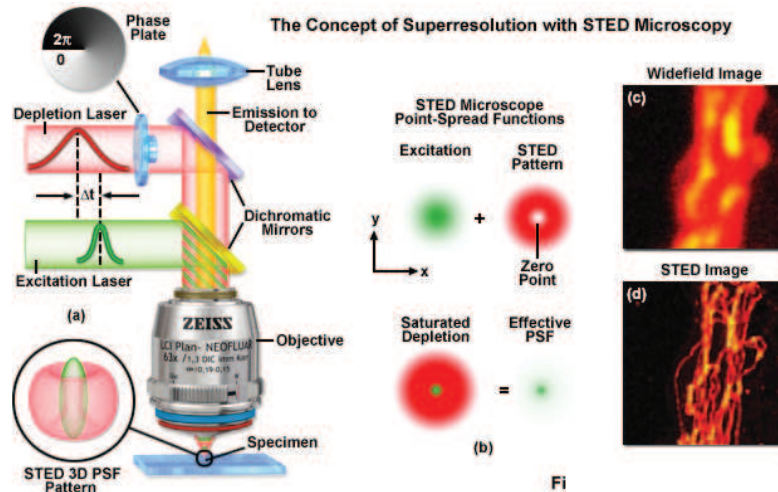


FIG. 10: STED (STIMULATED EMISSION DEPLETION) PRINCIPLE. A DEPLETION LASER SWITCH OFF THE EXCITATION STIMULATION RESULTING IN A REDUCED PSF SIZE. (FROM ZEISS RESSOURCE CENTER)

In a STED microscope (Fig. 10) the sample is first excited by a focused spot similar to the confocal one, the molecules in this spot get to an excited state, a second red-shifted de-excitation laser beam with a ring-like intensity profile is focused. While the dark spot inside the ring is itself diffraction-limited, it features at least some intensity near the focus falling to zero only at the very center. Therefore, using intense depletion light causes almost all of the excited molecules to return to the ground state, leaving only the region of the sample very close to the center of the excitation spot excited. Fluorescence from the remaining excited dye molecules is then detected by the microscope [14].

The size of the spot where molecules are still allowed to fluoresce gets smaller with increasing intensity of the de-excitation light. In order to achieve high resolution (around 5.8nm) one should use femtosecond and nanosecond lasers.

1.2.1.6 PALM AND STORM

Another technique is used by the photo-activated localization microscopy (PALM) [15] and stochastic optical reconstruction microscopy (STORM) [16] where the molecules are labeled with fluorescent probes, and then a burst of light is used to activate the fluorescence in a small percentage of labeled molecules. The microscope captures an image of the fluorescing probes. The technique is designed to activate a sufficiently low percentage of the probes to allow the image of each fluorescing molecule to be seen separately. The exact position of the molecule in x , and y plane is estimated by the center of mass of the PSF captured in a nanometer accuracy (Fig. 11).

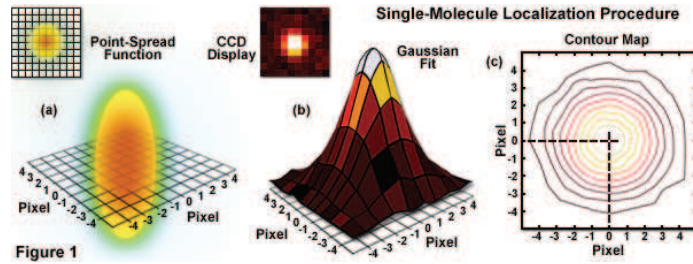


FIG. 11: PALM SINGLE-MOLECULE LOCALIZATION PROCEDURE.

In the Z axis, the position is calculated according to the shape of the PSF (Fig. 12), as at a specific depth, a fluorescing molecule will appear round through the microscope, a cylindrical lens has been introduced into the imaging path of the microscope, so that above and below that point, the circle distorts (becoming more and more elliptical in shape as the distance increases) [17].

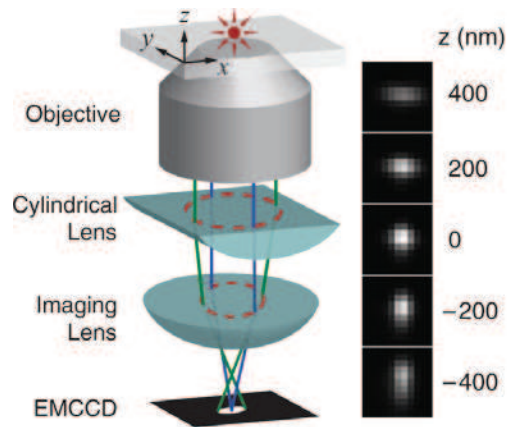


FIG. 12: PALM SINGLE-MOLECULE LOCALIZATION ALONG THE OPTICAL AXIS (DEPTH DISCRIMINATION).

The process is repeated several times, capturing a different subset of molecules each image. A final compilation of the images shows each molecule in its precise location in the cell with nanometer accuracy (20 – 60nm).

A complete image is actually the compilation of millions of points, representing the positions of the molecules of interest, each of which must be precisely localized in three dimensions which can take a long time, too long to catch most of the cell's dynamic processes in action.

1.2.1.7 SIM - STRUCTURED ILLUMINATION MICROSCOPY

The confocal microscopy offers a high capability of optical sectioning where only the plane in focus is efficiently imaged and the out of focus light is rejected by the use of a pinhole. The structured illumination microscopy (SIM) is an alternative method proposed to ameliorate the sectioning capability for the wide field microscopy, this technique has been introduced to the scientific community around 1997[18], it has been also shown that it can be used to enhance resolution in all dimensions by Gustafsson et al in 1999[19].

The structured illumination microscopy uses a single frequency optical grid pattern illumination onto the sample (Fig. 13) and acquires images with the grid in multiple complementary positions and increase the resolution by measuring the fringes in the Moiré pattern (from the interference of the illumination pattern and the sample) and then the image can be deduced from the fringes computationally [18][20].

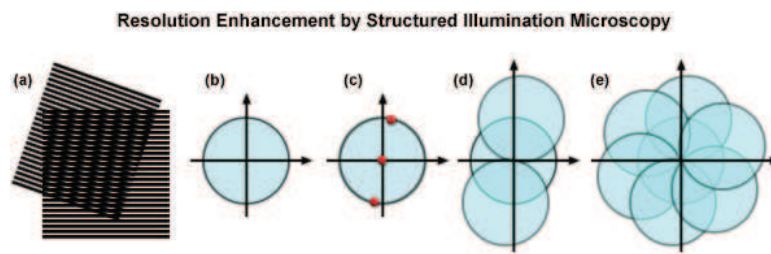


FIG. 13 : STRUCTURED ILLUMINATION MICROSCOPY PRINCIPLE.

The Fourier transform of a SIM's image contains superimposed additional information from different areas of reciprocal space, it is possible to computationally separate and reconstruct a Fourier transform image containing more information from various frames with illumination shifted by some phase, the higher-resolution image is then obtain by the reverse Fourier Transform of the reconstructed solution. As the illumination pattern cannot be focused any smaller than the excitation wavelength, the enhancement in the resolution is only by a factor of two. In order to increase it, nonlinearity can be used [21]. Nonlinearity yields a series of higher-order harmonics in the Fourier transform; each allows another set of images that can be used to reconstruct a larger area in reciprocal space, and thus obtain a higher resolution.

Recently a non-moving parts method is proposed to produce structured illumination patterns based on a micro-structured stripe-array light emitting diode allowing to switch between illumination techniques without modification of the setup [22].

1.2.3. DISCUSSION ON HARDWARE ENHANCEMENT TECHNIQUES

The fluorescence microscope can be decomposed into two functional blocks, the illumination block and the detection block. From this angle of view, the amelioration techniques can be classified according to the concerned block, this classification may yield:

- *Illumination block amelioration techniques:* the main objective of these techniques is to limit the number of actually excited fluorophores to a restraint zone. This zone tends, ultimately, to a single fluorophore or a restricted thickness by using single or combined modification in light coherence, complex optical set to achieve certain focal forms and angles, illumination light wavelength and concentration etc.
- *Detection block amelioration techniques:* these techniques aim to maximize the collect of useful signal by maximizing the angle of collection and thereby the size of the wavefront and/or rejecting the out of focus light using pinhole.

One should keep in mind the importance of the sample in dictating the type of possible amelioration that can be used depending on the fluorophores used (Endogenous or Exogenous), its viability, the temporal stability and the possible field of observation.

1.3 DECONVOLUTION TECHNIQUES

For all the fluorescence microscopes described above (except the PALM and STORM microscope) the acquired image is a result of a convolution process, thereby a software restoration is, in most cases, possible. Furthermore all of these microscopes have their own limitations and in some cases the technique cannot be applied on a certain specimen and the user is bound to the use of the classical form of fluorescence microscopy. In such cases the image restoration by software solutions is the last resort before extraction of available information.

Deconvolution is a computational method used to reduce out-of-focus fluorescence in three-dimensional (3D) microscope images, it tries to reverse the image formation process (convolution) and reconstruct an estimation of the object.

It can be applied to any type of microscope image and it can be accomplished at very low light levels, thus enabling multiple focal-planes imaging of light-sensitive living specimens over long time periods.

The restoration algorithm uses prior information on the optical system used, in order to reverse the blurring function and redistribute the intensities to their points of origin in the specimen. Generally the information needed to perform the inversion is the Point Spread Function of the system or PSF.

By assuming that the PSF is shift invariant into the object space, the image formation is reduced to a simple convolution process:

$$g(x, y, z) = h(x, y, z) \otimes f(x, y, z) \quad (1.2)$$

The deconvolution methods aim to find an estimate $\hat{f}(x, y, z)$ that minimize a resemblance criterion, classically the quadratic error $\|f(x, y, z) - \hat{f}(x, y, z)\|^2$ adding eventually a penalization criterion or constraints based on some prior knowledge of the restored object yielding more or less complex formula.

The noise statistics can also be considered, some assume a Gaussian distribution that can be modeled as additive noise. Others use a Poisson statistics, more realistic approach in the case of photons-limited imaging.

If the minimization of the resemblance criterion can be done analytically, this will leads to direct inversion methods, those methods are usually fast but sensible to noise, and otherwise the minimization will be done iteratively yielding a lengthy process but usually a better immunity to noise.

1.3.1 DIRECT INVERSION METHODS

1.3.1.1 INVERSION

When discretizing, the formula (1.2) can be represented in a matrix form as [23]:

$$\mathbf{g} = \mathbf{H}\mathbf{f} + \mathbf{n} \quad (1.3)$$

Where “ \mathbf{H} ” is a linear transformation formed by the PSF values, under the space non invariance assumption, it is a Toeplitz matrix with banded Toeplitz blocks. Some solutions try to solve the equation $\hat{\mathbf{f}} = \mathbf{H}^{-1}\mathbf{g}$ with singular value decomposition (*SVD*)³ but “ \mathbf{H} ” is ill-conditioned with singular values decaying to, clustering at zero and containing noise. Thus, standard techniques produce solutions highly corrupted with noise with local instabilities.

Another direct approach uses the fact that a convolution becomes a multiplication in Fourier space, thus the equation (1.2) can be written in Fourier space as:

$$G(u, v, w) = F(u, v, w)H(u, v, w) + N(u, v, w) \quad (1.4)$$

Where the upper case notation denotes a Fourier transform. By neglecting the noise one can writes $\hat{F}(u, v, w) = \frac{G(u, v, w)}{H(u, v, w)}$ and the estimate $\hat{f}(x, y, z)$ is the inverse Fourier transform of the resulting [24]. Using such direct inversion leads to instabilities, especially that the OTF, H drops off at higher frequencies and goes to zero at $f_c = 2NA/\lambda$, the optical cutoff frequency. Frequencies above the cutoff are not recorded in the microscope image.

A simple solution to help overcome this problem (especially preventing the zero division) is to limit the OTF as follow:

$$\hat{F}(u, v, w) = \begin{cases} \frac{G(u, v, w)}{H(u, v, w)} & |H(u, v, w)| \geq \varepsilon \\ 0 & |H(u, v, w)| < \varepsilon \end{cases}$$

Where ε is a positive constant, which defines a balance between resolution and noise.

1.3.1.2 WIENER DECONVOLUTION

The wiener approach tries to filter the data while restoring the original image; it implements a balance between inverse filtering and noise smoothing that is optimal in mean square error sense.

Assuming the noise as a white Gaussian distribution, it calculates:

$$H^{-1}(u, v, w) = H_{wiener} = \frac{H^*(u, v, w)}{|H(u, v, w)|^2 + \left(\frac{S_n(u, v, w)}{S_f(u, v, w)} \right)} \quad (1.5)$$

Where S_f, S_n are the power spectral density of the image and the noise respectively and * denotes the complex conjugate.

The equation (1.5) can be rewritten as:

$$H^{-1}(u, v, w) = \frac{1}{H(u, v, w)} \left[\frac{|H(u, v, w)|^2}{|H(u, v, w)|^2 + \frac{1}{SNR(u, v, w)}} \right] \quad (1.6)$$

Where $SNR(u, v, w) = \frac{S_f(u, v, w)}{S_n(u, v, w)}$ represents the signal to noise ratio. As it can be seen in equation (1.6) the process can be interpreted as two filters in cascading the frequency domain, where $\frac{1}{H(u, v, w)}$ the inverse filter and the term between brackets is the Wiener filter. In a noise free case the term between brackets is reduced to one and the formula become a normal inverse filter case, otherwise The Wiener filter attenuates certain frequencies according to their SNR.

Wiener deconvolution performs well in the presence of noise, but it tends to smooth the image which is not appreciated in the case of fine details. Finally, Wiener deconvolution cannot handle a spatially variant microscope PSF.

1.3.1.3 LINEAR LEAST SQUARE

The Linear Least Square method (LLS) also assumes a white Gaussian noise distribution; it uses the discrete formulation (formula 1.2).

The formulation as a least-squares minimization problem is presented as following using the vectorial notation; one try to find an estimate $\hat{\mathbf{f}}$, so if it is blurred by \mathbf{H} , the result will differs from \mathbf{g} by as little as possible in the mean square sense. Since \mathbf{g} itself is simply \mathbf{f} blurred by \mathbf{H} , if \mathbf{f} and $\hat{\mathbf{f}}$ are nearly equal, then hopefully $\hat{\mathbf{f}}$ is a good estimation. This formulation is different from that used in the Wiener filter. It is the difference between the blurred original and a similarly blurred estimate of the original that is minimized.

The minimization formula is written as:

$$\|\mathbf{e}(\hat{\mathbf{f}})\|^2 = \|\mathbf{g} - \mathbf{H}\hat{\mathbf{f}}\|^2 = (\mathbf{g} - \mathbf{H}\hat{\mathbf{f}})^T (\mathbf{g} - \mathbf{H}\hat{\mathbf{f}}) \quad (1.7)$$

Where $\|\mathbf{a}\| = \sqrt{\mathbf{a}^T \mathbf{a}}$ denotes the Euclidean norm of a vector. The solution is then written as:

$$\hat{\mathbf{f}} = [\mathbf{H}^T \mathbf{H}]^{-1} \mathbf{H}^T \mathbf{g} \quad (1.8)$$

The variance and the error depend on the eigenvalues, which are used for the matrix-inversion operation. The algorithm searches the optimal number of eigenvalues to be used in the inversion process by discarding the lowest eigenvalues. The formula (1.8) can be written in the frequency domain as [25]:

$$\hat{F} = \frac{\mu_h^* G}{|\mu_h|^2} \quad (1.9)$$

The regularization is done by using k largest eigenvalues μ_h from the normalized PSF according to a threshold λ .

Using the Regularized Linear Least Square (RLLS) algorithm the estimate of the 3-D image is obtained in a single pass, but it still highly sensitive to noise and limited to an invariant PSF. During the thesis the RLLS method was implemented as an ImageJ plugIn as described in [26].

1.3.1.4 TIKHONOV-MILLER FILTER

Andrei Nikolaevich Tikhonov proposed an error criterion [26] that consists of minimizing the term:

$$\left\|g(x, y, z) - h(x, y, z) \otimes \hat{f}(x, y, z)\right\|^2 + \lambda \left\|R \otimes \hat{f}(x, y, z)\right\|^2 \quad (1.10)$$

Where R corresponds to a high pass filter. This criterion contains two terms; the first one, expresses fidelity to the data $g(x, y, z)$ and the second one smoothness of the restored image, λ is the regularization parameter and represents the trade-off between fidelity to the data and the restored image smoothness. Finding the optimal value necessitates use of numeric techniques such as Cross-Validation. The analytical direct solution of this criterion yields Tikhonov-Miller filter which is a generalization of Wiener filter

$$H^{-1} = H_{im} = \frac{H^*}{H^*H + \lambda R^*R} \quad (1.11)$$

1.3.2 ITERATIVE METHODS

The direct methods are fast to compute, but they have several drawbacks. These include the inability to incorporate prior knowledge about the true image, the fact that negative intensities might occur in the deconvolved image, and ringing artifacts that may be created near edges. Artifacts result from an inability to estimate the high-frequency components that are cut off by the diffraction-limited objective. The solution is to use an iterative approach that incorporate some prior knowledge about the data like non-negativity and enforce regularization constraints that the specimen estimate must satisfy.

1.3.2.1 JANSSON – VAN CITTERT

Jansson-Van Cittert method (JVC) is an iterative method in the spatial domain, it proposes the following iteration [27]:

$$\hat{f}_{n+1}(x, y, z) = \hat{f}_n(x, y, z) + \alpha \left(g(x, y, z) - \hat{f}_n(x, y, z) \otimes h(x, y, z) \right) \quad (1.12)$$

Where α is a converging parameter, it controls, during the iteration, voxel-specific constraints and image convergence constraints. The method proceeds by repeatedly adding term proportional to the residual scaled by α . Typically, α is a finite weight function that is defined over a positive intensity range. It is used to prevent unusually bright intensities in the estimated image and negative intensities.

A critical factor in reconstruction quality is the mitigation of noise, as equation(1.12) is not regularized, as iterations proceed, noise is amplified. Most implementations suppress this with a smoothing filter (e.g., Gaussian), which simultaneously attenuates both signal and noise. Residual structures are then amplified by a high-pass filter. The equation (1.12) becomes [28]:

$$\widehat{f}_{n+1}(x, y, z) = \widehat{f}_n(x, y, z) + \alpha h_s(x, y, z) \otimes [g(x, y, z) - h(x, y, z) \otimes \widehat{f}_n(x, y, z)] \quad (1.13)$$

Where $h_s(x, y, z) = h(-x, -y, -z)$.

Most often, the smoothing operation does not work well for low-SNR images it amplifies the noise while converging as its effect is masked by the convolution in the error criterion.

1.3.2.2 ITERATIVE CONSTRAINED TIKHONOV–MILLER ALGORITHM

The iterative constrained Tikhonov-Miller algorithm [29] resolves the Tikhonov-Miller criterion iteratively and introduces a non-negativity constraint by clipping to zero the negative intensities at each iteration step. This algorithm finds the minimum of Tikhonov-Miller functional using the method of conjugate gradients. The conjugate gradient direction d of the formula (1.10) is given by:

$$d_n = r_n + \gamma_n d_{n-1}, \quad \gamma_n = \frac{\|r_n\|^2}{\|r_{n-1}\|^2} \quad (1.14)$$

Where n denotes the iteration number and r is the steepest descent direction given by:

$$r_n = -\frac{1}{2} \tilde{N}_f \Phi(\widehat{\mathbf{f}}) = (\mathbf{H}^T \mathbf{H} + \lambda \mathbf{R}^T \mathbf{R}) \widehat{\mathbf{f}}_n - \mathbf{H}^T \mathbf{g} \quad (1.15)$$

The new conjugate gradient estimate is now found with:

$$\mathbf{f}_{n+1} = P(\mathbf{f}_n + \beta_n \mathbf{d}_n) \quad (1.16)$$

Where P is a projection function to incorporate the constraints, in this case:

$$P(f_i) = \begin{cases} f_i & \text{if } f_i \geq 0 \\ 0 & \text{otherwise} \end{cases}$$

β_n is the optimal step size, which can be analytically determined using an iterative one-dimensional minimization algorithm, such as the golden section rule or by using a first-order Taylor series expansion of (1.16) with respect to β which will yields:

order Taylor series expansion of **Error! Reference source not found.** with respect to β which will yields:

$$\beta = \frac{\mathbf{d}^T T(\mathbf{f}) r}{\mathbf{d}^T T(\mathbf{f}) (\mathbf{H}^T \mathbf{H} + \lambda \mathbf{R}^T \mathbf{R}) T(\mathbf{f}) \mathbf{d}}$$

with the diagonal threshold matrix T defined as:

$$T(f)_{ij} = \begin{cases} 1 & f_i \geq 0 \text{ and } i = j \\ 0 & \text{otherwise} \end{cases}$$

Although the ICTM algorithm used with a non-negativity constraint is less artifactual than non-iterative TM restoration, it is more computationally expensive.

1.3.2.3 CARRINGTON ALGORITHM

Carrington proposed a regularization method based on minimization with constraints in the least squares sense [30]. One has to minimize the following function:

$$\min_{\{\hat{f} \geq 0\}} \sum \left| g(x, y, z) - \iiint h(x, y, z) \hat{f}(x, y, z) dx dy dz \right|^2 + \alpha \iiint \left| \hat{f}(x, y, z) \right|^2 dx dy dz \quad (1.17)$$

Where α is a constant. The first term in the equation (1.17) represents the difference between the original and the restored images. The second term represents a smoothing of the data weighted by α to prevent noise in $g(x, y, z)$ from introducing unwanted oscillations. If the value of α is small, the restored data become more noise sensitive but have more accuracy, otherwise if the value of α is large, the restored data are smoothed and weakly noise sensitive, the accuracy is, however, relatively low.

Carrington uses the method of projection onto convex sets (POCS) [31] to integrate the constraints in a rigorous way, which will make the result to converge into a unique solution.

1.3.2.4 MAXIMUM-LIKELIHOOD EXPECTATION-MINIMIZATION ALGORITHM (ML-EM)

The likelihood of a recorded image \mathbf{g} , knowing the microscope PSF “ h ”, is a function of the true specimen image \mathbf{f} , and it is noted by $P(\mathbf{g} | \mathbf{f}, h)$. Then the problem of image restoration is to estimate the unknown parameters $f(X), \forall X \in S_f$ where S_f is the support of \mathbf{f} . The expectation maximization is an iterative algorithm that tries to find the maximum likelihood estimate while some data is missing or hidden. The aim is to estimate the model parameters (specimen function, $\hat{\mathbf{f}}$) for which the observed data are the most likely.

The ML-EM algorithm can be applied in both Gaussian and Poisson statistic distribution cases.

In the Gaussian noise case the probability density function is given by:

$$P(\mathbf{g} | \mathbf{f}, \mathbf{H}) = \frac{1}{(2\pi)^{N/2\sigma^2}} \exp\left(\frac{-\|\mathbf{g} - \mathbf{H}\mathbf{f}\|^2}{2\sigma^2}\right) \quad (1.18)$$

Where N is the number of voxels and σ^2 is the noise variance. The ML solution for the image estimate $\hat{\mathbf{f}}$, which is most likely to give rise to the observed image \mathbf{g} , is found by solving:

$$\hat{\mathbf{f}} = \arg \min_f \frac{\|\mathbf{g} - \mathbf{H}\mathbf{f}\|^2}{2\sigma^2} \quad (1.19)$$

This is similar to the least-square solution and can be solved using the following iteration:

$$\hat{\mathbf{f}}_{n+1} = \hat{\mathbf{f}}_n + \eta \mathbf{H}^T (\mathbf{g} - \mathbf{H}\hat{\mathbf{f}}_n) \quad (1.20)$$

Where η is a predetermined parameter such that $0 < \eta < 2/\sigma_1^2$, where σ_1^2 is the largest singular value of the matrix \mathbf{H} .

In a Poisson noise case, if A represents the mean number of photon counted at all image voxels, the probability of counting exactly n photons during the exposure time of one voxel have the density of:

$$P(n) = \frac{A^n}{n!} \exp(-A) \quad (1.21)$$

Then the probability density function of the image is written as:

$$P(\mathbf{g} | \mathbf{f}, \mathbf{h}) = \frac{(\mathbf{h}\mathbf{f})^{\mathbf{g}}}{\mathbf{g}!} \exp(-\mathbf{h}\mathbf{f}) \quad (1.22)$$

The maximum likelihood solution can be found by setting $\partial \log(P(\mathbf{g} | f, h)) / \partial f$ to zero, and the iterative solution may be written as:

$$\begin{aligned} \hat{\mathbf{f}}_{n+1} &= \hat{\mathbf{f}}_n \frac{1}{h(0)} \left[\begin{array}{c} \mathbf{H} \mathbf{g} \\ \mathbf{H}\hat{\mathbf{f}} \end{array} \right] \\ \hat{f}_{n+1}(x, y, z) &= \hat{f}_n(x, y, z) \frac{1}{h(0)} h(x, y, z) \otimes \left(\frac{g(x, y, z)}{h(x, y, z) \otimes \hat{f}_n(x, y, z)} \right) \end{aligned} \quad (1.23)$$

Where $h(0)$ is the mean value of the PSF [32] [33].

Regularization can be applied as a penalty function added to the likelihood function; this is known as the maximum-penalized-likelihood (MPL) method [34], where the likelihood function is modified such that it decreases when the noise increases.

The EM algorithm has a slow convergence rate and is quite computationally intensive.

1.3.2.5 LUCY-RICHARDSON METHOD

Lucy-Richardson [35] [36] is an iterative method similar to the ML-EM for Poisson noise [37], the maximization of $P(\mathbf{g} | f, h)$ in respect to f leads to this iterative formulation:

$$\hat{f}_{n+1}(x, y, z) = \left[\frac{g(x, y, z)}{\hat{f}_n(x, y, z) \otimes h(x, y, z)} \otimes h(-x, -y, -z) \right] \hat{f}_n(x, y, z) \quad (1.24)$$

In matrix form it is written as:

$$\hat{\mathbf{f}}_{n+1} = \left[\begin{array}{c} \mathbf{H}^T \mathbf{g} \\ \mathbf{H}\hat{\mathbf{f}}_n \end{array} \right] \hat{\mathbf{f}}_n \quad (1.25)$$

Where \mathbf{H}^T denotes the transpose of the convolution matrix corresponding to the PSF. As long as the initial estimate is positive the iterations remain positive. The algorithm is stopped when the MSE (between the estimated image and the true solution) reaches a minimum; actually it increases again when noise over-fitting begins.

The Lucy-Richardson algorithm is constrained but not regularized. Conchello has derived an algorithm that incorporates Tikhonov regularization into the Richardson-Lucy algorithm [29] and the regularized solution can be calculated from the un-regularized one using this formula:

$$\hat{f}_{n+1}^{\text{regularized}} = \frac{-1 + \sqrt{1 + 2\lambda \hat{f}_{n+1}}}{\lambda} \quad (1.26)$$

Where \hat{f}_{n+1} is calculated in (1.24).

1.3.2.6 MAXIMUM A POSTERIORI METHOD (MAP)

Alternative Bayesian statistic can be used for regularization in the form of a prior probability distribution. Let $P(g|f)$ be the probability of observing the image g from a fluore distribution f , if the probability distribution function $P(f)$ represents prior knowledge about the true image then according to Bayes' theorem, the posterior probability of having f knowing g can be calculated as:

$$P(f|g) = \frac{P(g|f)P(f)}{P(g)} \quad (1.27)$$

As $P(g)$ depends entirely on the observed image, it can be regarded as normalization constant, thus the MAP solution is obtained by maximizing the posteriori probability:

$$\hat{f} = \arg \max_f P(g|f)P(f) \quad (1.28)$$

$P(f)$ is used to introduce prior information about the true object, thereby the selection of a prior distribution that performs well for one class of images might not be suitable for another. Several forms of the prior distribution have been published, including the Gibbs distribution [38] and the Good's roughness penalty [39] [40]. Alternatively, when information about the true image is not available, the probability can be based on the entropy of "f" [41]. Preza has published a MAP solution with Gaussian statistics and found an analytical solution called LMAP [42].

1.3.2.7 MONTECARLO RESTORATION

Bruno Colicchio [43] has presented in his thesis a method of image reconstruction that may take into account possible spatial variations of the PSF. This method is based on the interpretation of image formation described by Fig.4, where the accumulations of point-like sources build up the image. The technique PALM or STORM controls this phenomenon by stimulation of single molecules and localizing them through time. In the case of deconvolution, the collection of points (object) is to be found in a collection of PSF (the observed image) Deconvolution is achieved by exploring probable configurations of point-like source in the object space, where their projections onto the image space could minimize an error criterion with the acquired one.

The exploration of space object and image is achieved by a random displacement of each space's basic element (grain). The acceptance of the elementary grain placement is then based on the improvement of an error criterion in image space (quadratic error). Furthermore a constraint in the object space is applied to the variance of intensities as a regularization criterion. The minimization is performed by simulated annealing. This method is very heavy on computational time, but extremely simple to implement on embedded computing systems. An application of this method is currently a potential solution in the field of infrared imaging in partnership with a company of civil and military security.

1.3.3 BLIND DECONVOLUTION

In order to obtain a good estimation of the object, all the techniques described above need a known and relatively accurate PSF describing the imaging system. However this condition cannot always be fulfilled, obtaining an accurate PSF is not an easy task, as measured ones is always polluted with noise and the calculated ones do not always include all the aberrations that the imaging system may have. The blind deconvolution process tries to estimates not only the unknown image but also the PSF of the system, both from the acquired image with a little or without prior information about the later.

Considering the problem of deconvolution is ill-posed, Blind Deconvolution is a challenging task, because the unknowns are increased without increasing the amount of data.

If one consider the blurring observation model in the Fourier Space without noise $G(u, v, w) = F(u, v, w) \cdot H(u, v, w)$ and try to find both H and the object F from this product. Several solutions can respond to this problem. Another ambiguity is in the scaling factor. If (H, F) is a solution then $\left(\alpha \cdot H, \frac{1}{\alpha} \cdot F \right) \forall \alpha > 0$ are solutions too.

Then the blind deconvolution algorithms impose a forced normalization on H in addition to some constraints on H and F in order to reduce the space of possible solutions and to regularize the problem.

Several authors have described blind deconvolution algorithms , some approaches constrain the PSF to be circularly symmetric and band-limited; others apply a quadratic parameterization to enforce non-negativity on f and use a PSF parameterization based on a mathematical model [44].

In optical microscopy, Holmes [45] was the first to propose a maximum likelihood-estimation-based blind deconvolution algorithm to deblur simulated images. An iterative blind deconvolution algorithm operates as follow:

In general, an iterative estimate of the object is computed, in the first iteration step, the object estimate is simply the recorded image, which is convolved with a theoretical PSF calculated from the optical parameters of the imaging system. The resulting blurred specimen estimate is compared with the raw image, and a correction is computed. This correction is used to generate the next estimate. The same correction is also applied to the PSF, generating a new PSF estimate and so on. Constraints can be imposed at each iteration step.

1.4 CONCLUSION

The hardware ameliorations are highly encouraged to be used when the specimen permit it. However when this is not possible, numerical restoration can be used in order to ameliorate the images and reduce the quantitative measurement's errors.

As seen, one can use a large set of deconvolution algorithms to restore fluorescence microscopy images. As each family of these algorithms uses a different method to approach the inverse problem, one cannot expect to obtain the same qualitative results with all of them.

The selection of the correct algorithm to use was a large subject for [46] [47].

The linear direct inversion methods are very sensitive to noise but they are fast, which is an important variable when processing large 3D data. One can use these algorithms with high signal to noise ratio data and can enhance furthermore the result by applying a filtering process before the deconvolution itself [48].

The iterative algorithms yield a relatively good result when the noise can be considered as Gaussian (high luminosity images), Carrington algorithm is noticed to be highly effective with fine details data like filaments.

The algorithms that incorporate a noise with Poisson statistic approach, find its use when the data present low luminosity and the noise statistics can be no longer considered as Gaussian, these algorithms are slow and may need up to few hundred iterations for good results especially in the case of EM based algorithms. Lucy-Richardson algorithm is faster to converge with good results, that what make it widely used.

One will notice that the value of the regularization constant is totally left to the user's attention, finding the correct value depend largely on the user's experience and the value is specific to each family of images. In order to find the optimum value, some algorithms have been developed [49] and it can be used at least once to obtain some idea of the proper value for a certain images type [42].

Finally the PSF is considered as shift invariant into the object space, which allows us the use of matrix notation where the PSF become a Toeplitz matrix formed with sub Toeplitz matrix, and in also the use of fast Fourier transform (FFT) to perform fast convolution process. This assumption cannot be maintained, especially with thick data as the PSF can present large variations with depth. Furthermore the specimen optical proprieties may induce large variation into the PSF.

During this thesis, multiple deconvolution algorithms (LLS, Lucy-Richardson, Jansson-Van Cittert) have been implemented as an ImageJ plugins coupled with JNI (Java Native

Chapter 1

Interface) to optimize computation speed. These implementation are part of IMMSI (Imagerie Microscopique Multidimensionnelle et systèmes d'information), a multi-disciplinary project regrouping the themes of our laboratory that aim to help the users in the choice of the deconvolution algorithm and automate the processing procedure based on the input data attributes.

When the PSF is depth variant the matrix based algorithms become unusable (See chapter 2) and only the iterative algorithms may be adapted by implementing depth variant convolution. Monte-carlo algorithm can be easily applied on depth variant case where each grain in the object space has its corresponding “image” grain in the image space.

In the next chapter we will discuss depth variant PSF case and the possible solutions provided in the literature. We also propose a method that can use any classical deconvolution algorithm to solve the depth variant PSF problem.

1.5 REFERENCES

-
- [1] M. Minsky, "Microscopy apparatus," U.S. Patent No. 3013467, United States (1961).
- [2] N. Claxton, T. Fellers, and M. Davidson, "Laser scanning confocal microscopy," Olympus (2006).
- [3] T. Wilson, *Theory and Practice of Scanning Optical Microscopy*, 1st ed., Academic Press (1984).
- [4] K. W. Dunn and P. A. Young, "Principles of multiphoton microscopy," *Nephron Exp. Nephrol* **103**, e33-40 (2006) [doi:10.1159/000090614].
- [5] D. W. Piston, "Imaging living cells and tissues by two-photon excitation microscopy," *Trends in Cell Biology* **9**, 66-69 (1999) [doi:10.1016/S0962-8924(98)01432-9].
- [6] Y. Sako and T. Uyemura, "Total Internal Reflection Fluorescence Microscopy for Single-molecule Imaging in Living Cells," *Cell Structure and Function* **27**, 357-365 (2002).
- [7] S. D. [+. (S. Hell, "Double-confocal Scanning Microscope.," U.S. Patent No. EP0491289 (A1) (1992).
- [8] S. W. Hell, E. H. K. Stelzer, S. Lindek, and C. Cremer, "Confocal microscopy with an increased detection aperture: type-B 4Pi confocal microscopy," *Opt. Lett.* **19**, 222-224 (1994) [doi:10.1364/OL.19.000222].
- [9] K. Bahlmann, S. Jakobs, and S. W. Hell, "4Pi-confocal microscopy of live cells," *Ultramicroscopy* **87**, 155-164 (2001).
- [10] M. Schrader, S. W. Hell, and H. T. M. van der Voort, "Three-dimensional super-resolution with a 4Pi-confocal microscope using image restoration," *J. Appl. Phys.* **84**, 4033 (1998) [doi:10.1063/1.368616].
- [11] S. W. Hell, S. Lindek, and E. H. K. Stelzer, "Enhancing the Axial Resolution in Far-field Light Microscopy: Two-photon 4Pi Confocal Fluorescence Microscopy," *Journal of Modern Optics* **41**, 675 (1994) [doi:10.1080/09500349414550701].
- [12] S. W. Hell and J. Wichmann, "Breaking the diffraction resolution limit by stimulated emission: stimulated-emission-depletion fluorescence microscopy," *Opt. Lett.* **19**, 780-782 (1994) [doi:10.1364/OL.19.000780].
- [13] T. A. Klar and S. W. Hell, "Subdiffraction resolution in far-field fluorescence microscopy," *Opt. Lett.* **24**, 954-956 (1999) [doi:10.1364/OL.24.000954].
- [14] S. W. Hell and M. Kroug, "Ground-state-depletion fluorescence microscopy: A concept for breaking the diffraction resolution limit," *Appl. Phys. B* **60**, 495-497 (1995) [doi:10.1007/BF01081333].
- [15] H. Shroff, H. White, and E. Betzig, "Photoactivated localization microscopy (PALM) of adhesion complexes," *Curr Protoc Cell Biol* **Chapter 4**, Unit 4.21 (2008) [doi:10.1002/0471143030.cb0421s41].
- [16] M. J. Rust, M. Bates, and X. Zhuang, "Sub-diffraction-limit imaging by stochastic optical reconstruction microscopy (STORM)," *Nat Meth* **3**, 793-796 (2006) [doi:10.1038/nmeth929].
- [17] B. Huang, S. A. Jones, B. Brandenburg, and X. Zhuang, "Whole-cell 3D STORM reveals interactions between cellular structures with nanometer-scale resolution," *Nat Meth* **5**, 1047-1052 (2008) [doi:10.1038/nmeth.1274].
- [18] M. A. A. Neil, R. Juskaitis, and T. Wilson, "Method of obtaining optical sectioning by using structured light in a conventional microscope," *Opt. Lett.* **22**, 1905-1907 (1997) [doi:10.1364/OL.22.001905].

- [19] M. G. L. Gustafsson, "Surpassing the lateral resolution limit by a factor of two using structured illumination microscopy," *Journal of Microscopy* **198**, 82-87 (2000).
- [20] L. H. SCHAEFER, D. SCHUSTER, and J. SCHAFFER, "Structured illumination microscopy: artefact analysis and reduction utilizing a parameter optimization approach," *Journal of Microscopy* **216**, 165-174 (2004).
- [21] M. G. L. Gustafsson, "Nonlinear structured-illumination microscopy: Wide-field fluorescence imaging with theoretically unlimited resolution," *Proceedings of the National Academy of Sciences of the United States of America* **102**, 13081 -13086 (2005) [doi:10.1073/pnas.0406877102].
- [22] B. Chang, L. Chou, Y. Chang, and S. Chiang, "Isotropic image in structured illumination microscopy patterned with a spatial light modulator," *Opt. Express* **17**, 14710-14721 (2009) [doi:10.1364/OE.17.014710].
- [23] B. Hunt, "A matrix theory proof of the discrete convolution theorem," *Audio and Electroacoustics, IEEE* **19**, 285-288 (1971).
- [24] A. Erhardt, G. Zinser, D. Komitowski, and J. Bille, "Reconstructing 3-D light-microscopic images by digital image processing," *Appl. Opt.* **24**, 194-200 (1985) [doi:10.1364/AO.24.000194].
- [25] C. Preza, M. I. Miller, J. Thomas, and J. G. McNally, "Regularized linear method for reconstruction of three-dimensional microscopic objects from optical sections," *J. Opt. Soc. Am. A* **9**, 219-228 (1992) [doi:10.1364/JOSAA.9.000219].
- [26] A. N. Tikhonov, *Solutions of Ill Posed Problems*, Vh Winston (1977).
- [27] P. H. Van Cittert, "Zum Einfluss der Spaltbreite auf die Intensitätsverteilung in Spektrallinien.II," *Z. Phys* **69**, 298-308 (1931).
- [28] D. A. Agard, "Optical Sectioning Microscopy: Cellular Architecture in Three Dimensions," *Annu. Rev. Biophys. Bioeng.* **13**, 191-219 (1984) [doi:10.1146/annurev.bb.13.060184.001203].
- [29] J. Conchello and J. G. McNally, "Fast Regularization Technique for Expectation Maximization Algorithm for Optical Sectioning Microscopy."
- [30] W. Carrington, R. Lynch, E. Moore, G. Isenberg, K. Fogarty, and F. Fay, "Superresolution three-dimensional images of fluorescence in cells with minimal light exposure," *Science* **268**, 1483-1487 (1995) [doi:10.1126/science.7770772].
- [31] R. Abma and N. Kabir, "3D interpolation of irregular data with a POCS algorithm," *SEG Expanded Abstracts* **24**, 2150-2153 (2005) [doi:10.1190/1.2148139].
- [32] T. J. Holmes, "Maximum-likelihood image restoration adapted for noncoherent optical imaging," *J. Opt. Soc. Am. A* **5**, 666-673 (1988) [doi:10.1364/JOSAA.5.000666].
- [33] T. J. Holmes, "Expectation-maximization restoration of band-limited, truncated point-process intensities with application in microscopy," *J. Opt. Soc. Am. A* **6**, 1006-1014 (1989) [doi:10.1364/JOSAA.6.001006].
- [34] H. M. Hudson and T. C. M. Lee, "Maximum likelihood restoration and choice of smoothing parameter in deconvolution of image data subject to Poisson noise," *Comput. Stat. Data Anal.* **26**, 393-410 (1998).
- [35] L. B. Lucy, "An iterative technique for the rectification of observed distributions," *The Astronomical Journal* **79**, 745 (1974) [doi:10.1086/111605].
- [36] W. H. RICHARDSON, "Bayesian-Based Iterative Method of Image Restoration," *J. Opt. Soc. Am.* **62**, 55-59 (1972) [doi:10.1364/JOSA.62.000055].
- [37] T. J. Holmes and Y. Liu, "Richardson-Lucy/maximum likelihood image restoration algorithm for fluorescence microscopy: further testing," *Appl. Opt.* **28**, 4930-4938 (1989) [doi:10.1364/AO.28.004930].
- [38] S. Geman and D. Geman, "Stochastic relaxation, Gibbs distributions and the

- Bayesian restoration of images,” *IEEE Transactions on Pattern Analysis and Machine Intelligence* **6**, 721-741 (1984).
- [39] S. Joshi and M. I. Miller, “Maximum a posteriori estimation with Good's roughness for three-dimensional optical-sectioning microscopy,” *J Opt Soc Am A* **10**, 1078-1085 (1993).
- [40] P. J. Verveer and T. M. Jovin, “Image restoration based on Good's roughness penalty with application to fluorescence microscopy,” *J. Opt. Soc. Am. A* **15**, 1077-1083 (1998) [doi:10.1364/JOSAA.15.001077].
- [41] R. Kikuchi and B. H. Soffer, “Maximum entropy image restoration. I. The entropy expression,” *J. Opt. Soc. Am.* **67**, 1656-1665 (1977) [doi:10.1364/JOSA.67.001656].
- [42] C. Preza, M. I. Miller, and J. Conchello, “Image Reconstruction For 3-D Light Microscopy With A Regularized Linear Method Incorporating A Smoothness Prior,” *ACHARYA, R.S. & GOLDFOF, D.B. (EDS), IS&T/SPIE PROCEEDINGS*, 129--139 (1992).
- [43] B. Colicchio and S. Jacquey, “Déconvolution adaptative en microscopie tridimensionnelle de fluorescence,” Haute-Alsace University (2004).
- [44] P. PANKAJAKSHAN, “Blind Deconvolution for Confocal Laser Scanning Microscopy” (2009).
- [45] T. J. Holmes, “Blind deconvolution of quantum-limited incoherent imagery: maximum-likelihood approach,” *J. Opt. Soc. Am. A* **9**, 1052-1061 (1992) [doi:10.1364/JOSAA.9.001052].
- [46] J. G. McNally, T. Karpova, J. Cooper, and J. A. Conchello, “Three-Dimensional Imaging by Deconvolution Microscopy,” *Methods* **19**, 373-385 (1999) [doi:10.1006/meth.1999.0873].
- [47] A. Chomik, A. Dieterlen, C. Xu, O. Haeberle, J. J. Meyer, and S. Jacquey, “Quantification in optical sectioning microscopy: a comparison of some deconvolution algorithms in view of 3D image segmentation,” *Journal of Optics* **28**, 225-233 (1997).
- [48] H. olivier and C. bruno, “Techniques d’amélioration de la résolution en microscopie de fluorescence : de la production des photons au traitement des images,” 25 May 2009, <http://spectrabiology.com/Documents/SA244_22-26.pdf> (25 May 2009).
- [49] B. Colicchio, O. Haeberlé, C. Xu, A. Dieterlen, and G. Jung, “Improvement of the LLS and MAP deconvolution algorithms by automatic determination of optimal regularization parameters and pre-filtering of original data,” *Optics Communications* **244**, 37-49 (2005) [doi:10.1016/j.optcom.2004.08.039].

2. SPACE VARIANT PSF DECONVOLUTION

ANY INTELLIGENT FOOL CAN MAKE THINGS BIGGER AND MORE COMPLEX... IT TAKES A TOUCH OF GENIUS - AND A LOT OF COURAGE TO MOVE IN THE OPPOSITE DIRECTION.
ALBERT EINSTEIN

2.1. INTRODUCTION

In this chapter we present a method to adapt all non-blind deconvolution algorithm presented in the previous chapter to be a solution for non-invariance problem, without any modification of the later.

It is important to obtain an accurate PSF of the used microscope in order to achieve good restoration of the acquired images [1]; furthermore studying the PSF may deliver information on some optical aberrations in the system.

Three methods may be used in order to obtain a system's PSF: experimental, mathematical or analytical.

The analytical method consists on estimating the system's PSF using the blind deconvolution process. This method uses a parametrical model for the PSF and tries to find iteratively the parameters that best suit the system. It can be more or less adapted to a system depending on the complexity of the PSF. [2]

The mathematical approach uses a fixed formulation for the PSF developed using a physical model of light propagation [3]. It can be more or less complex and accurate, but this method might not take into consideration all the aberrations that exist in the optical path and are not included into the mathematical model. In our work we will use the vectorial model made by Török and Varga [4] and modified by Olivier heaberlé [5] to simulate PSF of a wild field microscope in order to validate the proposed method. This PSF model is implemented as an ImageJ plugin.

Acquisition gives the closest result to the system's true PSF. Actually, one should acquire a small light source having its diameter less than the system's resolution, and so it might be considered as a point like source. This method gives the most accurate PSF but usually it is corrupted by noise. Such case is treated in chapter 4.

2.2. PSF NON-INVARIANCE

Usually the PSF is considered as shift invariant into the object space, but in 3D images this assumption does not necessarily holds, due to the refraction induced by the variations in the specimen's refractive index [6] and the depth variation [7]. If the specimen is homogenous, the error induced by the refractive index variation can be safely neglected. Never less, the depth variation, in particular when there is a refractive index mismatch between the specimen and the immersion medium, it introduces large aberrations in 3D fluorescence imaging. The manifestation of this aberration is an axial asymmetry in the shape of the point spread function, with a corresponding increase in size, particularly along the z-axis [8].

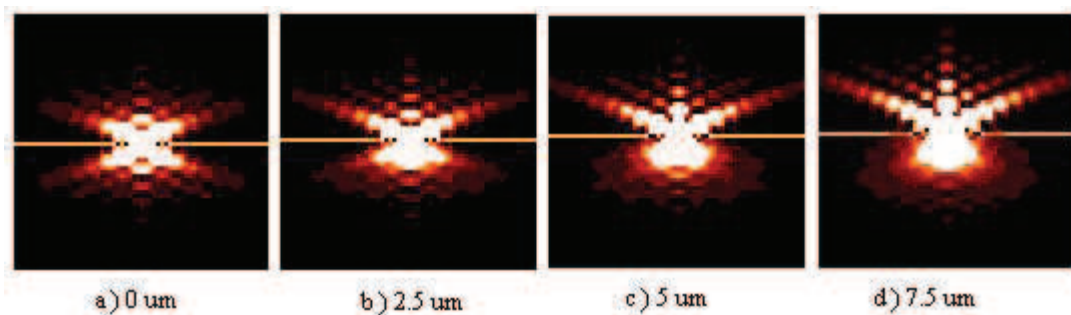


FIG. 1: PSF CALCULATED FOR A WIDE FIELD MICROSCOPE AT DIFFERENT DEPTHS UNDER THE COVER-SLIP: INCREASE OF AXIAL EXTENT ALONG THE Z-AXIS IS CLEARLY VISIBLE. (NA: 1.2, WAVELENGTH: 630 NM, OBJECTIVE X100)

Fig. 1 shows four PSF calculated at different depths for a microscope with a numerical aperture of 1.2 and a light of wavelength equals to 630nm. One can easily notice the large variation introduced at 7.5 μ m of depth (the center points are intentionally saturated so the low intensity details can be shown).

Holding the space-invariance assumption while using a system having such variations will lead to large quantitative errors into the estimated image. Although some microscope objectives can be adjusted to be aberration free at planes deep under the cover slip, they are aberration free only for the depth they were corrected for and lose their interest in 3D acquisition. In this chapter we will discuss the non-invariance case and the solutions proposed in the literature. A new algorithm is proposed capable of transforming any existing deconvolution algorithm based on depth-invariant assumption into a solution for the non-invariance problem. Tests are carried on simulated data to validate the process using our algorithm combined with both linear and statistical based algorithms.

2.3. AVAILABLE NON-INVARIANCE SOLUTIONS

As stated before, when the PSF is shift-invariant, the discrete representation of the kernel is a Toeplitz matrix with banded Toeplitz blocks of dimensions $[n^3 \times n^3]$ assuming a 3D cubic image of $[n \times n \times n]$ dimension. In such matrix form, the vector multiplications can be efficiently done, otherwise, the kernel's discrete form may not have any special structure thus the matrix vector multiplication can be extremely expensive, even for moderate value of n , unless the matrix is separable which mean that the PSF matrix can be written as Kronecker products of smaller matrixes. E. S. Angel and A. K. Jain [9] used this method in 1978 to restore 2D images blurred with space variable Gaussian blur using a conjugate gradient method. However for 3D microscopy images, PSF matrixes are too large and complex that decomposing it to Kronecker products is not a straightforward task.

One of the earliest technique to deal with space varying blur is the use of geometrical coordinate transformation [10] [11] in order to transform a variable PSF to a shift-invariant one. In such case the deconvolution can be performed in an invariance assumption then an inverse geometrical transformation is applied on the result. This technique is very difficult to apply on a complex 3D system.

The most straightforward and general solution is to implement a space-variant convolution process using spatial convolution:

$$g(x, y, z) = \iiint f(u, v, w)h(u, v, w, x-u, y-v, z-w) dudvdw \quad (2.1)$$

Where (x, y, z) are any voxel location in the resulting image g , (u, v, w) are the voxel locations in the object space f and h is the PSF at a certain point in the object space. This equation can be easily used with depth variant PSF where it varies only along the optical axis (w coordinate) and the discrete form of such spatial convolution can be written as:

$$g(x, y, z) = \sum_{u=0}^{N_x} \sum_{v=0}^{N_y} \sum_{w=0}^{N_z} f(u, v, w)h_{(w)}(x-u, y-v, z-w) \quad (2.2)$$

This solution may offer a primary approach for the non-invariance problem, but it is very costly in term of processing time. As for a single convolution with $[s \times s \times s]$ dimensions kernels assuming a $[n \times n \times n]$ dimensions image one should process $3n^3s^3$ arithmetic operations.

In order to speed up the process, the most used approaches in literature consist on sectioning the object space into sub-regions, where the PSF variations are minimal and it can be considered as invariant. Trussell and Hunt [12] used this technique in 2D imagery in 1978 using Landweber iteration. Fish, Grochmalicki and Pike [13] used a truncated singular value decomposition method in 1996 for 2D astronomical images. James G. Nagy and Dianne P. O'Leary in 1997 described various procedures to apply the sub-block technique for 2D convolution using fast Fourier transform (FFT) [14] and proposed linear interpolation for the PSF, where the variant PSF are sewed together using linear interpolation scheme, in order to reduce the mosaic effect, and then the image is restored globally using a conjugate gradient method [15].

Inspired by the work in astronomical field, C. Preza and J. Conchello proposed the decomposition of the 3D image into stratum along the optical axis, where the PSF is considered as invariant, then developed a space variant PSF convolution model for 3D images [16]. In 2004 Preza and Conchello introduced to their model a PSF weighted interpolation to reduce the mosaic effect; this method assigns to each stratum an interpolated PSF between the PSF at the top and the end of the stratum. This model is then implemented into an ML-EM (Maximum Likelihood - Expectation Maximization) deconvolution algorithm [17].

In the following section we propose an algorithm that can adapt to any existing classical deconvolution algorithm (using the invariance assumption) to the depth varying PSF problem. The presented algorithm, EMMA (Evolutive Merging Mask Algorithm), can be used in addition with any classical deconvolution algorithm (chosen accordingly to the data and noise pollution) without any modification to the later, and with any number of known PSF at different depths, to yield a 3D non-invariant PSF deconvolution.

2.4. EMMA – EVOLUTIVE MERGING MASKS ALGORITHM

EMMA is based on the observation that in the case of a system having spatial PSF variations through depth, deconvolving an acquired image with an invariance assumption, using a generalized PSF at a depth “k”, yields a result having its minimum errors in the region surrounding the position “k” of the used PSF.

Having a set of PSF at different depths, multiple deconvolution process can be done, each with a different PSF, using any classical algorithm, the results are then merged together using an adequate mask that takes the best of each part to form the final estimated image.

The resulting estimation can be expressed as:

$$\hat{f} = \sum_{i=0}^n \hat{E}_i \times D_i \quad \text{where} \quad \hat{E}_i = f \otimes^{-1} h_i \quad (2.3)$$

\hat{E}_i is the i^{th} deconvolution estimation using the adequate h_i PSF and mask D_i for this deconvolution.

2.4.1. MERGING MASK

In order to merge the convolution results into a final estimated image, having the best estimated part of each, a set of 3D Masks must be created. These masks play the role of weighted merging function that assures the use of the best estimation of each, and a smooth transition between blocks along the optical axis.

As the merged images are the restored ones, and by assuming that the error function increases linearly along the distance to the used PSF position, the merging masks used have a linear nature and depends only on the used PSF positions.

The grayscale variations in the masks are only through the Z axis, their values are uniform in the same slice (as the PSF non-invariance in this study is considered only along the optical axis).

The masks are formed according to the used PSF positions in the object space, hence the name “evolutive”. For each deconvolution, the used PSF is considered along with the previous and next PSFs using this method:

- The pixels at the used PSF plane position have the grayscale value of 1
- The pixel values in next and previous planes Decrease linearly till it reaches 0 at the next and previous PSF positions (formula 1).
- The pixels in the remaining planes are set to 0.
- If it is the last PSF all next planes are set to 1
- If it is the first PSF all previous planes are set to 1

The pixel values of an intermediate plane are calculated according to the following formula:

$$\left\{ \begin{array}{ll} (n - p_p) \cdot \left(\frac{1}{p_c - p_p} \right) & p_p \leq n < p_c \\ 1 - \left[(n - p_c) \cdot \left(\frac{1}{p_n - p_c} \right) \right] & p_c < n < p_n \\ 1 & n = p_c \end{array} \right. \quad (2.4)$$

Where p_p , p_c and p_n denote respectively the positions of the previous, current and next PSF and n denotes the slice depth in the mask stack.

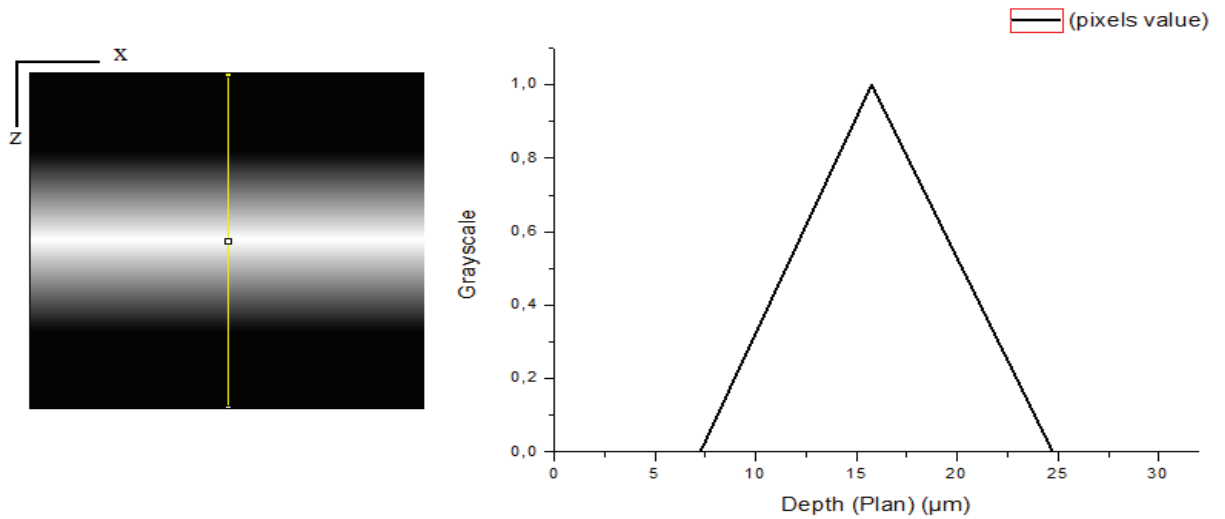


FIG. 2: EXAMPLE OF A MASK ASSOCIATED TO A PSF AT 15.75 μm WITH PREVIOUS AND NEXT PSFS AT POSITIONS 7.25 μm AND 24.75 μm . AT LEFT AN X-Z SLICE OF THE MASK.

An example of a mask associated to the deconvolution using a PSF at 15.75 μm with previous and next PSFs at positions 7.25 μm and 24.75 μm respectively is represented in Fig. 2.

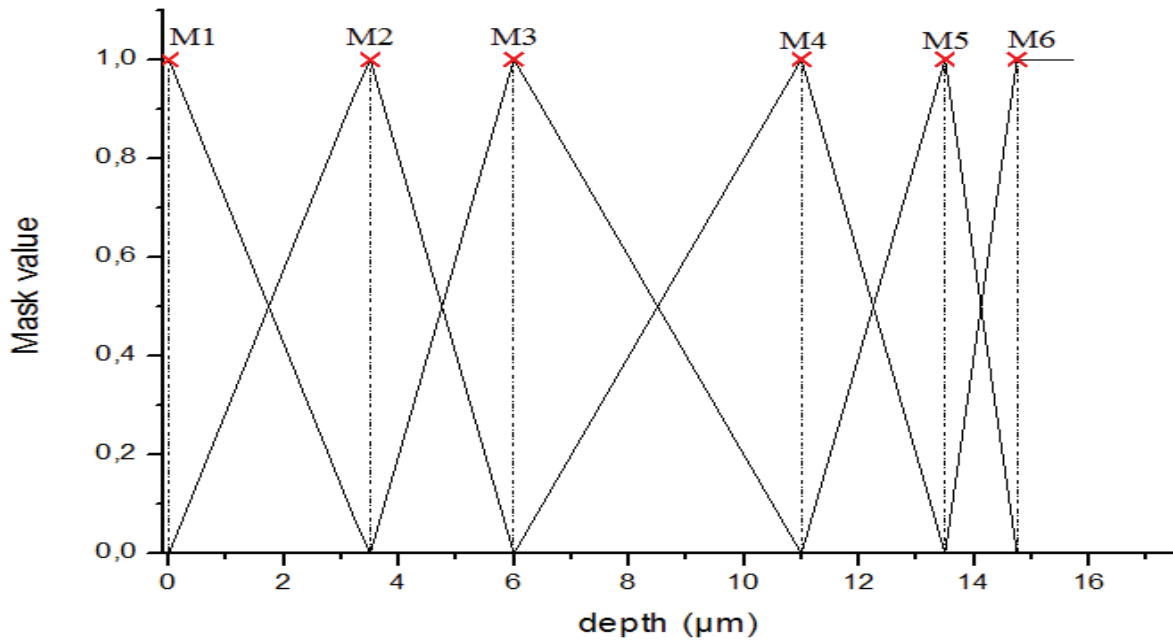


FIG. 3: EXAMPLE OF A SET OF 6 MASKS FOR A DECONVOLUTION WITH 6 PSF. (M1: $0\mu\text{m}$) – (M2: $3.5\mu\text{m}$) – (M3: $6\mu\text{m}$) – (M4: $11\mu\text{m}$) – (M5: $13.5\mu\text{m}$) AND (M6: $14.75\mu\text{m}$).

The Fig. 3 shows a set of masks associated to a non-invariance blur deconvolution with 6 PSF at depth 0, 3.5, 6, 11, 13.5 and $14.75\mu\text{m}$ over a global sample depth of $16\mu\text{m}$. one can see the last mask with the part passing $14.75\mu\text{m}$ is set to 1 till the end of the sample depth.

2.5. TEST AND RESULTS

Our tests were conducted over simulated images; this offers the advantage of a known object and the ability to calculate PSF at any depth needed.

We use two synthesized objects, the first consist of 4 spherical beads having a diameter of $2.25\mu\text{m}$ spaced by $5\mu\text{m}$ along the optical axis, and the center of the first bead is placed at $5.25\mu\text{m}$ of depth (Fig. 4– a, a’).

The second is a rectangular parallelepiped placed along the Z axis; we intentionally smoothed the edges to limit the high frequencies artifact when using the LLS algorithm. This object is $20.75\mu\text{m}$ along the Z and $2.25\mu\text{m}$ along x and y (Fig. 4 – c, c’).

The acquisitions are simulated considering a wide field fluorescence microscope with $0.25\mu\text{m}$ resolution along the optical axis and $0.068\mu\text{m}$ in x-y axis, numerical aperture of 1.2, a 100X lateral magnification and an oil immersed objective. The system presents a spatial non-invariance of the PSF, in order to simulate these variations; one can use a spatial convolution according to formula (2.2). We use a different PSF for each slice.

This convolution method yields a lengthy and heavy computational load but guarantees the most accurate simulation to the space variant blur.

The PSF are calculated using the Tôrôk and Varga vectorial model (modified by Olivier Haeberlé) [5] , using the same parameters for the microscope and an emission light wavelength of 512nm.

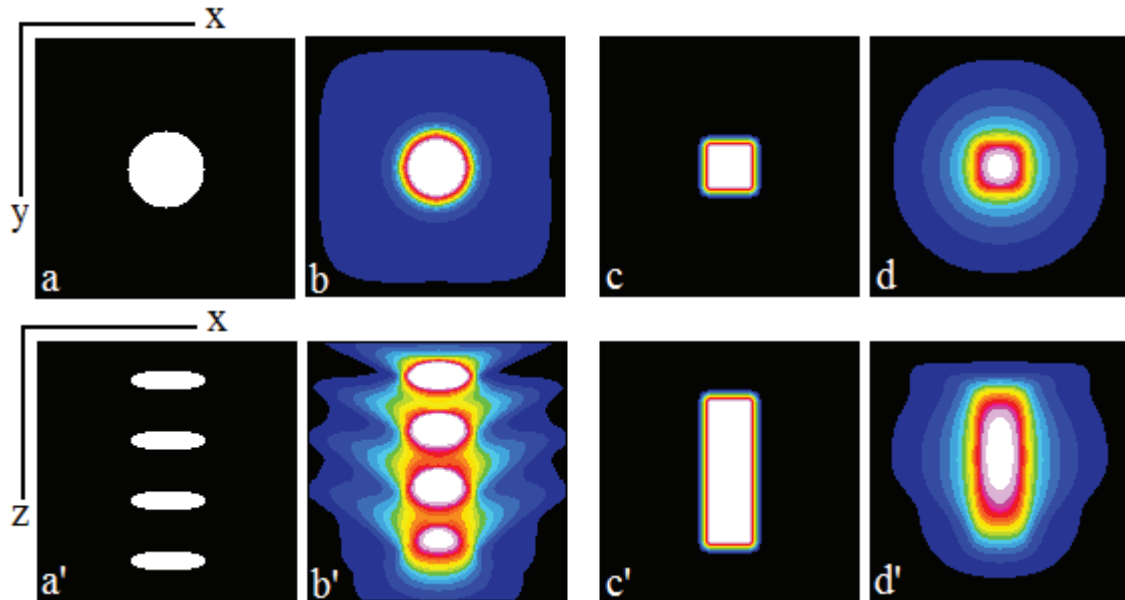


FIG. 4: SYNTHETIC OBJECTS AND THE ACQUISITIONS SIMULATION: (a) FIRST BEAD IN THE OBJECT SPACE IN AN X-Y SLICE. (a') AN X-Z SLICE IN THE OBJECT SPACE SHOWING THE FOUR BEADS. (b – b') X-Y AND X-Z SLICES RESPECTIVELY IN THE IMAGE SPACE SIMULATING AN ACQUISITION USING A SYSTEM WITH SPACE VARYING PSF. (c – c') X-Y AND X-Z SLICES RESPECTIVELY IN THE OBJECT SPACE REPRESENTING A RECTANGULAR PARALLELEPIPED. (d – d') X-Y AND X-Z SLICES RESPECTIVELY IN THE IMAGE SPACE REPRESENTING AN ACQUISITION USING A SYSTEM WITH SPACE VARYING PSF.

Fig. 4 shows the original objects (in object space) and the acquired images simulated for a system having a spatial non-invariance of the PSF along the optical axis. For each object we show an x-y slice and an x-z slice in object space and in image space respectively, the images are in 16 Color LUT to show easily the intensity variations and the blur spreading. For the rest of this manuscript only x-z slices will be showed, as the blur studied is along the optical axis only.

Fig. 5 and Fig. 6 shows the intensity profiles comparison of the object and the acquisition, the profiles are traced along the optical axis passing by the center of the object(s), for each object we represent the real and observed intensities and a comparison using normalized data.

Chapter 2

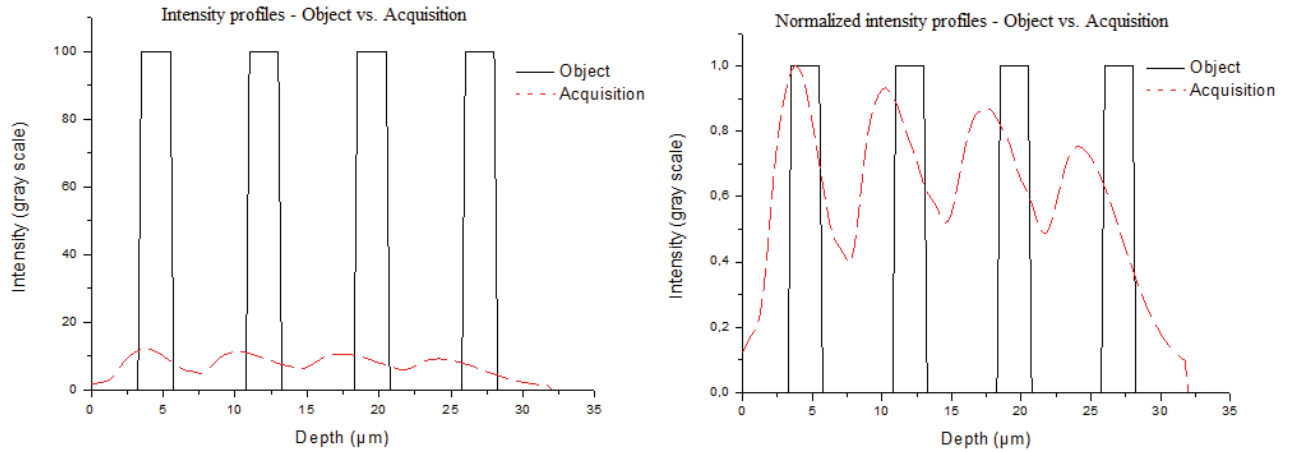


FIG. 5: (LEFT) INTENSITY PROFILES OF THE FOUR BEADS INTO THE OBJECT SPACE (REAL DATA) AND IN THE IMAGE SPACE (MEASURED DATA). THE PROFILES ARE MEASURED ALONG THE OPTICAL AXIS PASSING THROUGH THE CENTER OF THE BEADS. (RIGHT) NORMALIZED INTENSITY PROFILES IN ORDER TO SEE BETTER THE NON INVARIANCE EFFECT.

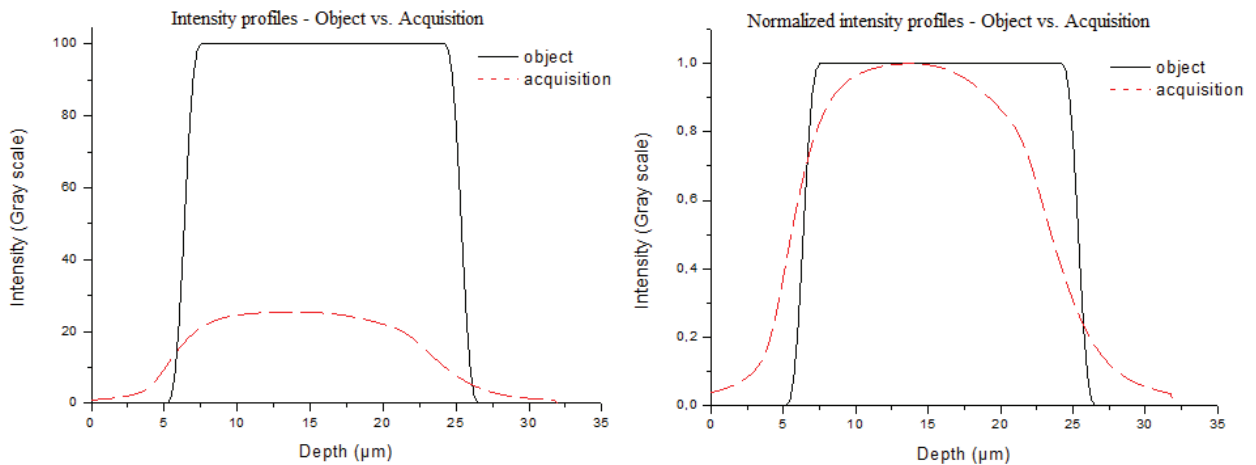


FIG. 6: (LEFT) INTENSITY PROFILES OF THE RECTANGULAR PARALLELEPIPED INTO THE OBJECT SPACE (REAL DATA) AND IN THE IMAGE SPACE (MEASURED DATA). THE PROFILES ARE MEASURED ALONG THE OPTICAL AXIS PASSING THROUGH THE CENTER OF THE OBJECT. (RIGHT) NORMALIZED INTENSITY PROFILES TO SEE BETTER THE NON INVARIANCE EFFECT

It can be seen that the acquired images present loss of intensities with depth and asymmetry along the Z axis, the resolved center of the beads (max intensity) is more shifted toward the origin (cover slip direction) with depth making the beads look closer. The rectangular parallelepiped look more degraded with depth.

2.5.1. RESTORATION

The two simulated images described are restored using EMMA in association with the direct inversion Linear Least Square algorithm (LLS) and Lucy-Richardson, a statistical based iterative method. Both algorithms are used as described into literature without any modification or adaptation to the non-invariance problem.

The results are then compared with deconvolutions without EMMA using the same deconvolution algorithms, and original data. A visual comparison is performed by showing the images in 16 color LUT, a qualitative one by comparing intensity profiles and a quantitative one by comparing the objects measurements and calculating the error percentage. One should keep in mind that the restoration quality highly depends on the parameters used in the deconvolution algorithm and the number of PSF used. We shall use the parameters that yield a best result for the classical deconvolution (invariant assumption) with our tests.

The most used approach to deal with non-invariance in the literature as shown before is to divide the object space into subspaces where the PSF variations may be considered as insignificant; we decided to use this as a basis to choose our PSF where we assume that 10% of variation (resemblance been calculated using the correlation coefficient) is the maximal accepted variation. The positions of the PSF to be used are defined in a way to have 10% variation each according to the previous, starting with the PSF at $0\mu\text{m}$ (as the PSF under the cover-slip are the easiest to measure). To define these positions, the correlation coefficient of the PSF is calculated at each depth relatively to the $0\mu\text{m}$ PSF, then we define the position of the PSF having 10% variation, the new PSF becomes the new reference and the process loops back.

The Fig. 7 shows the consecutive correlation coefficient variation and the subspaces defined within the 10% tolerance. We can see that, under the current optical settings, the variation become slower with depth and thereby the number of PSF needed become lesser by depth

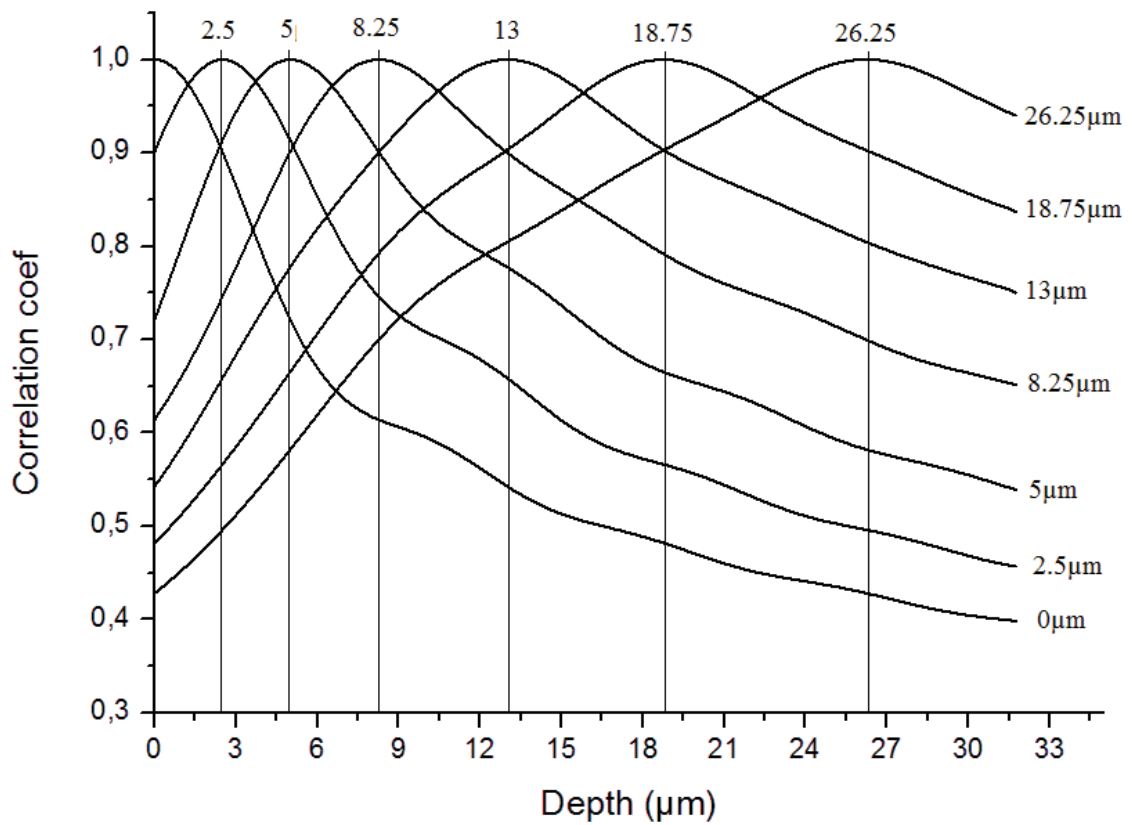


FIG. 7: CORRELATION COEFFICIENT VARIATIONS BETWEEN A REFERENCE PSF AND EACH PSF AT DIFFERENT DEPTHS. THESE CURVES ARE USED TO DEFINE PSF POSITIONS REPRESENTING 10% VARIATION TO THE PREVIOUS ONE STARTING BY THE PSF AT $0\mu\text{m}$. WE FIND 7 PSF TO BE USED.

According to this assumption, we will use 7 PSF at positions 0, 2.5, 5, 8.25, 13, 18.75 and $26.25\mu\text{m}$.

We need to emphasize on the fact that the quality of the deconvolution result highly depends on the number of PSF used and their positions, optimally one should use a PSF for each single slice, we have chosen the later setting for more realistic conditions.

2.5.1.1. EMMA-LLS

The first test is performed associating EMMA with the linear least squares (LLS) algorithm, this kind of algorithms are fast and yield very satisfactory results when the data and specially the PSF measured are of high quality with high signal to noise ratio (therefore the noise can be estimated to a Gaussian distribution). LLS drawbacks are artifacts (ringing) produced by high frequency edges and discontinuity in data.

Fig. 8 shows both objects deconvolutions using EMMA associated with LLS using the settings described above, compared with, deconvolutions using LLS and the invariance assumption (PSF at $0\mu\text{m}$). The regularization parameter commonly noted λ is the same for both deconvolutions. One can easily see the quality of restoration using EMMA all along the optical axis.

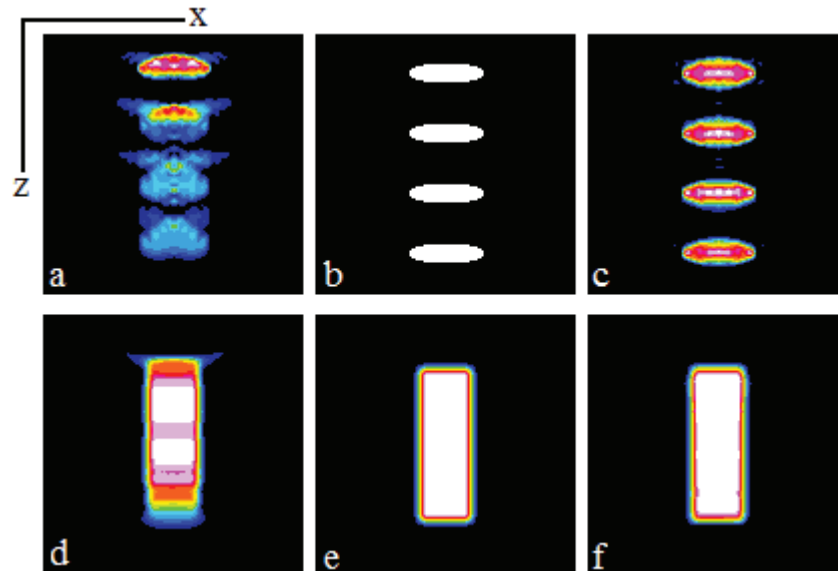


FIG. 8: (a - d) RESTORATION USING LLS IN THE DEPTH INVARIANCE PSF ASSUMPTION (PSF $0\mu\text{m}$). (b - e) THE ORIGINAL OBJECTS. (c - f) RESTORATION USING EMMA ASSOCIATED WITH LLS ALGORITHM AND 7 PSF AT DIFFERENT DEPTHS.

Chapter 2

The intensity profile along the Z axis passing through the center of the four beads object shown in the Fig. 9, demonstrates a good restoration of the intensity values and also the beads center positions when using EMMA (LLS-DV), meanwhile the last two beads are chaotically restored in the depth invariant deconvolution (LLS – DIV).

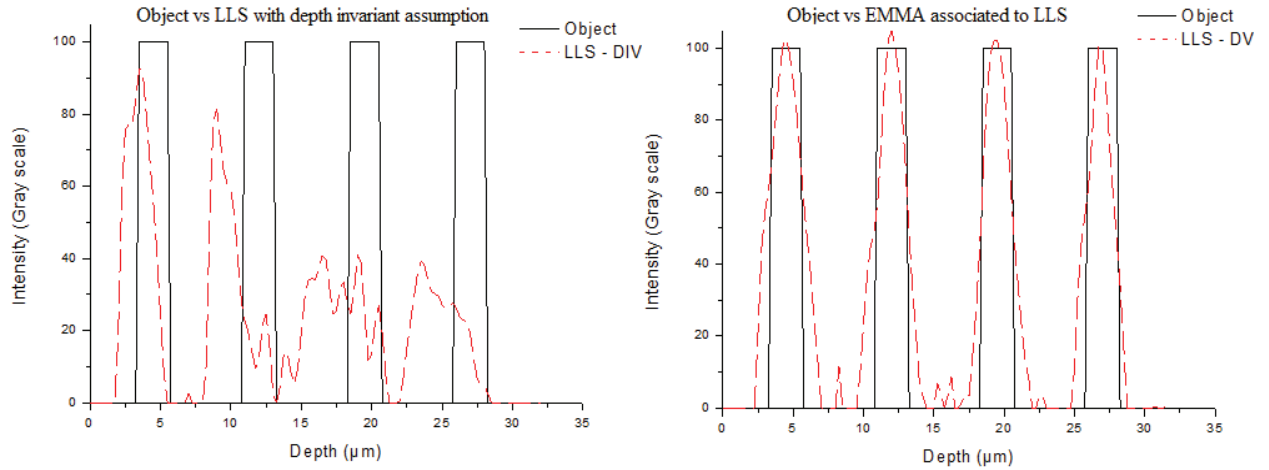


FIG. 9: INTENSITY PROFILES OF (LEFT) RESTORATION USING LLS AND THE DEPTH INVARIANCE PSF ASSUMPTION (PSF $0\mu\text{m}$) AND (RIGHT) RESTORATION USING EMMA ASSOCIATED WITH LLS ALGORITHM AND 7 PSF AT DIFFERENT DEPTHS.

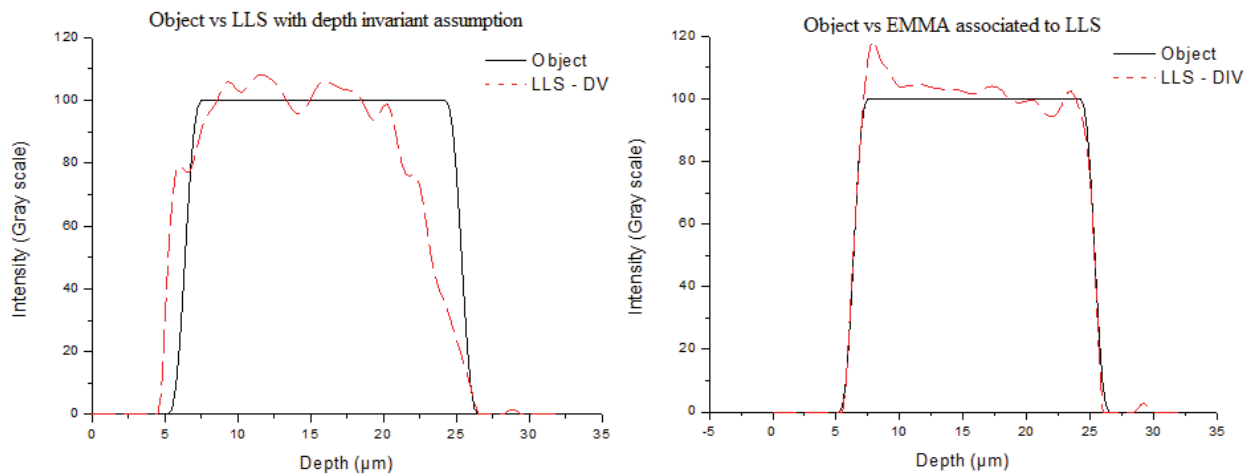


FIG. 10: INTENSITY PROFILES OF (LEFT) RESTORATION USING LLS AND THE DEPTH INVARIANCE PSF ASSUMPTION (PSF $0\mu\text{m}$). (RIGHT) RESTORATION USING EMMA ASSOCIATED WITH LLS ALGORITHM AND 7 PSF AT DIFFERENT DEPTHS.

Chapter 2

In Fig. 10 one can notice a good restoration of the parallelepiped edges positions, which cannot be seen over the classical (depth invariance) deconvolution.

The following table compares in a quantitative point of view the results obtained from a depth invariant PSF deconvolution using LLS (LLS-DIV), a deconvolution done with EMMA with LLS (EMMA – LLS) and the original data. The size of the object is measured along the Z axis after applying a threshold at half maximum (50%). The correlation coefficient of each bead is measured separately after extraction of the latter into a separate volume.

	Bead 1	Bead 2	Bead 3	Bead 4	Parallelepiped
Original size along Z axis	2.25 μ m	2.25 μ m	2.25 μ m	2.25 μ m	18.75 μ m
Measured LLS - DIV	2.5 μ m	1.5 μ m	-	-	18 μ m
Measured EMMA - LLS	2.75 μ m	2.25 μ m	2.25 μ	2 μ m	18.75 μ m
3D correlation coef. LLS - DIV	0.917	0.778	0.429	0.345	0.961
3D correlation coef EMMA - LLS	0.926	0.937	0.938	0.937	0.998

These numbers above reflect a very good reconstruction of the objects, especially in the case of the beads, where we can notice an error of $\pm 0.25\mu\text{m}$ over all the set of beads in contrast to the classical approach where the beads are not even resolved in depth, and a correlation coefficient jump from 0.345 up to 0.937 in the case of the deepest bead. In the case of the parallelepiped the measurement is exact with a correlation coefficient of 0.998 when using EMMA.

2.5.1.2. EMMA-LUCY RICHARDSON

Lucy- Richardson method follows a statistical approach to the deconvolution problem (see chapter 1), it uses Poisson statistic, which make it suitable for images with low signal to noise ratio usually acquired in low luminosity circumstances where the noise is estimated to be Poisson distribution.

In this section we will repeat the tests presented above while associating EMMA this time with Lucy-Richardson method.

Fig. 11 show the central slices along the optical axis of the original objects and their restorations, one using EMMA associated with Lucy-Richardson method and the other using Lucy-Richardson with the depth invariance PSF assumption. Both restorations used 100 iterations.

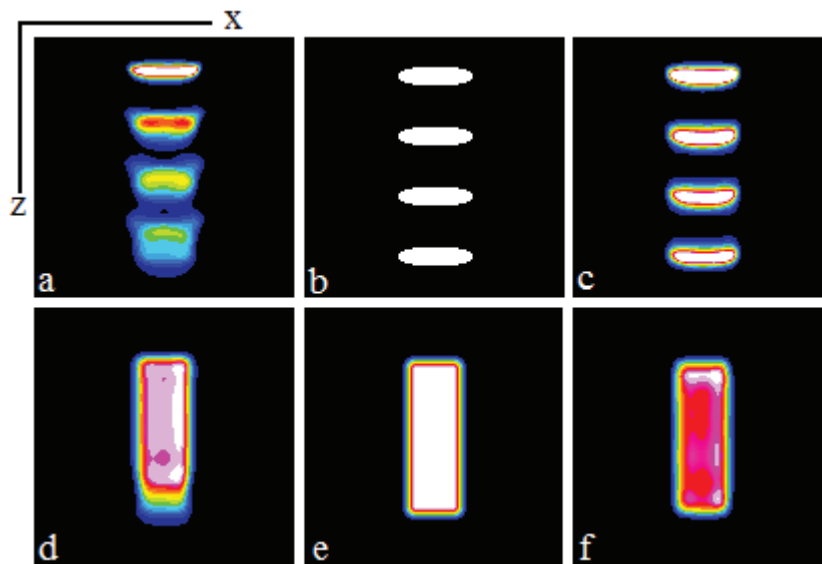


FIG. 11: (a - d) RESTORATION USING LUCY-RICHARDSON AND THE DEPTH INVARIANCE PSF ASSUMPTION (PSF $0\mu\text{m}$). (b - e) THE ORIGINAL OBJECTS. (c - f) RESTORATION USING EMMA ASSOCIATED WITH LUCY-RICHARDSON METHOD AND 7 PSF AT DIFFERENT DEPTHS.

Fig. 12 and Fig. 13 show the intensity profiles along the optical axis passing through the center of the objects. As with LLS, the beads restoration worsen with depth when the depth invariance is assumed, while it is well restored when EMMA is used.

Chapter 2

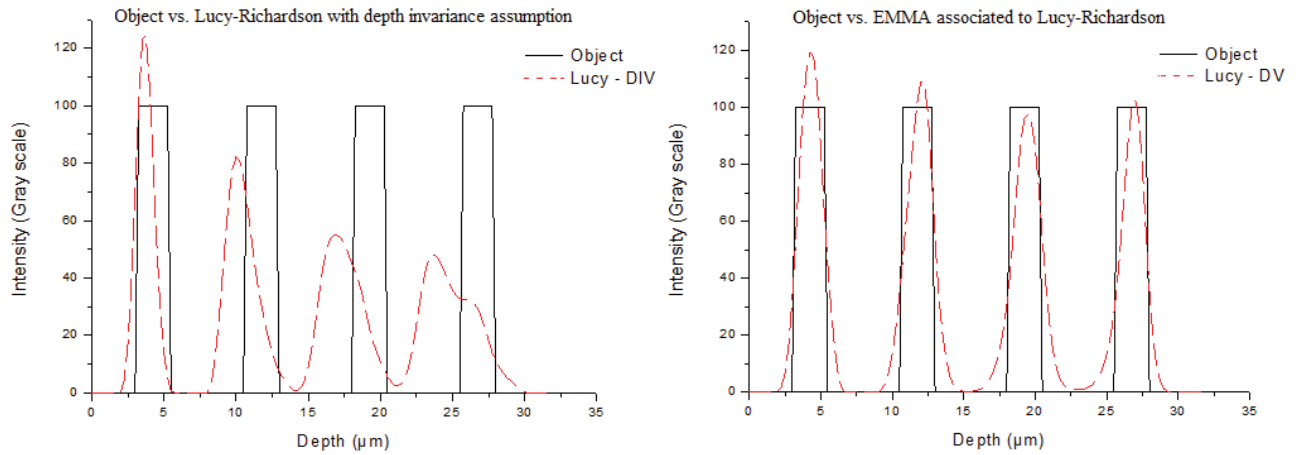


FIG. 12: (LEFT) RESTORATION USING LUCY-RICHARDSON METHOD AND THE DEPTH INVARIANCE PSF ASSUMPTION (PSF $0\mu\text{m}$). (RIGHT) RESTORATION USING EMMA ASSOCIATED WITH LUCY-RICHARDSON AND 7 PSF AT DIFFERENT DEPTHS.

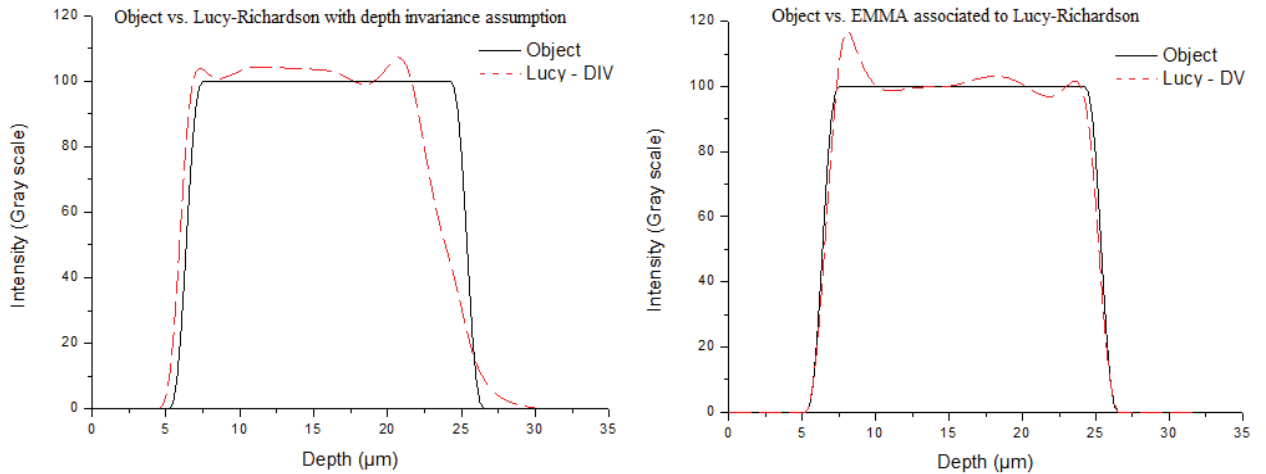


FIG. 13: (LEFT) RESTORATION USING LUCY-RICHARDSON AND THE DEPTH INVARIANCE PSF ASSUMPTION (PSF $0\mu\text{m}$). (RIGHT) RESTORATION USING EMMA ASSOCIATED WITH LUCY-RICHARDSON METHOD AND 7 PSF AT DIFFERENT DEPTHS.

The following table, resume as in the LLS case, a series of quantification measurements. The diameters along the Z axis are measured at mid height (thresholding to 50%). When using EMMA the diameter restoration yield exact for the first three with only $0.25\mu\text{m}$ error (1 pixel) for the third. The correlation coefficient calculated for each separate bead (extracted and re-centered) is high and stable along the depth when using EMMA.

	Bead 1	Bead 2	Bead 3	Bead 4	Parallelepiped
Original size along Z axis	2.25 μ m	2.25 μ m	2.25 μ m	2.25 μ m	18.75 μ m
Measured L-R - DIV	1.75 μ m	2 μ m	1.25 μ m	-	17.75
Measured EMMA – L-R	2.25 μ m	2.25 μ m	2.25 μ m	2 μ m	18.25
3D correlation coef. L-R - DIV	0.873	0.831	0.728	0.585	0.964
3D correlation coef EMMA – L-R	0.894	0.876	0.866	0.876	0.992

2.5.2. EMMA OPTIMIZATION

Many optimizations can be applied on EMMA in order to gain in efficiency and speed; we propose the use of the following techniques:

Parallel computing:

As deconvolution processes in EMMA are totally independent of each others, a parallel architecture can be easily implemented for the deconvolution stage. This technique would speed up computing time especially when executed on multiple core computers (8 threads with Xeon or i7 Intel CPU – widely used).

Using GPU:

The current mid-range graphic cards are equipped with powerful GPUs (Graphical Processing Unit) that can be composed with up to 680 million transistors (NVIDIA G8800 GTX) and beyond for top-range cards and high memory bandwidth. Unlike CPUs however, GPUs have a parallel throughput architecture that emphasizes executing many concurrent threads, therefore coding multithreaded EMMA for GPU execution would yield an extreme acceleration of the process.

GPU coding might be done using CUDA for NVidia cards, ATI Stream for ATI cards. To be able to execute the code on both cards type and over CPUs in the case where a non-compatible card existed, OpenCL can then be used despite a possible loss of specialized architecture optimization.

Adaptive regularization parameters and iteration number:

The regularization constant and the iteration number are very important parameters in the deconvolution algorithms, these parameters are usually set empirically by the user based on his experience. To ensure the use of the best value we propose the use of automatic methods to set these variables. For simplicity we decided to use the same value for all deconvolutions with the different PSF in EMMA, but to ensure the best result one should set the adequate value for each deconvolution which would yield the best estimation in the sub-region of interest.

The automatic determination of regularization parameter depends on the deconvolution method used.

For LLS like algorithms we propose a modified version of Bruno Colicchio automatic determination of regularization parameter [18] applied on each deconvolution and where the bias error is calculated only in the sub-region of interest. This method can be paralyzed with some computation skills.

For iterative algorithms, the bias error can be calculated in the sub-region of interest for each deconvolution at the end of each iteration. If the new bias error is bigger than the previous one or it is lesser by an epsilon, the deconvolution of the sub-region stops and the previous result is used; when all sub-regions are deconvolved the final estimation is then constructed (Fig. 14)

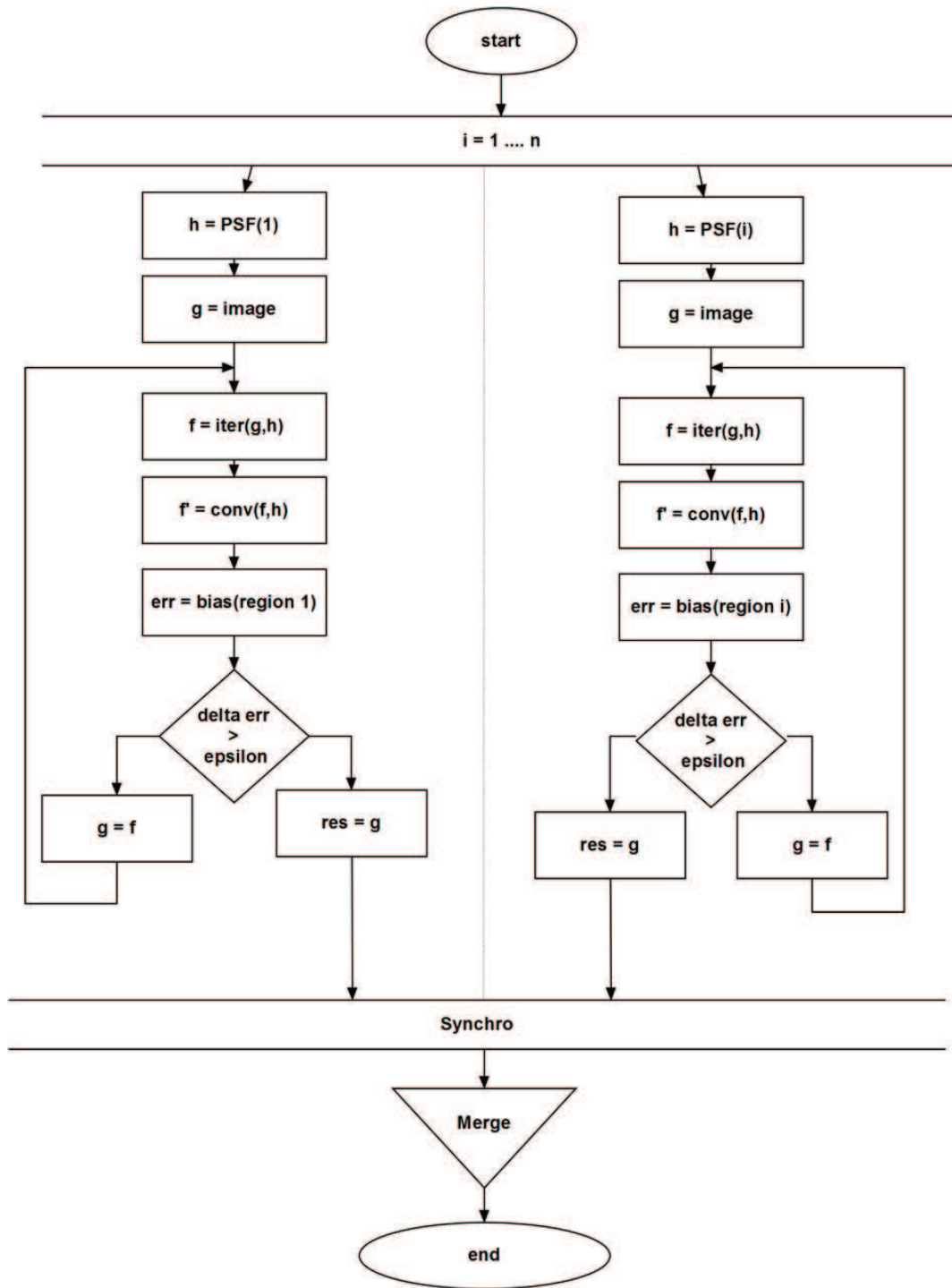


FIG. 14: AUTOMATIC ITERATION NUMBER FOR ITERATIVE ALGORITHMS ASSOCIATED WITH EMMA

2.6. CONCLUSION

We proposed a simple, yet a powerful method, that when associated with any deconvolution algorithm and a set of PSF at different positions, it becomes an effective solution for the depth variant PSF deconvolution.

EMMA itself is not a deconvolution algorithm, rather, an add-on for the depth non-invariant solution. This approach gives the flexibility to choose the adapted algorithm for the existing data accordingly to applications needs, not to mention the ease of its implementation that demands no modification to the deconvolution algorithm chosen. We performed the test using two algorithms representing a direct inversion and an iterative one.

we performed tests on simulated data having the advantage of knowing the original object is, hence the possibility to quantify the restoration quality. The restored image quality highly depend on the number of PSF used by the process, this number can change from a single PSF, transforming the case into a classical space invariant deconvolution, up till a PSF for each slice which yield the best result.

As measuring PSF is the main limitation, we chosen to limit the number of our PSF, and to avoid arbitrary choices, the number and positions we used are based on a common approach in literature where the space is divided into subspaces where the PSF variation is limited. We assumed that the variation is 10%.

In the results section one can see the quality of restoration when using EMMA, demonstrated by a visual comparison and quantitative measurements.

To enhance the results of deconvolution without the need of measuring more PSF, we propose in the next chapter a PSF interpolation technique based on Zernike polynomials which will help to interpolate more PSF from the existing ones at different depths with a high precision.

2.7. REFERENCES

1. J. G. McNally, T. Karpova, J. Cooper, et J. A. Conchello, "Three-Dimensional Imaging by Deconvolution Microscopy," *Methods* **19**, 373-385 (1999).
2. P. PANKAJAKSHAN, "Blind Deconvolution for Confocal Laser Scanning Microscopy," (2009).
3. S. F. Gibson et F. Lanni, "Diffraction by a circular aperture as a model for three-dimensional optical microscopy," *J. Opt. Soc. Am. A* **6**, 1357-1367 (1989).
4. P. Török, P. Varga, Z. Laczik, et G. R. Booker, "Electromagnetic diffraction of light focused through a planar interface between materials of mismatched refractive indices: an integral representation," *J. Opt. Soc. Am. A* **12**, 325-332 (1995).
5. O. Haeberlé, "Focusing of light through a stratified medium: a practical approach for computing microscope point spread functions. Part I: Conventional microscopy," *Optics Communications* **216**, 55-63 (2003).
6. C. J. R. Sheppard et P. Török, "Effects of specimen refractive index on confocal imaging," *Journal of Microscopy* **185**, 366-374 (1997).
7. J. G. McNally, C. Preza, J. Conchello, et L. J. Thomas, "Artifacts in computational optical-sectioning microscopy," *J. Opt. Soc. Am. A* **11**, 1056-1067 (1994).
8. A. Dieterlen, C. Xu, A. Chomik, J. J. Meyer, G. Jung, et S. Jacquy, "Artefacts due to shift variant and quasi-monochromatic image formation in 3D reconstruction by sectioning microscopy," *Analytical cellular pathology* **13**, 173 (1997).
9. E. S. Angel et A. K. Jain, "Restoration of images degraded by spatially varying pointspread functions by a conjugate gradient method," *Appl. Opt.* **17**, 2186-2190 (1978).
10. S. R. McNown et B. R. Hunt, "Approximate Shift-Invariance by Warping Shift-Variant Systems," <http://adsabs.harvard.edu/abs/1994rhis.conf..181M>.
11. S. R. McNown et B. R. Hunt, "Approximate Shift-Invariance by Warping Shift-Variant Systems," <http://adsabs.harvard.edu/abs/1994rhis.conf..181M>.
12. H. Trussell et B. Hunt, "Image restoration of space-variant blurs by sectioned methods," *IEEE Transactions, Acoustics, Speech and Signal Processing* **26**, 608 - 609 (1978).
13. D. A. Fish, J. Grochmalicki, et E. R. Pike, "Scanning singular-value-decomposition method for restoration of images with space-variant blur," *J. Opt. Soc. Am. A* **13**, 464-469 (1996).
14. J. G. Nagy, R. J. Plemmons, et T. C. Torgersen, "Iterative image restoration using approximate inverse preconditioning," *IEEE Trans Image Process* **5**, 1151-1162 (1996).
15. J. G. Nagy et D. P. O'Leary, "Restoring Images Degraded by Spatially Variant Blur," *SIAM J. Sci. Comput.* **19**, 1063-1082 (1998).
16. C. Preza, "Image estimation accounting for point-spread function depth variation in three-dimensional fluorescence microscopy," dans (2003), p. 135-142.
17. C. Preza et J. Conchello, "Depth-variant maximum-likelihood restoration for three-dimensional fluorescence microscopy," *J. Opt. Soc. Am. A* **21**, 1593-1601 (2004).
18. B. Colicchio, O. Haeberlé, C. Xu, A. Dieterlen, et G. Jung, "Improvement of the LLS and MAP deconvolution algorithms by automatic determination of optimal regularization parameters and pre-filtering of original data," *Optics Communications* **244**, 37-49 (2005).

3. ZERNIKE INTERPOLATION

DO NOT WORRY ABOUT YOUR DIFFICULTIES IN
MATHEMATICS. I CAN ASSURE YOU MINE ARE STILL
GREATER.
ALBERT EINSTEIN

3.1. INTRODUCTION

When using a deconvolution algorithm with a depth-varying PSF, multiple PSF measurements at different depths become mandatory, furthermore, the number of known PSF directly affects the deconvolution quality. This will be shown in the next chapter.

One can either use a mathematical model to calculate the PSF at different depths or measure sub-resolution beads that can be assimilated to punctual light sources and hence their images represents the point source function of the system [1]. The use of measured PSF offers the advantage of taking into account the aberrations of the entire optical system, which a mathematical model based on ideal numerical values fails to do so [2] especially with the aberrations induced by the specimen's refractive index [3] [4].

In this chapter, we expose the various methods presented in the literature that can be used to obtain multiple measured PSF or measured-like PSF at different depths. These PSF can be used in depth-variant deconvolution algorithms.

An algorithm, based on Zernike moments, for measured PSF's interpolation is then described. This algorithm offers the possibility of accurately interpolating PSF at different depths using only few known ones.

3.2. PSF EXTRACTION METHODS

As measuring PSF at various depths can be a complicated task, some techniques attempt to adjust the parameters of a mathematical model to be as close as possible to the actual measurement values by recovering data from an experimental PSF [5]. Another method proposes a simplified model with a restrained set of parameters that can be adjusted using two measured PSF and a maximum likelihood algorithm [6].

Z. Kam and al. proposed to estimate the 3D refractive index variations by using Nomarski Differential Interference Contrast (DIC) microscopy and use this information to model PSFs that take into account the refractive index variations induced by the specimen [7].

Measuring the PSF is a method able to capture the maximum of the true system's aberrations; measurements have been done using sub-resolution beads either embedded in optical cement [2] or fixed to a tilted surface [3]. Some tries to identify and extract small structures in the imaged specimen that can be considered as PSF [8] [9].

These techniques offer a limited number of randomly positioned PSF, so an optical tweezers attached to an epi-fluorescence microscope has been proposed [10], this method allows the measurement of a depth variant PSF by axially shifting a small bead using the optical tweezers, according to the author this method is not suitable for very deep specimens where an alternative technique will have to be developed. However, the use of a high powered laser in order to stabilize the bead in place may induce local refractive index variations yielding some errors in the measured PSF.

In order to obtain more relatively accurate PSF from a limited number of known ones at a variable depth, we propose an interpolation technique that allows the estimation of PSF at various positions. This technique provides the necessary PSF for optimal deconvolution results in a non-invariance assumption using a minimal number of measured PSF.

A simple interpolation technique may not be accurate enough in order to reflect the true aberration changes of the PSF. The proposed method quantifies the variation of the PSF by decomposing the image into a set of descriptors representing the PSF properties using Zernike moments.

3.3. PSF REPRESENTATION WITH ZERNIKE MOMENTS

3.3.1. GENERAL MOMENT THEORY

Moments are scalar quantities used to characterize a function and to capture its significant features. A set of moments computed from a digital image, generally represents global characteristics of the image and provides a lot of information about different types of geometrical features of the image, for these reasons, image Moments are widely used in computer vision and robotics for object identification techniques.

From the mathematical point of view, moments are “projections” of a function onto a polynomial basis (similarly, Fourier Transform is a projection onto a basis of harmonic functions). An image can be considered as a two-dimensional continuous real function $f(x, y)$ defined over a 2D plane in a domain noted ζ , where the value denotes the pixel intensity at location (x, y) . A general definition of moment function Φ_{pq} of an image $f(x, y)$ where p and q are non-negative integers and $(p + q)$ is the order, can be written as:

$$\Phi_{pq} = \iint_{\zeta} \Psi_{pq}(x, y) f(x, y) dx dy, \quad p, q = 0, 1, 2, 3 \dots \quad (3.1)$$

The function $\Psi_{pq}(x, y)$ is continuous over the domain ζ and is known as the moment weighting kernel or the basis set. p and q usually denote the degrees of the coordinates x , y respectively, as defined inside the function Ψ and depending on the polynomial basis used, one can obtain various systems of moments such as geometrical moments .

The equation (3.1) may have different variations depending on the type of the basis set used. For example, when using polar coordinates (ρ, θ) as basis function, it is necessary to re-write (3.1) in terms of polar representation of the image’s coordinate space, e.g:

$$\Phi_{pq} = \iint_{\zeta} \Psi_{pq}(\theta) f(\rho, \theta) \rho^{p+q+1} d\rho d\theta \quad p, q = 0, 1, 2, 3 \dots \quad (3.2)$$

Furthermore, in the case of orthogonal basis functions, which are only valid inside a unit circle, one should scale the coordinate space ζ to the region $[-1, 1]$. While evaluating the moment function, the integrals are often replaced by a direct summation as a first approximation, with an appropriate scale factors for the area’s elements.

3.3.2. ZERNIKE MOMENTS DESCRIPTORS

Zernike polynomials [11] [12] are widely used as a basis function of image moments, which makes them excellent invariant descriptors of the image shape and offer a good reconstruction of the image. They have been proven to be superior to other moment functions [13] [14], such as geometric moments, in terms of feature representation capabilities and robustness in the presence of noise. Their orthogonal property helps in achieving a near zero value in terms of redundancy measure in a set of moment functions. Thus, moments of different orders correspond to independent characteristics of the image [15].

An accurate representation of a PSF can be achieved by Zernike Polynomials since they offer a compact representation where low-order coefficients represent typical aberrations of optical wave-fronts while noise is represented in higher order coefficients [16]

Zernike moments are based on a set of complete and orthogonal functions defined over polar coordinate space, inside a unit circle.

The two dimensional Zernike moment of order p and repetition q of a continuous function $f(\rho, \theta)$ is defined as:

$$A_{pq} = \frac{1+p}{\pi} \int_0^1 \int_{-\pi}^{\pi} f(\rho, \theta) [V_{pq}(\rho, \theta)] \rho b d \rho d \theta \quad (3.3)$$

Where

$$\begin{cases} p = 0, 1, 2, \dots, \infty \\ q \in Z \\ p - |q| \text{ is even, } |q| < p \end{cases}$$

Zernike polynomial $V_{pq}(\rho, \theta)$ is defined as:

$$V_{pq}(\rho, \theta) = R_{pq}(\rho) \exp(-iq\theta) \quad (3.4)$$

Where $R_{pq}(\rho)$ is the orthogonal radial polynomial, defined as:

$$R_{pq}(\rho) = \sum_{s=0}^{(p-|q|)/2} (-1)^s \frac{(p-s)!}{s! \left(\frac{p+|q|}{2} - s\right)! \left(\frac{p-|q|}{2} - s\right)!} \rho^{p-2s} \quad (3.5)$$

Since Zernike moments are defined in terms of polar coordinates (ρ, θ) with $\rho \leq 1$, their computation requires a linear transformation of the image coordinates to a suitable domain inside a unit circle [17]. As 2D PSF are considered as airy discs, the transformation $(0; N-1) \xrightarrow{\text{yields}} (-1; +1)$ is used as shown in Fig. 1 where $x = (i - i_c) / N$ and $y = (j - j_c) / N$ with i_c and j_c are the coordinates of the unit circle. Then $\rho = (x^2 + y^2)^{1/2}$ is the length of the vector from the origin to the mapped pixel (x, y) into the unit circle, $\theta = \tan^{-1}\left(\frac{y}{x}\right)$ is the angle between the vector and the x axis and $x^2 + y^2 \leq 1$.

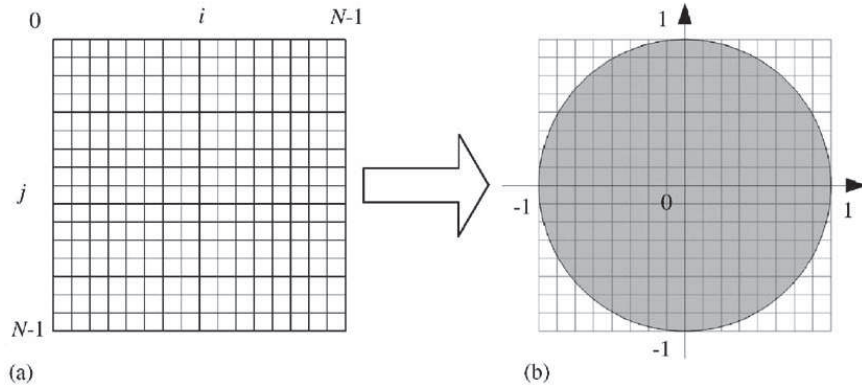


FIG. 1: THE MAPPING TRANSFORM BETWEEN CARTESIAN COORDINATE OF AN IMAGE TO POLAR COORDINATES INSIDE A UNIT CIRCLE [15].

The discrete approximation of Zernike moments is expressed as follow:

$$A_{pq} = \tau(N, p) \sum_{x=0}^{N-1} \sum_{y=0}^{N-1} f(\rho, \theta) V(\rho, \theta) \quad \{\rho \leq 1 \quad (3.6)$$

Where $\tau(D, p)$ is a normalization factor, defined by the number of pixels located in the unit circle by the mapping transform, which corresponds to the area π of a unit circle in the continuous domain D.

The image intensities can then be expressed using Zernike polynomials over the unit circle as:

$$f(\rho, \theta) = \sum_{p=0}^{\infty} \sum_{q=0}^p A_{pq} V_{pq}(\rho, \theta) \quad (3.7)$$

With Zernike moments A_{pq} calculated over the same unit circle.

However the reconstruction of an image using an infinite number of moments is computationally impossible, therefore this expansion is truncated to a finite order P_{\max} and considered as an optimum approximation to the original image function. The estimated reconstructed image \hat{f} is given as:

$$\hat{f}(\rho, \theta) = \sum_{p=0}^{P_{\max}} \sum_{q=0}^p A_{pq} V_{pq}(\rho, \theta) \quad (3.8)$$

This estimate can be easily computed using expansion with real-valued functions as given below:

$$\hat{f}(\rho, \theta) = \sum_{p=0}^{P_{\max}} \sum_{q>0}^p (C_{pq} \cos(q\theta) + S_{pq} \sin(q\theta)) R_{pq}(\rho) + \frac{C_{p0}}{2} R_{p0}(\rho) \quad (3.9)$$

Where C_{pq} and S_{pq} are the real and imaginary parts of A_{pq} with

$$C_{pq} = 2 \operatorname{Re}(A_{pq}) = \frac{2p+2}{\pi} \int_0^1 \int_{-\pi}^{\pi} f(\rho, \theta) R_{pq}(\rho) \cos(q\theta) \rho d\rho d\theta \quad (3.10)$$

$$S_{pq} = 2 \operatorname{Im}(A_{pq}) = \frac{-2p-2}{\pi} \int_0^1 \int_{-\pi}^{\pi} f(\rho, \theta) R_{pq}(\rho) \sin(q\theta) \rho d\rho d\theta \quad (3.11)$$

3.3.3. DESCRIBING PSF WITH ZERNIKE MOMENTS

Because the image is formed by real numbers, one can safely assume that the imaginary part of the constructed value is always zero. If one actually calculates the imaginary part of the recovered function, the values may be different than zero due to rounding errors. The absolute sum of the recovered function's imaginary part can be a good indicator of the rounding error's cumulative magnitude [18]. Thus only the real part of Zernike moments needs to be considered (the part with $\cos(q\theta)$ term), so one can write:

$$A_{pq} = \tau(D, p) \sum_x \sum_y R_{pq}(\rho) \cos(q\theta) f(\rho, \theta) \quad (3.12)$$

And

$$\hat{f}(\rho, \theta) = \sum_{p=1}^{P_{\max}} \sum_{q>1}^p 2A_{pq} R_{pq}(\rho) + \frac{C_{p0}}{2} R_{p0}(\rho) \quad (3.13)$$

Where $\rho = (x^2 + y^2)^{1/2} \leq 1$ and $\theta = \tan^{-1}(y/x)$.

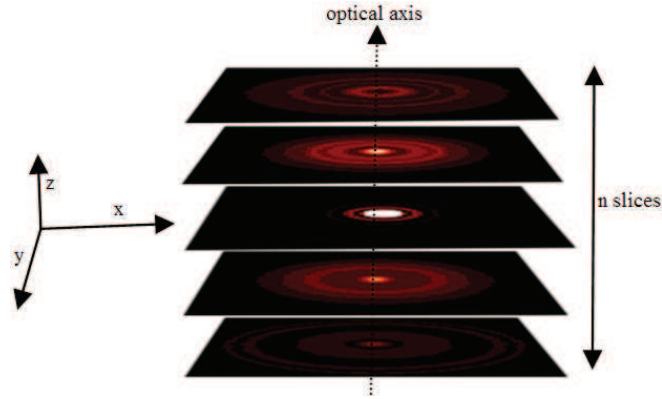


FIG. 2: 3D PSF REPRESENTATION – ALL SLICES ARE CENTERED BY THE SAME WAY IN THE UNIT CIRCLE (THE CENTRE OF MASS BEING CALCULATED USING THE AIRY DISK)

In our work, 3D PSF are considered as a stack of 2D airy patterns (Fig. 2) and the decomposition of a 3D PSF using Zernike moments is reduced to the decomposition of each slide (centered on the optical axis of the 3D PSF) then the reconstruction is done by reconstructing each slide apart. For a given order p and repetition q the Zernike moment of order “ p ” and repetition “ q ” on slide n can be written as:

$$A_{pq}^n = \sum \sum \tau_p f^n(\rho, \theta) R(\rho) \cos(q\theta) \quad (3.14)$$

The term $R(\rho)$ can be calculated once and used for all planes of the PSF (or any PSF of same dimensions).

Fig. 3 represents the first 5 orders and positive repetitions (0 to 4).

Each PSF plane is then represented by a set of Zernike moments with P_{\max} as the maximal optimal order, where each moment represents the participation of an aberration. An “n” plane 3D PSF at depth k can be represented using Zernike moments as follow:

$$Z_k = [B_{00}^k \quad \dots \quad B_{pq}^k] = \begin{pmatrix} A_{00}^1 & \dots & A_{pq}^1 \\ \vdots & \ddots & \vdots \\ A_{00}^n & \dots & A_{pq}^n \end{pmatrix} \quad (3.15)$$

For the rest of this manuscript we refer to this representation Z_k as pseudo-3D Zernike moments of the PSF at depth k.

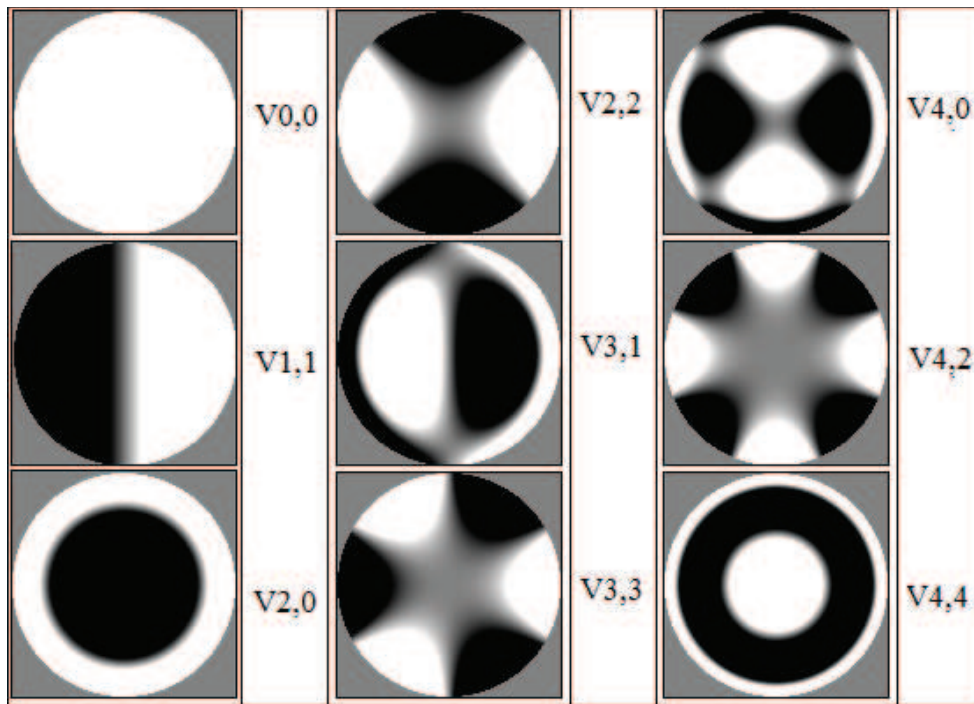


FIG. 3: ZERNIKE POLYNOMIALS IN THE UNIT CIRCLE FOR VARIOUS ORDER AND REPETITION (V0,0 = PISTON; V1,1 = TILT IN X; V2,0 = FIELD CURVATURE, DEFOCUS; V2,2 = ASTIGMATISM AT 0° OR 90°; V3,1 = COMA ALONG X AXIS; V3,3 = TREFOIL; V4,0 = SPHERICAL ABERRATION; V4,2 = SECONDARY ASTIGMATISM; V4,4 = QUADRAFOIL).

3.3.3.1. RADIALLY SYMMETRIC PSF

The entire set of odd orders of Zernike moments yields a zero value when they are applied to images which are symmetrical along the x- and y-axes. Since a symmetrical image has pairs of pixels that are equidistant (in opposite directions) from its centroid, the sum of an odd-order moment calculation produces a value of zero.

This case applies when using a radially symmetric PSF and thereby this property can be used to reduce the computational load.

In the case of measured radially symmetric PSF the noise disturbs the symmetry propriety. Only in such case, forcing these orders to the zero value yields a better symmetry in the construction of the interpolated PSF.

3.4. ANALYSIS OF MOMENTS VARIATIONS

To study the variation of Zernike moments along the depth of the PSF, one must know the intensity distribution of K PSF on different depth positions, of the same dimensions and well centered. These PSF are described using pseudo-3D Zernike moments and the 3D matrix $MZ(a, p, k)$ is formed, where each plane holds $Z_k \{1 \leq k \leq K\}$.

In this matrix, each plane represents a PSF at depth k where each line is the slice p Zernike moments representation a .

To get a specific pseudo-3D moment variation, V_{an} is constructed:

$$V_{an} = MZ(a, n, i) \{1 \leq i \leq k\} \quad (3.16)$$

The moment's index a is related to moment order and repetition "p, q" by the following equation:

$$a = \begin{cases} \left(\frac{p-1}{2} + 1\right)\left(\frac{p-1}{2} + 2\right) + \frac{q}{2} + 1 & \text{if } p \text{ is even} \\ \left(\frac{p-2}{2} + 1\right)\left(\frac{p-2}{2} + 2\right) + \frac{p-1}{2} + \frac{q}{2} + 2 & \text{if } p \text{ is odd} \end{cases} \quad (3.17)$$

This will permit to analyze the variation of each moment over a defined plane. The Fig. 4 shows the moment variation for a simulated set of PSF over two different planes. These curves show a continuous variation for an $A_{p,q}$ along the depth, then a polynomial fitting can be applied.

Chapter 3

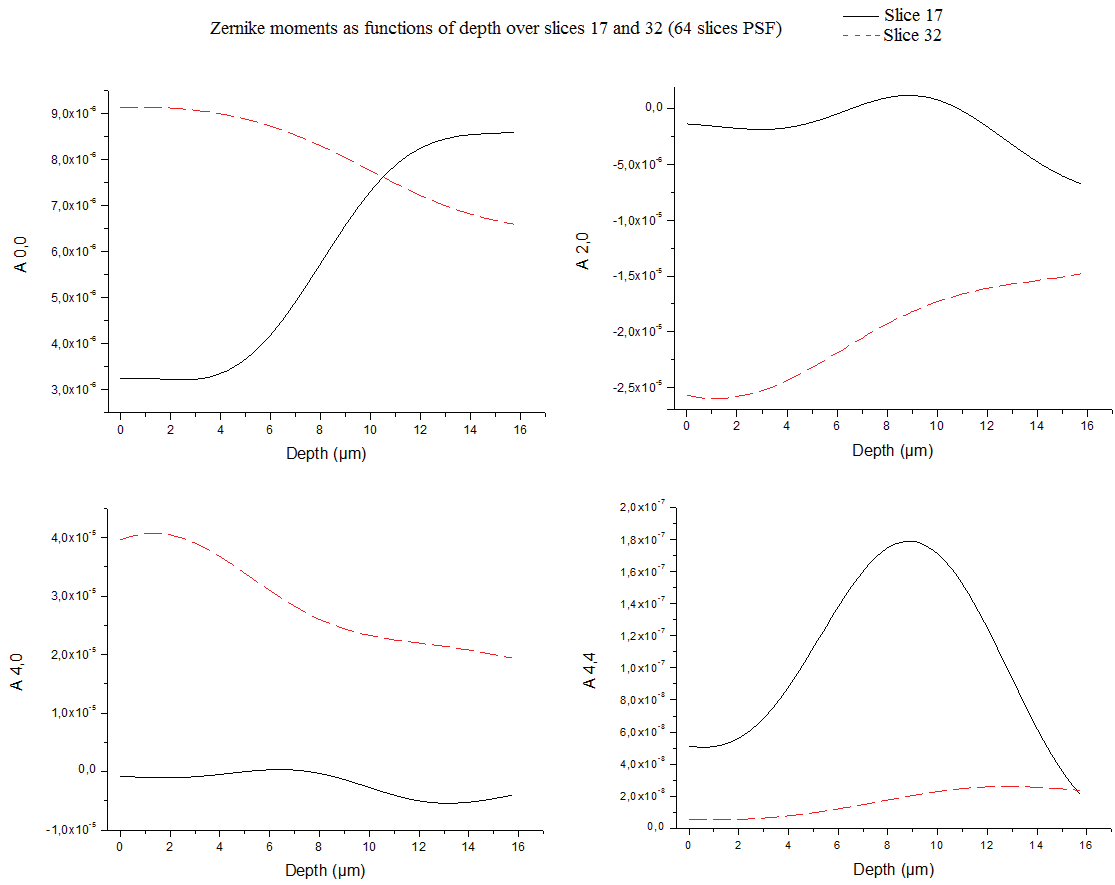


FIG. 4: FOUR ZERNIKE MOMENTS VARIATIONS OVER THE 17TH PLANE AND THE 32, ALONG THE DEPTH ($0\mu\text{m} - 15.75\mu\text{m}$). THE VARIATIONS REPRESENT RESPECTIVELY THE PARTICIPATION OF “PISTON”, “FIELD CURVATURE”, “SPHERICAL ABERRATION” AND “QUADRAFOIL”.

3.5. POLYNOMIAL FITTING AND INTERPOLATION

The changes in the pseudo-3D Zernike moments can be estimated using polynomial fittings.

The MZ 3D matrix is transformed to 2D matrix holding in each line the variation functions of each Zernike moment in the n th plane:

$$MZ(a, p, k) \xrightarrow{\text{yields}} VZ(a, p) = \begin{pmatrix} p_{00} & \cdots & p_{a0} \\ \vdots & \ddots & \vdots \\ p_{0n} & \cdots & p_{an} \end{pmatrix} \quad (3.18)$$

Where p_{an} the polynomial function representing the variation through depth of the moment of index a in the plane n .

Having polynomials description for each moment variation, it becomes straight forward to interpolate the whole set of pseudo-3D moments values at a certain depth and construct an estimate of the PSF using (3.13).

The PSF interpolation process can be described as following:

- K PSF at various depths are described using pseudo-3D Zernike moments and $MZ(a, p, k)$ is formed.
- MZ is transformed to the polynomial functions matrix $VZ(a, p)$ using polynomial fitting.
- For each needed depth value the entire set of 3D-pseudo Zernike values are estimated using VZ functions.
- The estimated PSF are constructed using equation (3.13).

3.6. DISCUSSION AND RESULTS

The tests are carried over simulated PSF in a volume of 64x64x64 voxels as references, computed using Török and Varga vectorial model modified by Olivier Haeberlé. Gaussian noise is added at different SNRs, from 30dB to 10dB, to demonstrate the robustness in measured PSF conditions. The Gaussian noise is the assumed noise type found in the wide field 3D fluorescence images (under sufficient light conditions) with an acceptable SNR around 20dB.

3.6.1. PSEUDO-3D RECONSTRUCTION

To test the reconstruction accuracies of a 3D PSF using the pseudo-3D Zernike moments, 2 PSF at depths 0 μ m and 10 μ m are used. Three reconstructions with a maximum Zernike order of $P_{\max} = 45$ are done in noise free conditions and with SNR of 20db and 10db. The error criterion used is the 3D correlation coefficient according to formula:

$$r_p = \frac{\sum_{i=0}^{i<N} (X_i - \bar{X})(Y_i - \bar{Y})}{\sqrt{\sum_{i=0}^{i<N} (X_i - \bar{X})^2 \sum_{i=0}^{i<N} (Y_i - \bar{Y})^2}} \quad (3.19)$$

	0.5 μ m (noise free)		0.5 μ m (SNR = 20db)		0.5 μ m (SNR = 10db)	
	original	Reconstructed	original	reconstructed	original	reconstructed
Corr. Coef (the calculated PSF is the ref.)	1	0.9907	0.7004	0.847	0.309	0.563

FIG. 5: RECONSTRUCTION OF A PSF AT 0 μ m OF DEPTH USING PSEUDO-3D ZERNIKE MOMENTS UP TO ORDER 45. WITH NOISE FREE IMAGE, SIGNAL TO NOISE RATIO OF 20DB AND 10DB RESPECTIVELY FROM LEFT TO RIGHT. THE CONTRAST WAS DELIBERATELY MODIFIED IN ORDER TO HIGHLIGHT LOW LEVEL STRUCTURES.

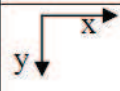


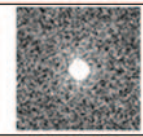
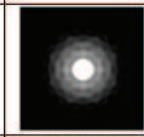
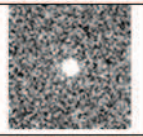
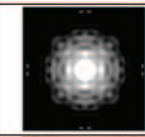
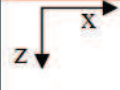


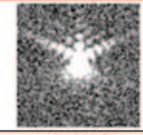
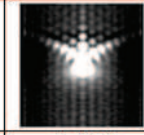
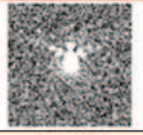
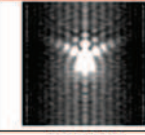
	0.5 μm (noise free)		0.5 μm (SNR = 20db)		0.5 μm (SNR = 10db)	
	original	Reconstructed	original		original	Reconstructed
						
						
Corr. coef (calculated PSF as ref.)	1	0.987	0.822	0.946	0.422	0.8005

FIG. 6: RECONSTRUCTION OF A PSF AT 10 μm OF DEPTH USING PSEUDO-3D ZERNIKE MOMENTS UP TO ORDER 45. WITH NOISE FREE IMAGE, SIGNAL TO NOISE RATIO OF 20DB AND 10DB RESPECTIVELY FROM LEFT TO RIGHT. THE CONTRAST WAS DELIBERATELY MODIFIED IN ORDER TO HIGHLIGHT LOW LEVEL STRUCTURES.

As seen in Fig. 5 and Fig. 6, the reconstructions have a coefficient of correlation up to 0.99, in the presence of noise the correlation coefficient relative to the calculated noiseless image rises from 0.7 in the case of the noisy original image with SNR of 20db at 0.5 μm of depth to 0.84 in the case of the constructed one, this coefficient rises from 0.822 to 0.946 for PSF at 10 μm of depth. In an ideal case, the correlation coefficient cannot be equal to 1, due to the limited number of Zernike orders used in the construction, in other hand, in presence of noise, the order number limitation induces a filtering effect, while conserving the main features of the PSF.

3.6.2. FITTING ORDER

The algorithm uses the polynomial fitting for interpolation, so it is quite obvious that one of the basic condition is to have points well spread (ideally uniformly scattered) over the interpolation area.

In order to study the effect of fitting order on the construction efficiency, a set of 9 PSF at positions 0-2-4-6-8-10-12-14-15.75 μm are used to interpolate 3 PSF at positions 1 μm , 7 μm and 15 μm respectively. While changing the polynomial fitting order between 1 and 8 ((psf number) - 1). The correlation coefficient is calculated relatively to the calculated PSF at these same positions and traced (Fig.8). This test is done using noisy PSF with SNR of 30db, 20db and 10db.

Chapter 3

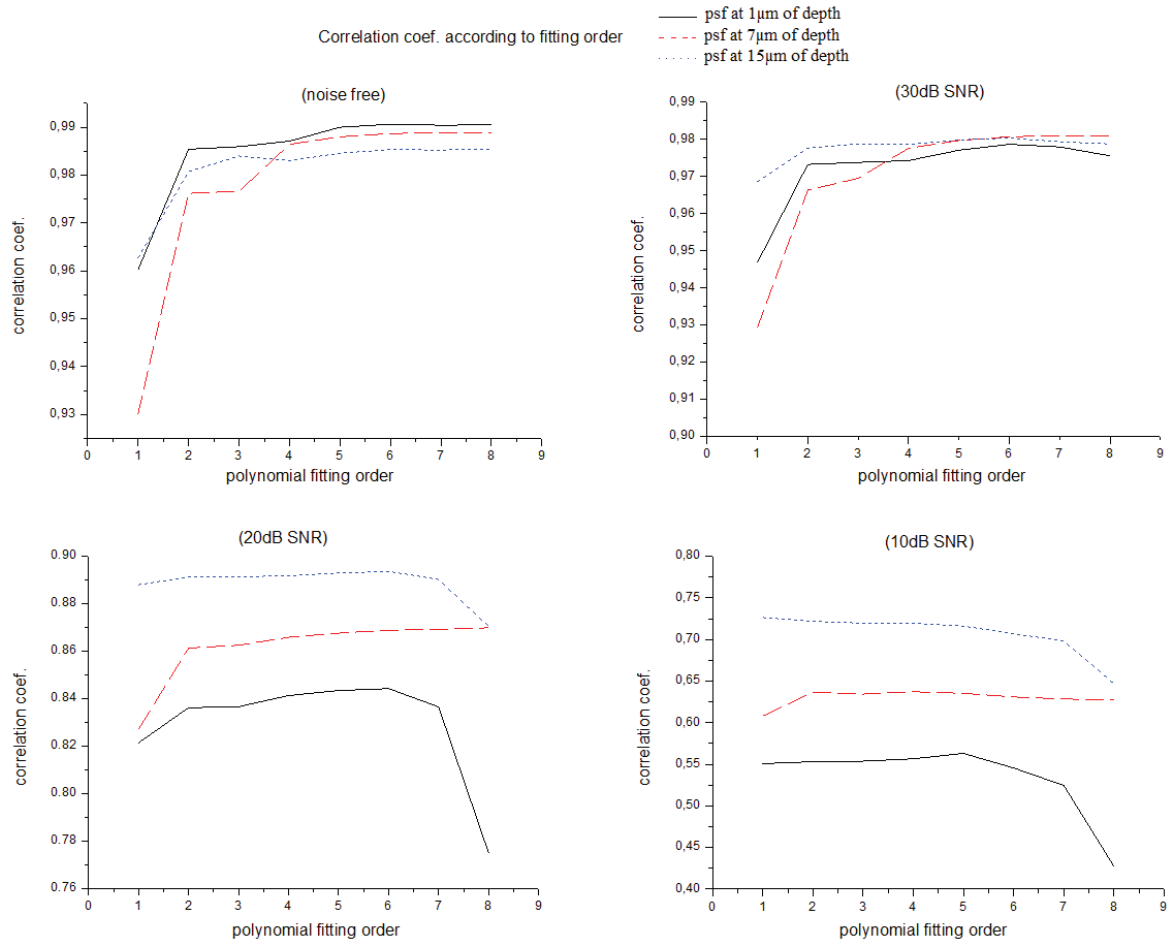


FIG. 7: CORRELATION COEFFICIENT (RELATIVE TO CALCULATED NOISE- FREE PSF) AS FUNCTION OF POLYNOMIAL FITTING ORDER USED (1-8). PSF ARE AT $1\mu\text{M}$, $7\mu\text{M}$ AND $15\mu\text{M}$ OF DEPTH. TOP LEFT: NOISE FREE PSF – TOP RIGHT: 30dB SNR – BOTTOM LEFT: 20dB SNR – BOTTOM RIGHT: 10dB SNR.

As can be seen in Fig. 7 the correlation coefficient reaches its maximum around order 6 in the case of noise free images and becomes stable while the order gets high. When images are corrupted with noise, the correlation coefficient starts to decrease after the order 5, especially for deep PSF positions. Actually when the image is corrupted with noise, the Zernike moments variations present local irregularities with amplitude proportional to the SNR. In such cases, polynomial of higher order tries to follow the irregularities, but such polynomials, while fitting to the irregularity, deviate widely at other regions introducing significant errors into the interpolation. As result the preferred fitting order is located between 4 and 6 depending on noise SNR and the number of known PSF. as: $ord \leq K - 1$ where “ord” is the fitting order and “K” is the number of known PSF used.

3.6.3. INTERPOLATION

To simulate a PSF interpolation case, 6 calculated PSF are used as known PSF at locations 0-3-6-9-12-15.75 μm . PSF are interpolated at positions extending from 0 μm to 15.75 μm with steps of 0.25 μm (Z axes resolution of our microscope), these PSF are compared with calculated noise free PSF using the correlation coefficient as resemblance criteria.

The test is carried with noise free PSF and with PSF degraded with Gaussian noise of 30db, 20db and 10db SNR.

The polynomial fitting order used is 5 and Zernike maximal decomposition order is 45.

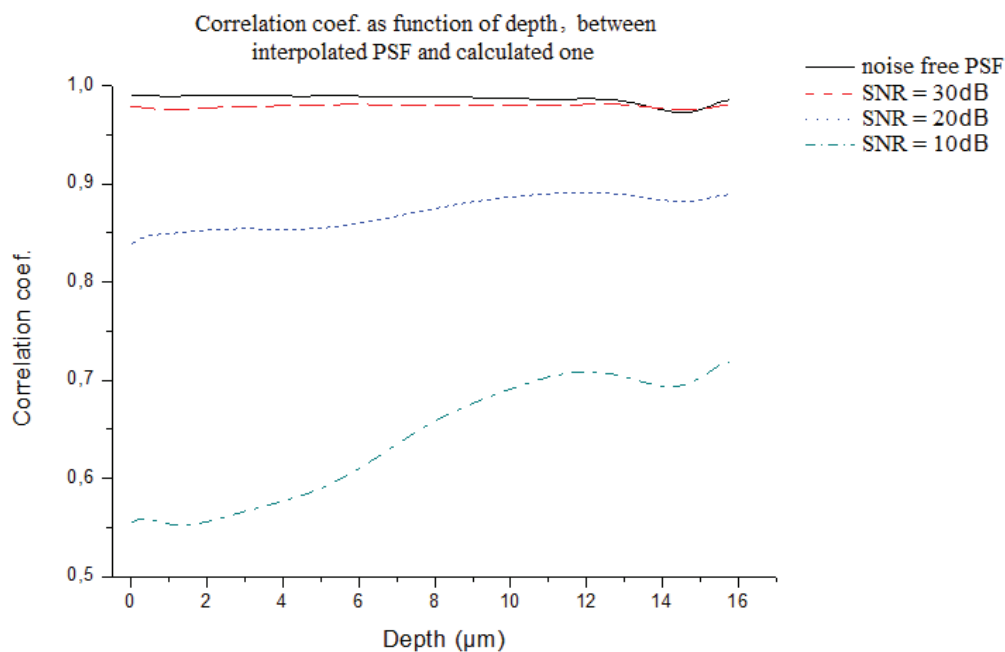


FIG. 8: CORRELATION COEFFICIENT AS A FUNCTION OF PSF DEPTH, BETWEEN INTERPOLATED PSF (USING 6 PSF (NOISE FREE AND SNR OF 30, 20 AND 10dB) AT 0, 3, 6, 9, 12 AND 15.75 μm) AND CALCULATED ONE.

As can be seen in Fig. 8, the interpolated PSF reach a correlation coefficient as 0.98 with SNR of 30db, drops to a mean of 0.87 at 20db and 0.65 at 10db SNR which is considered as fairly acceptable.

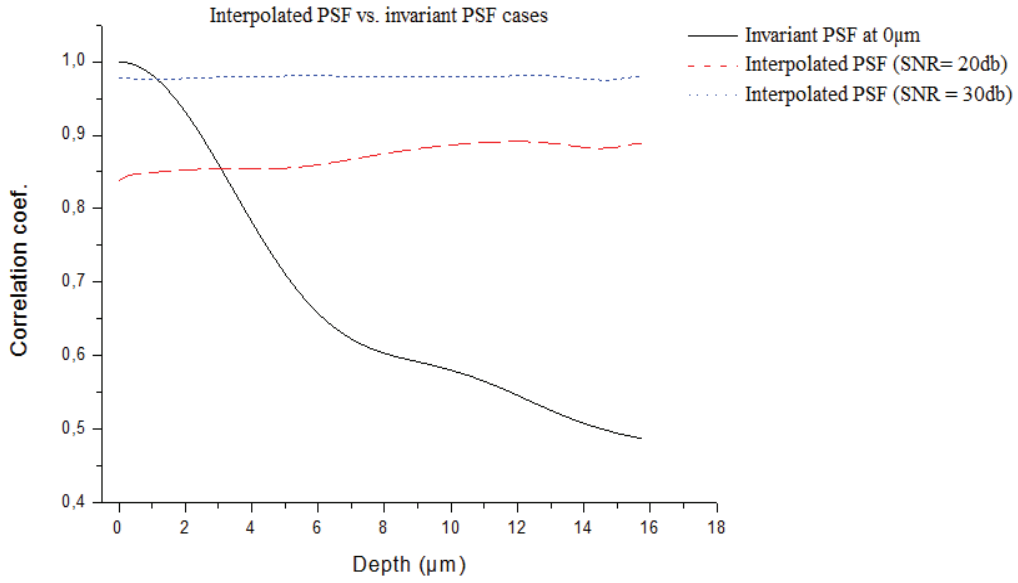


FIG. 9: CORRELATION COEFFICIENT AS A FUNCTION OF PSF DEPTH BETWEEN USED PSF AND CALCULATED ONE. THE CASE OF INTERPOLATED PSF (USING 6 WITH SNR OF 20dB (DASHED LINE) AND 30dB (DOTTED LINE) AT 0, 3, 6, 9, 12 AND 15.75μm) AND INVARIANT PSF AT 0μm (SOLID LINE).

To show the gain obtained using PSF interpolation we show in Fig. 9 the similitude variations between the used PSF and the calculated one along the depth, in the case of interpolated PSF and when using an invariant PSF calculated at 0μm.

A qualitative representation of interpolated PSF at 7μm can be seen at Fig. 10. The quality of a deconvolution using Zernike interpolated PSF is presented in the next chapter.

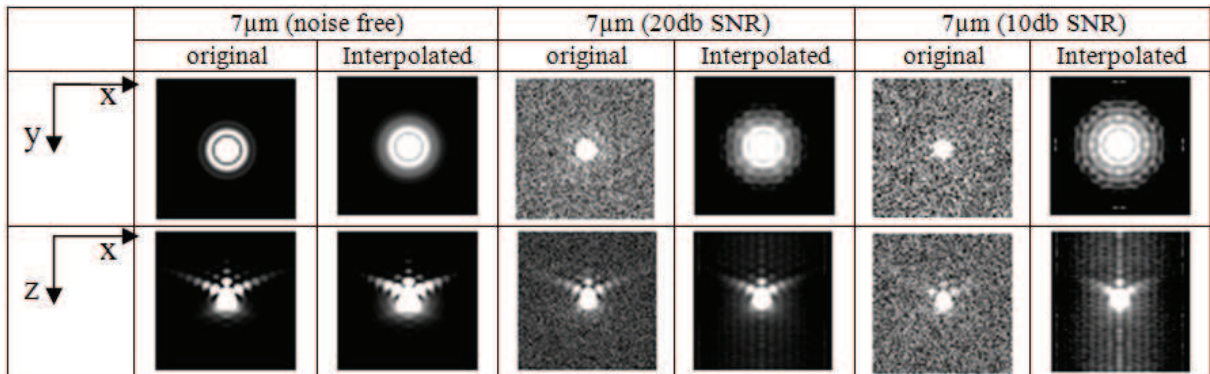


FIG. 10: INTERPOLATED PSF AT 7μm USING 6 KNOWN PSF, FROM LEFT TO RIGHT: NOISE FREE, 20dB AND 30dB GAUSSIAN NOISE (THE ORIGINALS ARE GIVEN AS COMPARISON REFERENCES).

3.7. ZERNIKE INTERPOLATION FOR OTHER OPTICAL PARAMETERS:

Zernike interpolation can be applied to study and interpolate PSF when any single optical parameter changes. One parameter that can change significantly and have a large impact over the PSF shape, other than the depth, is the immersion refractive index.

Objective numerical aperture can be increased by designing the objective to be use with an immersion medium with a refractive index similar to that of the glass coverslip. Image degradation due to thickness variations of the cover glass are practically eliminated, as the rays of high angle are no longer refracted and they are grasped by the objective (Fig. 11).

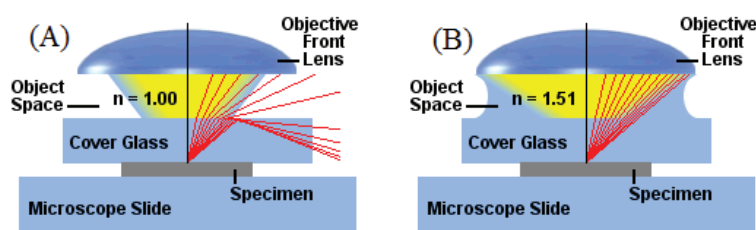


FIG. 11: THE CHANGES IN THE REFRACTIVE INDEX OF THE IMAGING MEDIUM CAN AFFECT HOW LIGHT RAYS ARE CAPTURED BY THE OBJECTIVE (ARBITRARILY FIXED ANGULAR APERTURE OF 65 DEGREES). A) AIR OBJECTIVE. B) OIL IMMERSION OBJECTIVE. (USED FROM WWW.MICROSCOPYU.COM - NIKON).

Temperature is a factor often overlooked as it applies to immersion oil. Liquids and most solids change index in an inverse ratio to the change in temperature (the RI goes down as temperature goes up). The temperature for which the oil is adjusted should be stated. We shall consider oil with a refractive index at 23 °c of 1.515 +/- .0005 (ISO). Meaning that a difference of 1°C in room temperature from the stated value causes a change in index of the oil of approximately 0.0005, summer weather or overheated rooms can affect the index match considerably. It must be remembered that both the glass and the oil change index with temperature. However, the change in solids is generally so insignificant that it can be ignored.

The effect of a change in temperature of 10°C on a PSF at 1µm of depth with an oil immersed objective having a numerical aperture of 1.4 and emission wavelength of 630nm can be noticed in Fig. 12.

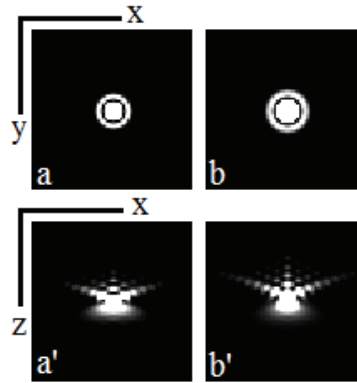


FIG. 12: EFFECT OF TEMPERATURE VARIATION OF 10°C OVER A PSF AT 1 μ M (NA: 1.4 – COVERSGLIP RI: 1.515 - OIL RI: 1.515 AT 23°C +/- .0005). a-a') T=23°C – ORI=1.515. b-b') T=33°C – ORI=1.510.

In this section we apply Zernike interpolation over PSF when only the refractive index changes with the ambient temperature. For validation purposes, 5 PSF are calculated at 1 μ m of depth under the coverslip using an objective with a numerical aperture of 1.4, emission wavelength of 630nm and a coverslip with a refractive index of 1.515 with oil refractive index calculated at 10, 15, 23, 28 et 33°C, considering an immersion oil having a refractive index at 23°C of 1.515 +/- 0.0005.

PSF at any temperature in the range of 10°C up to 33°C can then be interpolated (a realistic range of environment temperature). Fig. 13 shows a visual comparison between interpolated PSF at 18, 25 and 30°C and the theoretical calculated ones. The 3D correlation coefficient is 0.98 in the three cases.

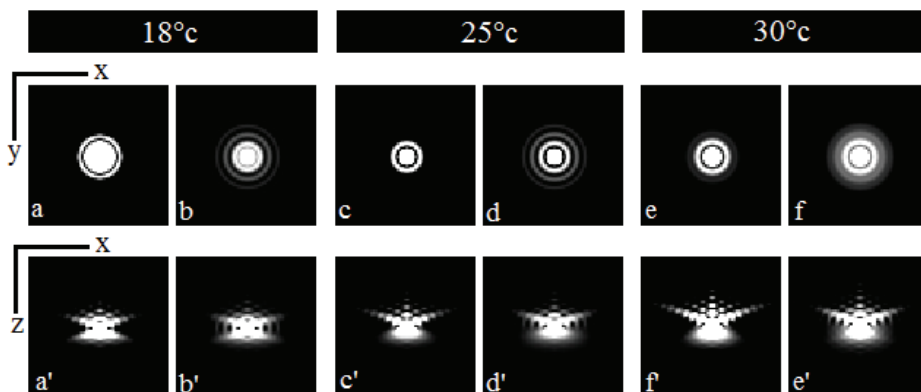


FIG. 13: A-A') THEORETICAL PSF AT 18°C. B-B')INTERPOLATED PSF AT 18°C. C-C')THEORETICAL PSF AT 25°C. D-D')INTERPOLATED PSF AT 25°C. E-E') THEORETICAL PSF AT 30°C. F-F')INTERPOLATED PSF AT 30°C.

A high correlation coefficient and a successful interpolation of the main major features of the PSF are achieved. One can notice ring amplification in the Zernike result. These rings are present at a lower level in the original PSF; however the PSF shape is well reconstructed.

3.8. CONCLUSION AND PERSPECTIVE

An effective interpolation technique based on Zernike moments has been developed. This technique allows studying the variation of PSF along the depth and interpolating PSF needed at various depths, using only a restricted number of known ones. It may also be used to study other parameter variation, such as emission wavelength or oil refractive index.

The process is implemented as an ImageJ plugin, using java language. Running on a 2.4 GHz PC with 4 GB of RAM and 64bit JVM the processing time for the interpolation test above was around 2 minutes.

The interpolation process has been implemented using a basic algorithm for computing Zernike polynomials, limiting the number of orders that can be used to 45 due to the factorial computing limits. Thereby the size of the images cannot exceed (64x64x64) voxels, larger images need higher orders to be better described and reconstruct, this can be done using advanced Zernike computation techniques [19] [20] [21] that will also reduce the computational time.

In this chapter, a PSF interpolation method based on Zernike moments and polynomial fitting was presented and tested on synthetic data with and without noise. In chapter 4, the interpolation technique will be tested with measured PSF with 100nm fluo-beads imbedded in polymers. And the interpolated PSF will be used in a non-invariant deconvolution using “EMMA” presented in chapter 2 (Evolutive Merging Masks Algorithm).

3.9. REFERENCES:

1. S. Frisken Gibson et F. Lanni, "Experimental test of an analytical model of aberration in an oil-immersion objective lens used in three-dimensional light microscopy," *J. Opt. Soc. Am. A* **9**, 154-166 (1992).
2. A. Chomik, A. Dieterlen, C. Xu, O. Haeberle, J. J. Meyer, et S. Jacquy, "Quantification in optical sectioning microscopy: a comparison of some deconvolution algorithms in view of 3D image segmentation," *Journal of Optics* **28**, 225-233 (1997).
3. J. G. McNally, C. Preza, J. Conchello, et L. J. Thomas, "Artifacts in computational optical-sectioning microscopy," *J. Opt. Soc. Am. A* **11**, 1056-1067 (1994).
4. A. Diaspro, F. Federici, et M. Robello, "Influence of refractive-index mismatch in high-resolution three-dimensional confocal microscopy," *Appl Opt* **41**, 685-690 (2002).
5. O. Haeberlé, F. Bicha, C. Simler, A. Dieterlen, C. Xu, B. Colicchio, S. Jacquy, et M. Gramain, "Identification of acquisition parameters from the point spread function of a fluorescence microscope," *Optics Communications* **196**, 109-117 (2001).
6. F. Aguet, D. Van de ville, et M. Unser, "An accurate PSF model with few parameters for axially shift-variant deconvolution," *Biomedical Imaging: From Nano to Macro* **5th IEEE**, 157 - 160 (2008).
7. Z. Kam, B. Hanser, M. G. L. Gustafsson, D. A. Agard, et J. W. Sedat, "Computational adaptive optics for live three-dimensional biological imaging," *Proc Natl Acad Sci U S A* **98**, 3790-3795 (2001).
8. J. B. de Monvel, E. Scarfone, S. Le Calvez, et M. Ulfendahl, "Image-Adaptive Deconvolution for Three-Dimensional Deep Biological Imaging," *Biophysical Journal* **85**, 3991-4001 (2003).
9. M. Von Tiedemann, A. Fridberger, M. Ulfendahl, I. Tomo, J. Boutet de Monvel, et J. B. De Monvel, "Image adaptive point-spread function estimation and deconvolution for in vivo confocal microscopy," *Microsc. Res. Tech* **69**, 10-20 (2006).
10. J. W. Shaevitz et D. A. Fletcher, "Enhanced three-dimensional deconvolution microscopy using a measured depth-varying point-spread function," *J. Opt. Soc. Am. A* **24**, 2622-2627 (2007).
11. F. Zernike, "Beugungstheorie des Schneidensverfahrens und seiner verbesserten Form, der Phasenkontrastmethode," *Physica* **1**, 689-704 (1934).
12. F. Zernike et H. Brinkman, "Hypersphärische Funktionen und die in sphärischen Bereichen orthogonalen Polynome," *Proc. K. Akad Wetensch* **38**, 161-170 (1935).
13. S. Liao et M. Pawlak, "Image analysis with Zernike moment descriptors," (2010).
14. C. Chong, P. Raveendran, et R. Mukundan, "Translation invariants of Zernike moments," *Pattern Recognition* **36**, 1765-1773 (2003).
15. A. De Meyer, "Contribution à l'amélioration des outils de restauration d'image et de caractérisation de l'instrument en microscopie 3D par Fluorescence," (2008).
16. N. Becherer, H. Jodicke, G. Schlosser, J. Hesser, F. Zeilfelder, et R. Manner, "On soft clipping of Zernike moments for deblurring and enhancement of optical point spread functions," dans C. A. Bouman, E. L. Miller, et I. Pollak, éd. (SPIE, 2006), Vol. 6065, p. 60650C-11.
17. M. R. Teague, "Image analysis via the general theory of moments*," *J. Opt. Soc. Am.* **70**, 920-930 (1980).
18. "Pseudo-Zernike Moments for Feature Extraction and Chinese Character Recognition," <http://www.scribd.com/doc/18993461/PseudoZernike-Moments-for-Feature-Extraction-and-Chinese-Character-Recognition>.
19. A. Mohammed et J. Yang, "Practical fast computation of Zernike moments," *Journal of Computer Science and Technology* **17**, 181-188 (2002).

Chapter 3

20. S. Hwang et W. Kim, "A novel approach to the fast computation of Zernike moments," *Pattern Recognition* **39**, 2065-2076 (2006).
21. J. Gu, H. Z. Shu, C. Toumoulin, et L. M. Luo, "A novel algorithm for fast computation of Zernike moments," *Pattern Recognition* **35**, 2905-2911 (2002).

4. EMMA-ZERNIKE COMBINATION (SIMULATION AND PRACTICAL APPLICATION)

AS FAR AS THE LAWS OF MATHEMATICS REFER TO REALITY,
THEY ARE NOT CERTAIN, AND AS FAR AS THEY ARE
CERTAIN, THEY DO NOT REFER TO REALITY.
ALBERT EINSTEIN

4.1. INTRODUCTION

EMMA offers a simple yet efficient solution for depth variant PSF deconvolution, the results quality depends on the number of known PSF used, their quality and their spreading along the object's depth. It is not always possible to acquire enough PSF that satisfy these requirements, in such cases, Zernike interpolation become a complementary solution to have satisfactory results.

In this section the entire solution, combining EMMA and Zernike interpolation, is evaluated on simulated data using a restrained PSF number with a low SNR, and measured data.

The specimen used contains 100nm fluorescent beads, PSF at various depths are acquired by imaging isolated beads in the volume and cells phantom like objects represented by aggregations of these beads, can be extracted. The acquired PSF set allows to verify Zernike interpolation results when applied on measured data and to use them for an EMMA depth variant deconvolution.

4.2. SIMULATION

The simulation is based on the same synthetic data used in the chapter concerning EMMA:

4 spherical beads having a diameter of $2.25\mu\text{m}$ spaced by $5\mu\text{m}$ along the optical axis, and the center of the first bead is places at $5.25\mu\text{m}$ of depth; a rectangular parallelepiped placed along the Z axis having $20.75\mu\text{m}$ of depth and $2.25\mu\text{m}$ as square side in x and y. Both images have been blurred with 128 PSF of $128 \times 128 \times 128$ using spatial depth variant convolution (see chapter 2) then polluted with a Gaussian noise with a 30dB SNR.

The restoration is performed using initially 5 calculated PSF ($64 \times 64 \times 64$ voxels) having 20dB SNR with Gaussian noise. It worth noting that 5 PSF represent a small number of known PSF relatively to a depth of $31.75 \mu\text{m}$ (128 planes), two of them are positioned at $0 \mu\text{m}$ (under coverslip) and $31.75 \mu\text{m}$ (on the slide) as these two positions are the easiest to measure with sub-resolution beads glued on the cover-slip and the slide respectively, the remaining three beads will be at $10 \mu\text{m}$, $18 \mu\text{m}$ and $25 \mu\text{m}$ (randomly chosen).

The small size of the used PSF is forced by the current implementation of Zernike interpolation algorithm where we can only calculate moments up to order 45, which does not guarantee a good restoration for larger images. A better implementation that can handle larger images is discussed in our perspectives.

Zernike interpolation will be applied over the 5 PSF to obtain 64 PSF (Fig. 6), each separated by $0.5 \mu\text{m}$ from its previous one starting at $0 \mu\text{m}$ (this will reduce by half the computational time needed when using full PSF set without a significant loss in result's quality). EMMA will be then applied combined with Lucy-Richardson algorithm. The results are compared with an EMMA deconvolution without a prior use of Zernike interpolation and with a depth invariant Lucy-Richardson deconvolution.

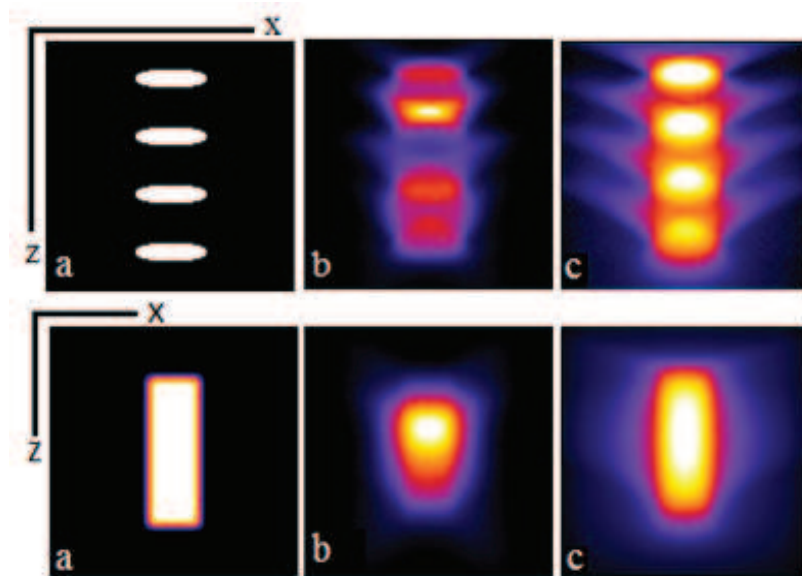


FIG. 1: DECONVOLUTION WITH A NON-INVARIANT ASSUMPTION USING LUCY-RICHARDSON ALGORITHM (100 ITERATION) – A) ORIGINAL DATA, B) RESTORED IMAGES, C) ACQUIRED IMAGES SIMULATION.

Fig. 1 shows a restoration attempt using Lucy-Richardson algorithm with depth invariant assumption, the PSF used is at $0 \mu\text{m}$ of depth calculated using Torök-Haeberlé algorithm and having a 20dB SNR with Gaussian noise (see Fig. 2).

Chapter 4

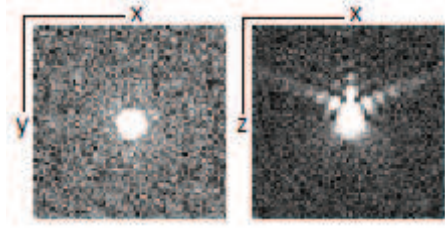


FIG. 2: CALCULATED PSF AT 5 μ m WITH 20DB SNR (CENTRAL PLANES).

One can notice that the beads are poorly separated and the wrong restoration of their depths. The parallelepiped form is not restored and one can notice an intensity shift toward the higher planes.

Fig. 3 represents two normalized intensity profiles comparing the deconvolution results with the original objects; the profiles were traced along the optical axis passing by the center of the object(s).

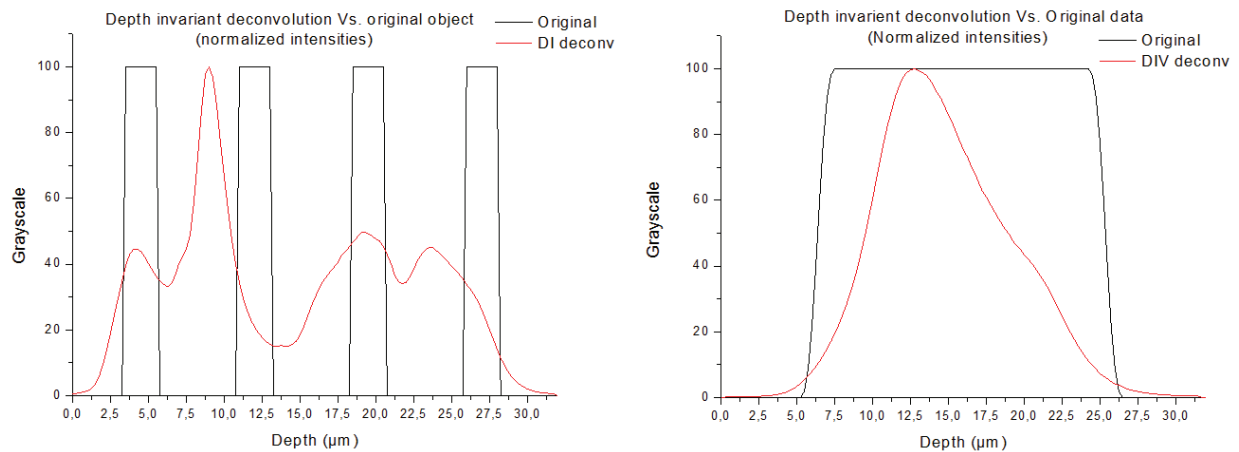


FIG. 3: NORMALIZED INTENSITIES PROFILES OF ORIGINAL OBJECT VS. DEPTH INVARIANT DECONVOLUTION RESULT (USING PSF AT 0 μ m DEPTH WITH 20dB SNR).

The 5 PSF are used to perform a deconvolution with EMMA associated to Lucy-Richardson algorithm, the results are shown in Fig. 4. And normalized intensities profiles comparing the deconvolution results with the original objects are shown at Fig. 5.

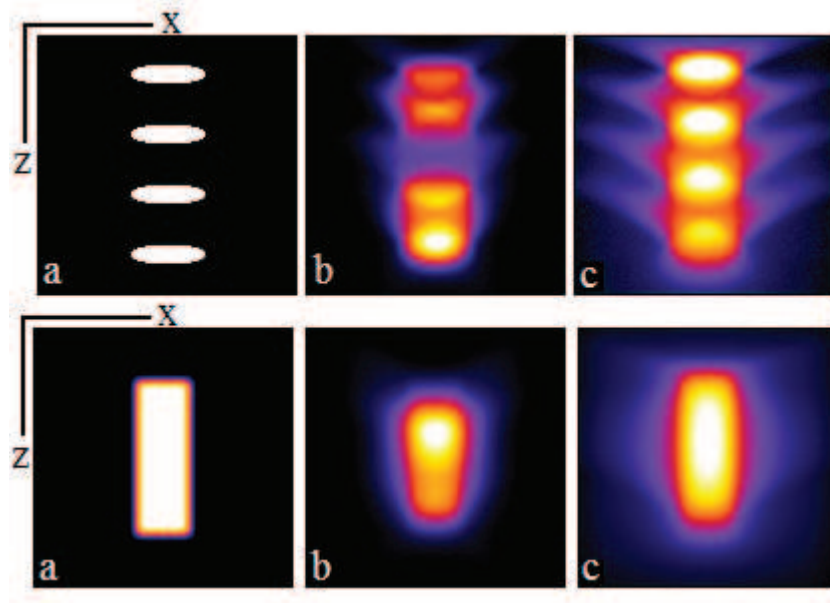


FIG. 4: RESULT OF EMMA DECONVOLUTION ASSOCIATED WITH LUCY-RICHARDSON USING 5 PSF WITH 20dB SNR (AT POSITIONS: 0, 10, 18, 25 AND 31.75 μm). a) ORIGINAL DATA, b) RESTORED IMAGES WITH EMMA, c) ACQUIRED IMAGES SIMULATION.

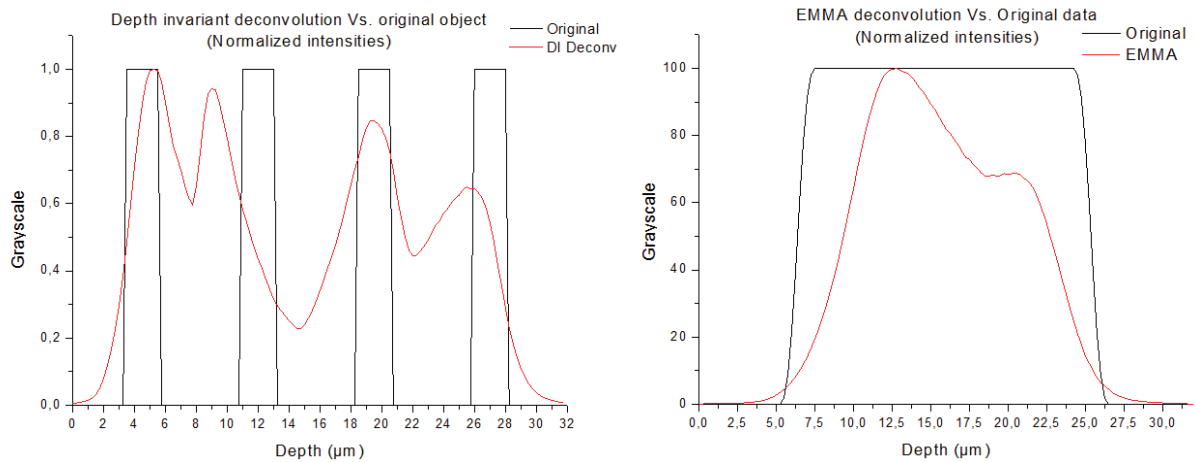


FIG. 5: NORMALIZED INTENSITIES PROFILES COMPARING EMMA DECONVOLUTION (5 PSF 20dB SNR) WITH THE ORIGINAL OBJECTS.

One can notice a slight amelioration of the deconvolution notably in beads separation and restoring the parallelepiped shape, but there are not ameliorations in restoring beads positions. This is due to the small number of PSF used, their positions and their low SNR. One should always keep in mind that EMMA results highly depend on the deconvolution algorithm and that high noise level into the data reduces the deconvolution performances. Furthermore, EMMA uses the intensities at the used PSF positions and interpolates the rest with linear weighted masks, so the used PSF positions have an important role in defining what features

are better restored. In this case, PSF at random positions were used and they don't emphasize a needed feature in general (eg. Beads positions), which better reflect a practical case.

In contrast to the previous case, to get a better result, one should provide more known PSF, at positions close to the regions of interests or may emphasize the needed features and also with high signal to noise ratio. To do so we provided Zernike interpolation algorithm that we will use to interpolate more PSF from the originally used 5 PSF (schematic represented in Fig. 6).

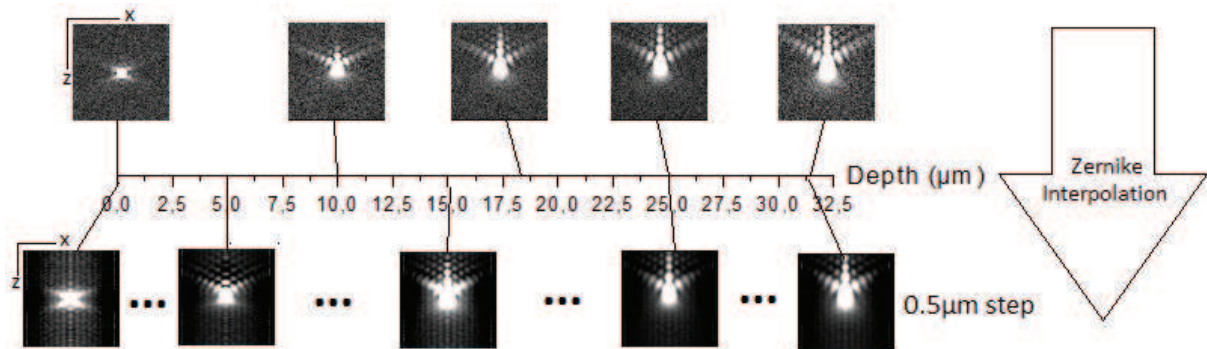


FIG. 6: ZERNIKE INTERPOLATION PROCESS USED (5 PSF AS INPUT, 64 PSF AS OUTPUT. ONE CAN NOTICE THE FILTERING EFFECT ON THE INTERPOLATED DATA.)

One can notice the filtering effect in the interpolated PSF (see chapter 3).

Fig. 7 shows the deconvolution result of EMMA associated with Lucy-Richardson algorithm and using the output data of Zernike interpolation shown above. A normalized intensities profiles comparison along the optical axis, between the deconvolution results and the original objects is shown at Fig. 8.

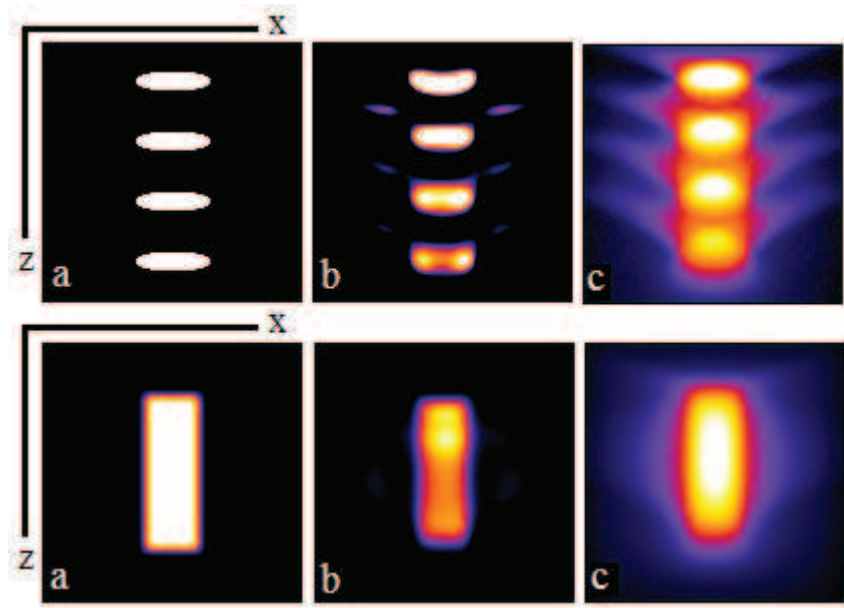


FIG. 7: EMMA DECONVOLUTION RESULT USING LUCY-RICHARDSON WITH PRIOR ZERNIKE INTERPOLATION (5 PSF AS INPUT - 64 PSF AS OUTPUT). a) ORIGINAL DATA, b) RESTORED IMAGES, c) ACQUIRED IMAGES SIMULATION.

One can easily notice a large amelioration in beads separation and their positions and dimensions restoration also a better restoration of the general shape of the parallelepiped.

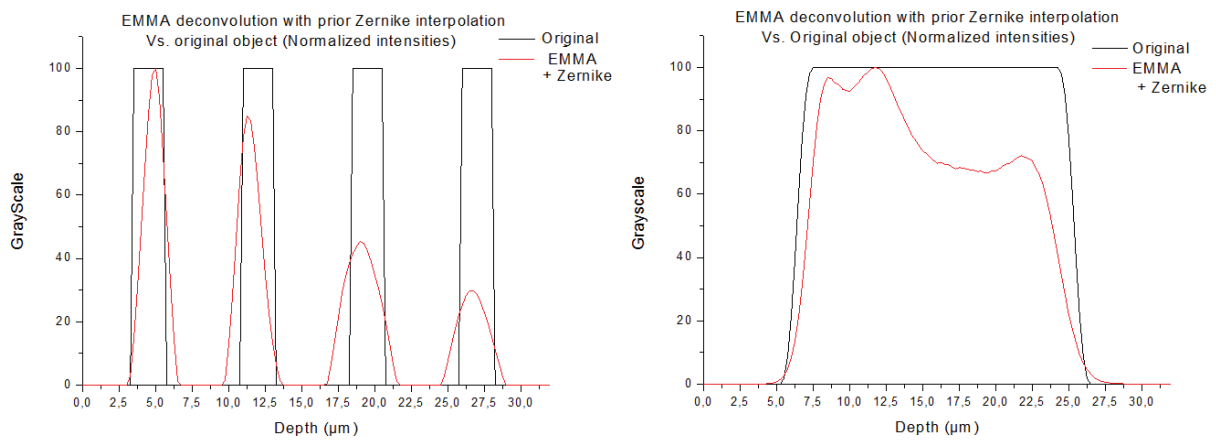


FIG. 8: NORMALIZED INTENSITIES PROFILES COMPARING AN EMMA DECONVOLUTION WITH PRIOR ZERNIKE INTERPOLATION WITH THE ORIGINAL OBJECT (5 PSF INPUT).

4.3. ACQUIRED DATA APPLICATION

4.3.1. SAMPLE PREPARATION

For this experimental part, a sample is prepared using fluorescent nano-beads (FluoSphere Molecular Probes) fixed into polymer over a depth up to $30\mu\text{m}$, the beads have 100nm of diameter and their emission wavelength is around 605nm . The manufacturing of such sample and its particularities are described in details in DE MEYER Arnaud thesis [1].

4.3.2. ACQUISITION

We are equipped with a wide field epi-fluorescence microscope based on an Olympus BX51, modified to acquire 3D images using computational optical sectioning. We use an oil immersed 100X objective with a numerical aperture of 1.4, mounted on a piezoelectric platform capable of moving along the optical axis in a range between $-50\mu\text{m}$ and $+50\mu\text{m}$, the axial step is set to be $0.25\mu\text{m}$. The images are captured using a cooled CCD (CoolSnap HQ²) camera having $6.45 \times 6.45\mu\text{m}$ pixels yielding a lateral resolution of $0.064\mu\text{m}$, and digitized using 14 bits-depth (16bits images); the full frame size is 1392×1040 . The system is controlled by a custom made program handling the 3D image acquisition and the synchronization between the illumination shutter and the camera's exposure time. This program has been developed during my thesis.

We acquired a full frame starting from the lowest point of the piezo range ($-50\mu\text{m}$) up to 128 slides ($0.25\mu\text{m}$ axial resolution). The Fig. 9 shows the acquired data volume, one can notice isolated beads (encircled with red) that can be used to extract multiple PSF at different depths and also aggregated beads (encircled with green) forming large structures that can be assimilated to cells phantoms. These extracted data is used to test Zernike interpolation, EMMA and EMMA-Zernike association.

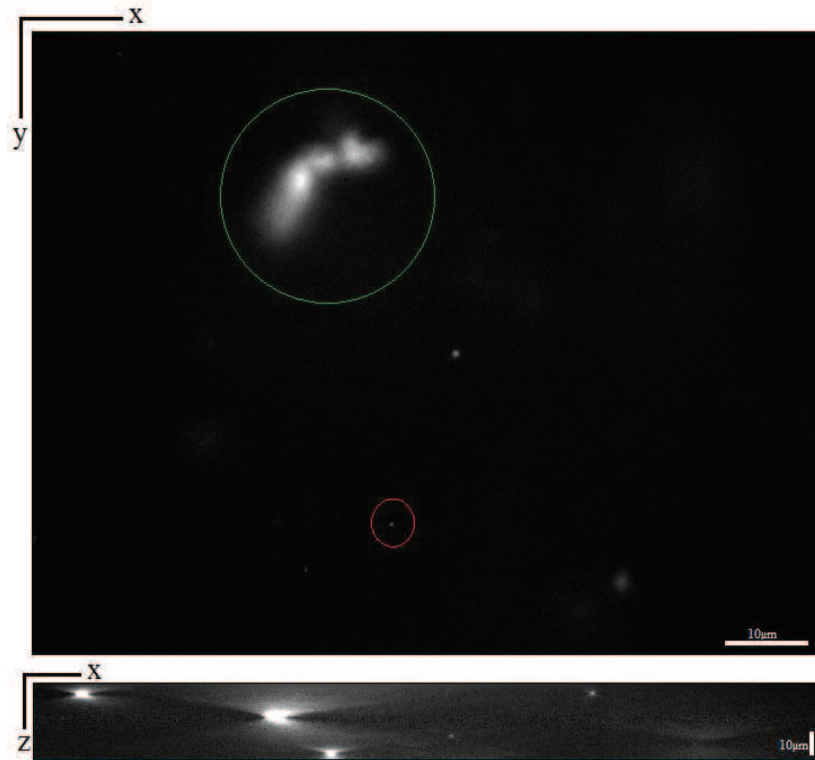


FIG. 9: ACQUIRED DATA SHOWING ISOLATED BEADS FOR PSF EXTRACTION (EX. RED CIRCLE) AND AGREGATES ASSIMILATED TO CELLS PHANTOMS (EX. GREEN CIRCLE).

4.3.2.1. OBJECT-LIKE AND POINT SPREAD FUNCTION EXTRACTION

The first Plane is considered as the relative origin of the depth (the relative $0\mu\text{m}$). Individual well separated beads are manually selected and 7 PSF has been extracted at relative depths 4, 8, 15.75, 18.25, 20.75, 22.75 and $25.75\mu\text{m}$ respectively, these PSF are centered in a $64 \times 64 \times 64$ voxels volume and then normalized. Fig. 10 shows 2 extracted PSF at depth $4\mu\text{m}$ (a-a') and $25.75\mu\text{m}$ (b-b') one can notice the change in elongation along the optical axis.

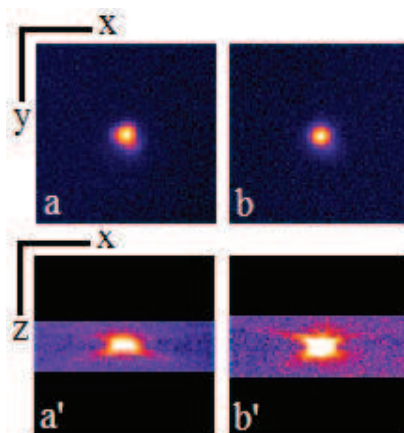


FIG. 10: EXTRACTED PSF AT RELATIVE DEPTH OF $4\mu\text{m}$ (a-a') AND $25.75\mu\text{m}$ (b-b').

In order to test EMMA deconvolution an aggregate of beads assimilated to cells phantom has been extracted in order to be deconvolved, this object is shown at Fig. 11.

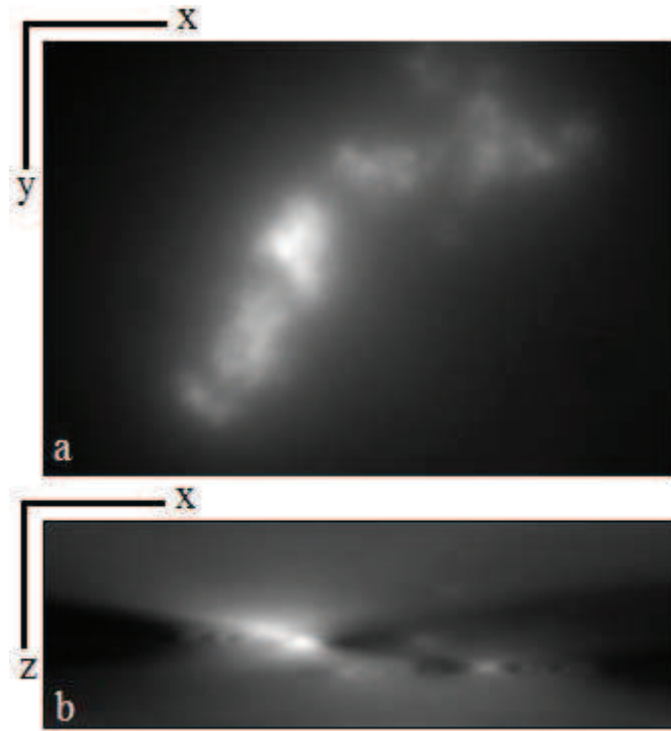


FIG. 11: THE EXTRACTED OBJECT, SHOWN AS AN AVERAGE INTENSITY PROJECTION ALONG THE Z AXIS (a) AND Y AXIS (b).

4.3.3. ZERNIKE INTERPOLATION TEST

In this section we test the efficiency of Zernike interpolation algorithm using acquired data. In order to do so 6 PSF are used and the 7th is interpolated then compared with the known one. This test is repeated twice, the first attempt we interpolated the PSF at 18.25 μm using the remaining PSF (4, 8, 15.75, 20.75, 22.75 and 25.75) and at the second attempt it is the PSF at 22.75 μm that is interpolated from the remaining ones (4, 8, 18.75, 20.75 and 25.75 μm). The interpolation uses 45 as maximum Zernike order and 5 as polynomial fitting order.

Fig. 12 shows the interpolated PSF at relative depth 18.25 μm (b-b') in comparison with the measured one at the same position (a-a'), one can see that the PSF is successfully estimated and present less noise than the measured one. This is also noticed in Fig. 13 showing the PSF interpolated at 22.75 μm (b-b') and the measured one at the same position (a-a').

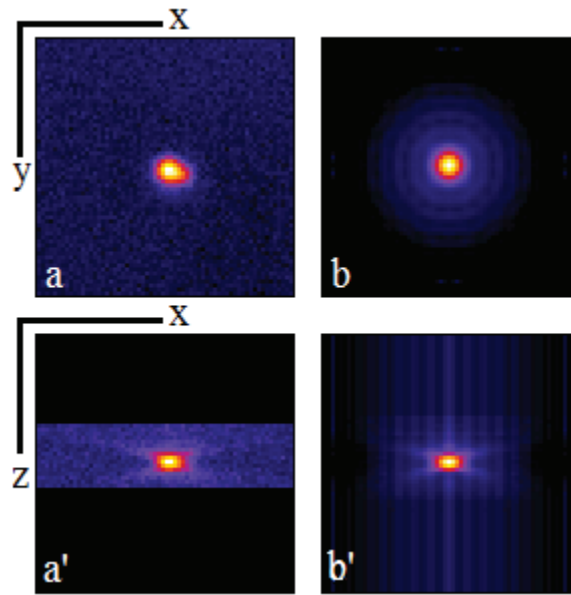


FIG. 12: INTERPOLATED PSF AT RELATIVE DEPTH $18.25\mu\text{m}$ (b-b') COMPARED TO THE MEASURED ONE AT THE SAME POSITION.

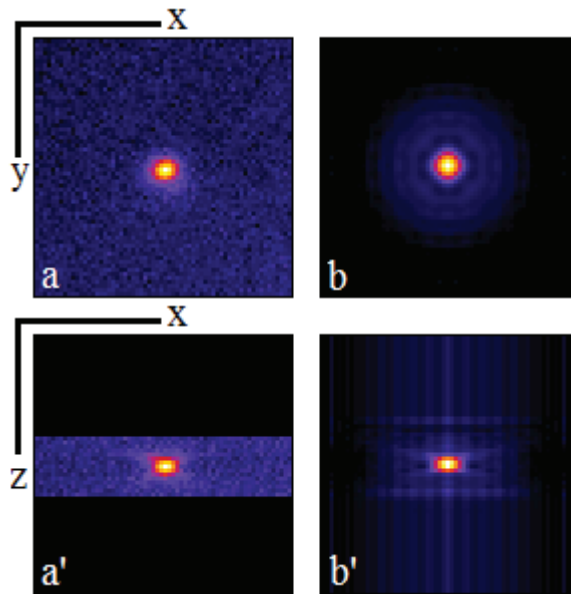


FIG. 13: INTERPOLATED PSF AT RELATIVE DEPTH $22.75\mu\text{m}$ (a-a') COMPARED TO THE MEASURED ONE AT THE SAME POSITION.

The Fig. 14 and Fig. 15 show intensity profiles comparing the interpolated PSF and the measured one at the same positions ($18.25\mu\text{m}$ and $22.75\mu\text{m}$ respectively). In each figure one can see a profiles passing by the center of the airy disc in the central plane of the PSF (left) and these along the optical axis passing by the center of the PSF. They demonstrate the quality of restoration of our interpolation algorithm as the background (essentially noise) is highly reduced and the PSF is well reshaped.

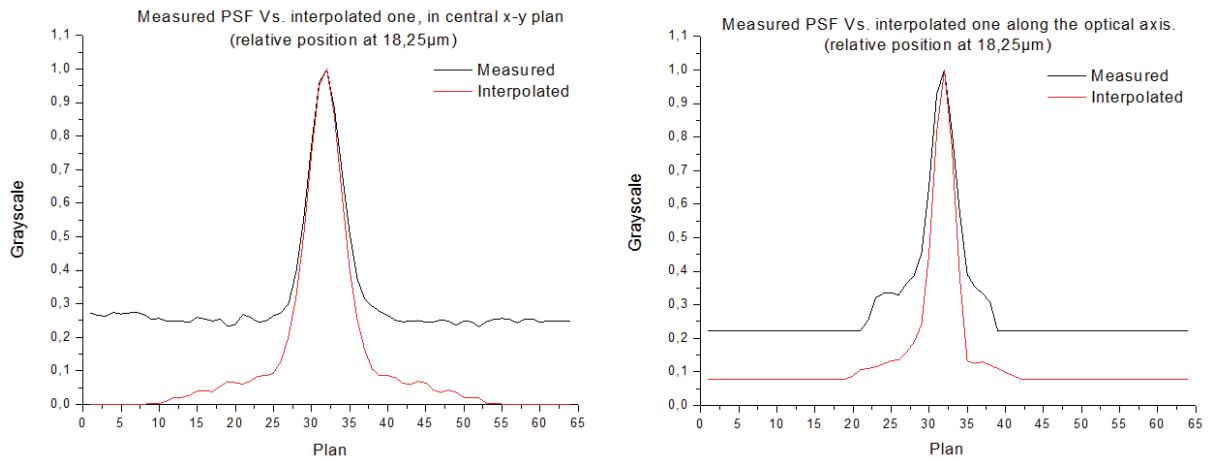


FIG. 14: INTENSITY PROFILES TRACED IN THE CENTRAL X-Y PLANE PASSING BY THE CETER OF THE AIRY DISK (LEFT) AND ALONG THE OPTICAL AXIS PASSING BY THE CENTER OF THE PSF (RIGHT), COMPARING THE MEASURED PSF AT THE RELATIVE POSITION $18.25\mu\text{m}$ AND THE INTERPOLATED ONE AT THAT POSITION.

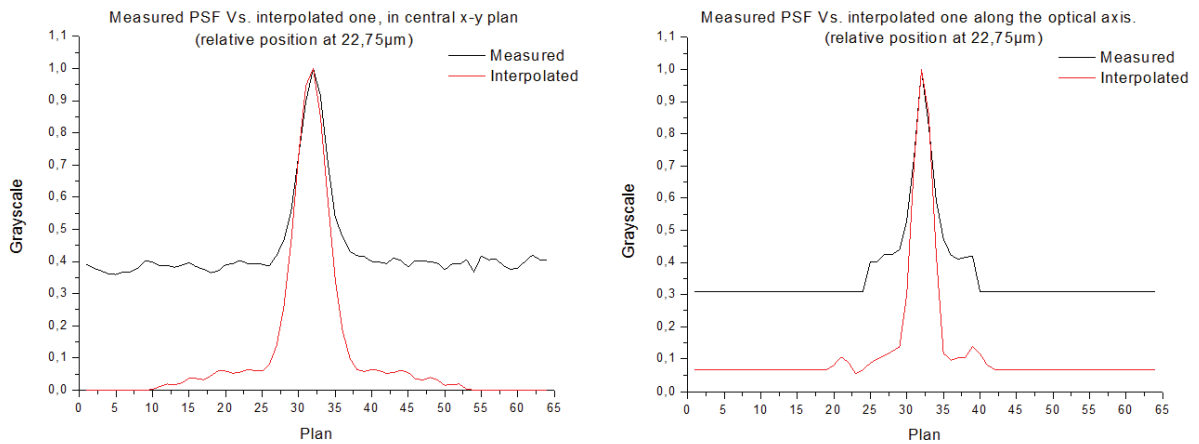


FIG. 15: INTENSITY PROFILES TRACED IN THE CENTRAL X-Y PLANE PASSING BY THE CETER OF THE AIRY DISK (LEFT) AND ALONG THE OPTICAL AXIS PASSING BY THE CENTER OF THE PSF (RIGHT), COMPARING THE MEASURED PSF AT THE RELATIVE POSITION $22.75\mu\text{m}$ AND THE INTERPOLATED ONE AT THAT POSITION.

Each resulting PSF match the experimental corresponding one with a filtering effect. These PSF are suitable to be used with EMMA. In the next section the measured PSF will be used first in an EMMA deconvolution, and then the interpolated one will be used.

4.3.4. IMAGE RESTORATION TESTS

In this section a restoration process is performed over the object extracted before and assimilated to a cells phantom. In order to present the 3D results in a convenient way in this manuscript and as the object spreads over multiple depths, we decide to represent the volumes as an intensity average projection along the optical axis and along the y axis. The results are shown using the ImageJ's "fire" LUT to emphasis low intensities details. A 3D view using ImageJ 3D Viewer [2] is also shown in a surface view mode.

To have an estimate of the noise in the image the following formula is used:

$$SNR = 20 \log_{10} \frac{\mu_{sig}}{\sigma_{bkg}} \quad (4.1)$$

Where μ_{sig} is the signal's mean and σ_{bkg} is the standard deviation in the background (representation of the noise). Applying equation (4.1) on the acquired image, and SNR of 20.24dB is obtained. Fig. 16 shows the histogram of the acquired image background (signal free slice) – one can notice that the noise have a Poisson statistics but it can be considered as Gaussian distribution.

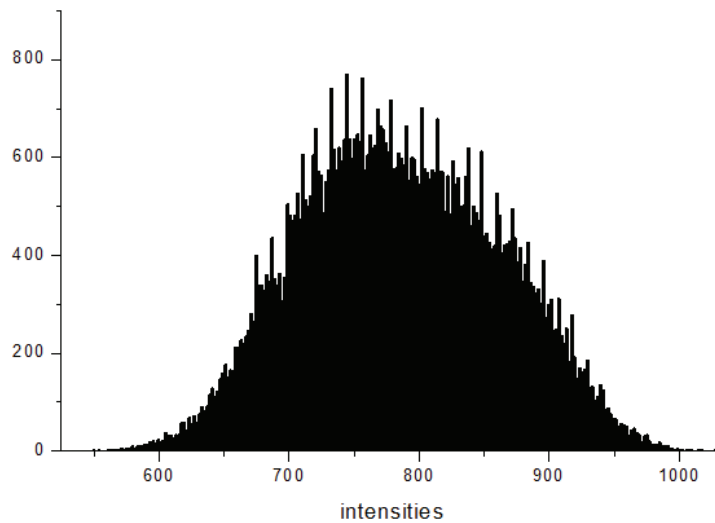


FIG. 16: HISTOGRAM OF THE ACQUIRED IMAGE BACKGROUND (SIGNAL FREE SLICE) – ONE CAN NOTICE THAT THE NOISE STATISTIC CAN BE CONSIDERED AS GAUSSIAN DISTRIBUTION.

The deconvolution algorithm chosen is the LLS algorithm described in the first chapter, all the result receive a same post-treatments in order to eliminate the noise, the rebound and ringing effect of LLS algorithm and all deconvolution attempts use the same regularization parameter.

The post-treatments are described as follow:

- Background removal is applied; all voxel intensities under the threshold value are set to zero. The threshold is estimated from a signal free zone.
- A median filter is then applied having a radius of 1 single pixel in order to eliminate the one pixel artifacts.

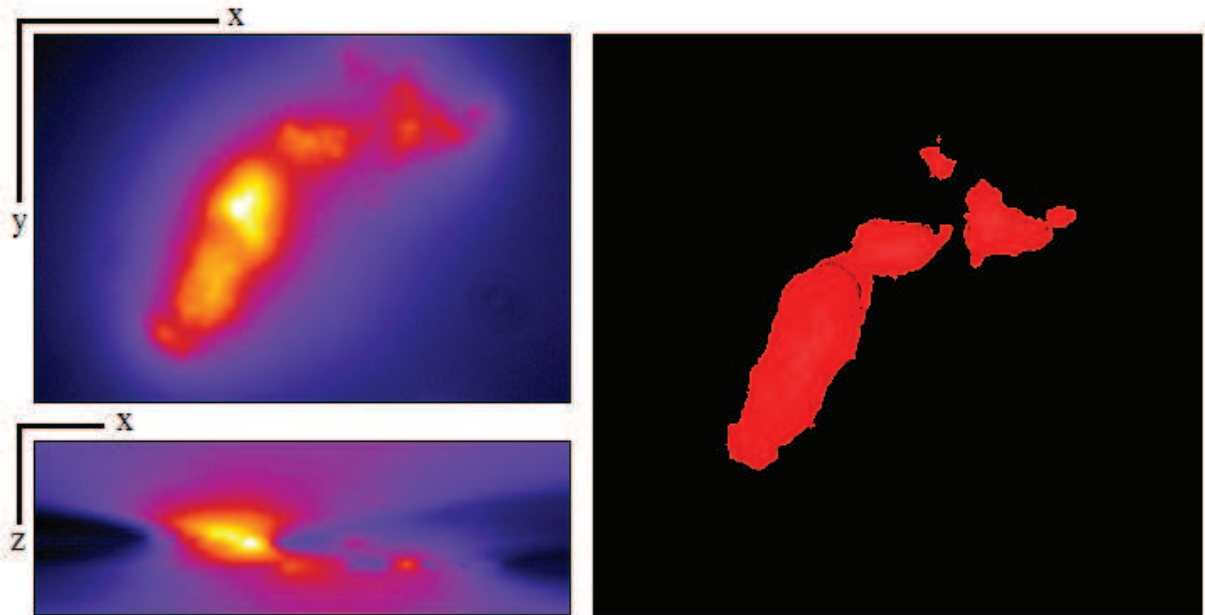


FIG. 17: THE ORIGINAL OBJECT (EXTRACTED) SHOWN IN INTENCITY AVERAGE PROJECTION MODE (LEFT) AND 3D SURFACE VIEW MODE (RIGHT).

Fig. 17 shows the extracted object in both modes described above.

4.3.4.1. NON-INVARIANCE DECONVOLUTION

As a reference, we perform a 3D deconvolution using LLS algorithm implemented as ImageJ plugIn. The measured PSF at relative depth of $25.75\mu\text{m}$ is used as the non-invariant PSF of the system.

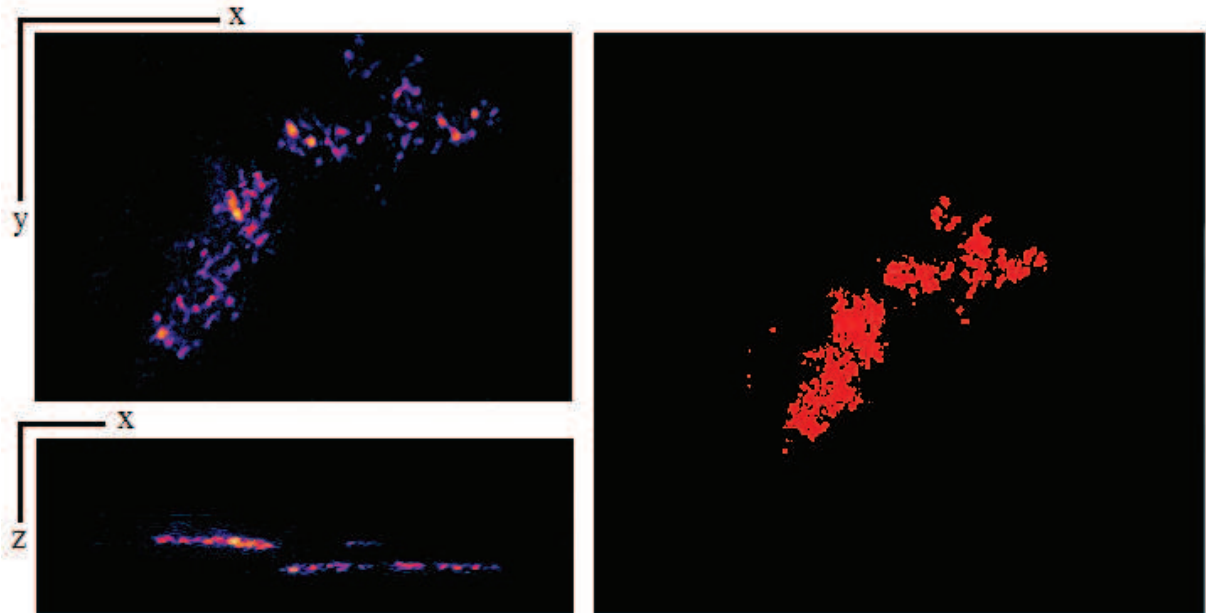


FIG. 18: RESULT OF A DECONVOLUTION USING LLS IN A PSF NON-INVARIANCE ASSUMPTION.

Fig. 18 shows the result of a deconvolution using LLS algorithm with PSF's non-invariance assumption. As we know that the object is a collection of nano-beads, the ideal restoration would be a spots arrangement of 200nm laterally and 600nm axially (the missing cone limits the restoration). However in this result we can notice that the beads still aggregated in smaller groups that get thicker as we get far from the used PSF (going up) due to the change in the PSF.

4.3.4.2. EMMA DECONVOLUTION

EMMA is associated in this section with the LLS algorithm and using the 7 PSF acquired along the depth (see acquisition section).

Fig. 19 shows the result of such deconvolution, one can easily notice a better separation of the beads. By examining the two set of beads, we can see that the beads are more or less equally restored along the depth.

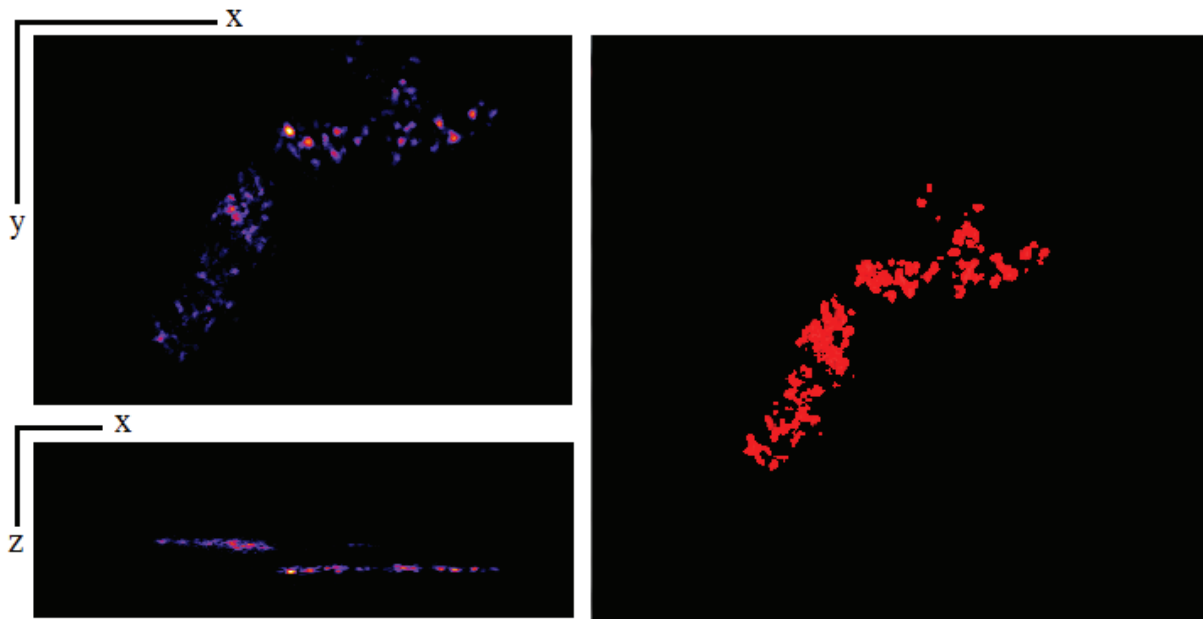


FIG. 19: RESULT OF EMMA DECONVOLUTION ASSOCIATED WITH LLS ALGORITHM USING 7 ACQUIRED PSF (4, 8, 15.75, 18.25, 20.75, 22.75 AND 25.75 μm).

In order to have a better restoration, Zernike interpolation is used in the next section, to interpolate and use more PSF equally spread along the depth and having a better SNR.

4.3.4.3. EMMA WITH ZERNIKE INTERPOLATION

In this section Zernike interpolation is used to generate 23 PSF starting from relative depth of $4\mu\text{m}$ till $25.75\mu\text{m}$ with $1\mu\text{m}$ step (4, 5, 6, 7, 8, 9, 10, 11, 12, 13, 14, 15, 16, 17, 18, 19, 20, 21, 22, 23, 24, 25 and $25.75\mu\text{m}$). These interpolated PSF are used with EMMA-LLS algorithm to perform the restoration.

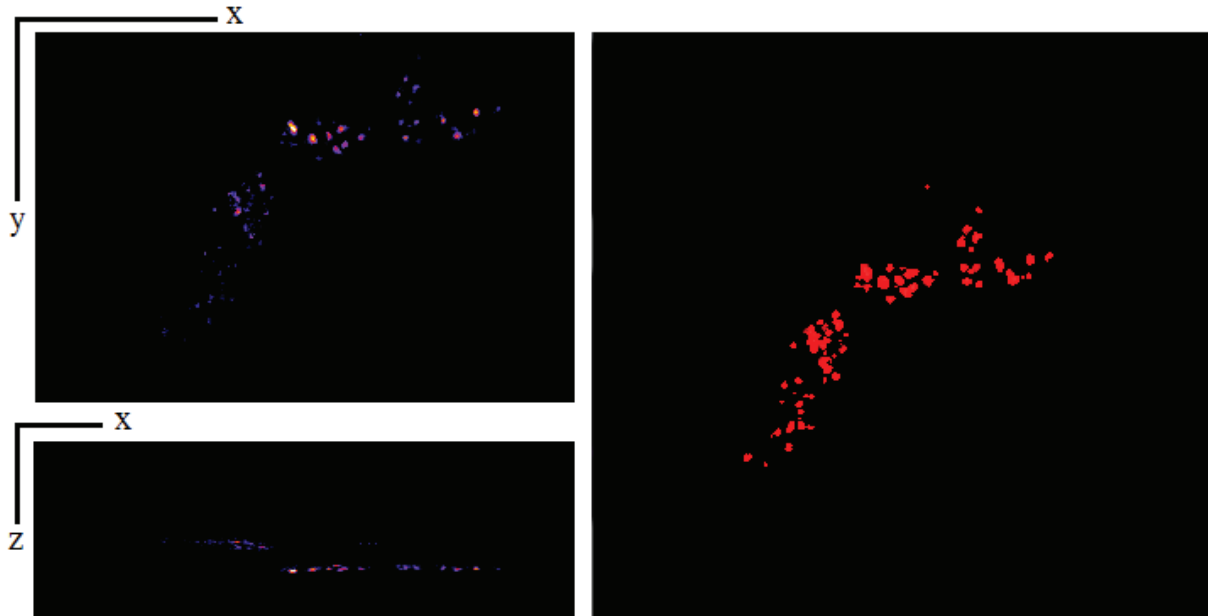


FIG. 20: DECONVOLUTION RESULT USING EMMA ASSOCIATED WITH LLS ALGORITHM AFTER USING ZERNIKE INTERPOLATION TO PRODUCE 23 PSF WITH $1\mu\text{m}$ STEP.

Fig. 20 shows the result of such deconvolution, one can see a larger amelioration of beads separation and equal restoration along the depth.

4.4. CONCLUSION

In this chapter, EMMA was associated with Zernike interpolation process and the entire solution was validated over simulation and experimental data.

PSF at various depths were acquired using a special sample manufactured with nano-beads fixed into a polymer, these beads were used to validate the Zernike interpolation process, where interpolated PSF were compared with the measured one.

Cells phantom-like object were extracted from the same sample as the PSF and were used to validate EMMA and EMMA-Zernike solution, where qualitative comparisons were used and better and homogenous resolution have been obtained along the optical axis.

Finally the EMMA-Zernike solution was implemented as ImageJ PlugIn associated with LLS and Lucy-Richardson algorithms. The PlugIn will be published on ImageJ website soon, after implementation of few performance ameliorations.

5. CONCLUSION AND PERSPECTIVES

This manuscript resumes three years work over fluorescence microscopy deconvolution thematic, one of the main fields in MIPS laboratory [1] [5][12]. This thesis was financed by “region Alsace” and continues previous works in image and signal processing applied to microscopy. This work is linked to the microscopist international community and offers many contributions in GDR [2][3][7][8][10] (Groupe de Recherche) “microscopie fonctionnelle du vivant” , ImageJ users and developers community and a MIPS project entitled “Imagerie en Microscopie Multidimensionnelle et Systèmes d’information” which aims to include the entire image acquisition and treatment process in a single automated tool.

The thesis objective being a practical solution for the 3D deconvolution under PSF non-invariance conditions through depth. As matter of fact the existing method up till now, in our knowledge, are limited to specific cases. We proposed a more general approach that can be applied to all deconvolution methods even with a limited number of measured PSF set.

In this manuscript, we started with a review over hardware amelioration methods in fluorescence microscopy followed by an overview of the deconvolution methods and their classification. As a contribution to the microscopy community, 3D Lucy-Richardson and LLS methods were implemented as ImageJ plugins [6] using JNI (Java Native Interface) in combination with native shared libraries (this work won the first prize in ImageJ users and developers conference 2008).

Afterward, an approach for space variant PSF deconvolution has been presented; it has been applied on depth variant PSF case that is especially noticeable when observing thick specimens using wide field fluorescence microscopy. The originality of this work is by proposing an algorithm [4][13] (EMMA) capable of transforming any classical deconvolution algorithm using the invariant assumption into a depth variant PSF deconvolution solution. Furthermore EMMA adapts itself to use any available input data in terms of number of known PSF and their positions. For validation purposes, EMMA was associated with Lucy-Richardson and LLS algorithm to perform depth variant PSF deconvolution over simulated data, with and without noise presence, in order to study robustness and accuracy gain in quantitative measurements.

It has been shown that the restored image quality highly depend on the number of PSF used by the process. However, in practical application, PSF measurement techniques may only offer a limited

Conclusion and perspectives

number of randomly positioned PSF. Thereby, in order to obtain more when a limited set of measured PSF is acquired, we present an interpolation algorithm based on Zernike moments and polynomial fitting. Zernike moments are used as image descriptors. The method was tested on synthetic data with and without noise for validation purposes. In addition to depth variant PSF interpolation our method may be used with others optical setting variations; the case of immersion oil refractive index change induced by temperature was presented as an example. An ImageJ plugin is developed, it include the interpolation process, PSF decomposition and re-composition using Zernike moments and moments variation tracer, enabling the user to visualize these variations for each moment.

In the final chapter, Zernike interpolation was tested over measured data and a combination of both algorithms was applied on acquired data using few extracted PSF. 100nm fluo-beads imbedded in polymers were used to extract some PSF at various depths and a cells-phantom like object was extracted. The PSF were used to validate the Zernike interpolation process, which is later associated with EMMA algorithm and the entire solution is then validated over simulated and measured data. A qualitative comparison was performed showing the success of EMMA algorithm and the better resolution obtained from the EMMA-Zernike association.

However, the presented study let appear that further PSF descriptors improvements can be discussed. For example, new approaches propose the use of discrete orthogonal moment based on Tchebichef, Hahn or Racah polynomials in place of continuous orthogonal moments as these based on Zernike or Legendre polynomials, these polynomials set can yield better image reconstruction with less computational effort. In future work we will investigate these possibilities in order to ameliorate our interpolation technique for better interpolated PSF quality.

In addition, some other possibilities to continue this work take place in the context of the DIAMOND project in which our laboratory participates dynamically and is supported by the ANR. The DIAMOND project purposes are the enhancement of deconvolution process for multi-dimensional microscopy, taking into account the sample effect on image formation and novel imaging systems like the Macroscope.



FIG. 1: PSF SET ACQUIERED USING A MACROSCOPE

The macroscope presents severe variations in the PSF in all three directions, especially in the XY plane (Fig. 1). To correct the images acquired with such device one must take in consideration these variations in the deconvolution process. We will study the possibility of adapting the interpolation process for the macroscope PSF. First, the PSF variation can be consider in a cylindrical coordinate

Conclusion and perspectives

and decomposed in successive interpolation steps along each coordinate variable. Then we can modify EMMA's masks to handle these 3D variations. Furthermore, EMMA may be adapted for blind deconvolution algorithms but the process would be time consuming, we consider studying this case and try to optimize our algorithm to be a solution for depth variant blind deconvolution.

As a conclusion, the presented work offers a complete framework from the sample preparation, PSF and sample imaging, to the signal processing methods. This framework is a shared tool distributed to the microscopist community as ImageJ plugins. Computational enhancement for EMMA could be the amelioration of implementation discussed in chapter 2 and propose to the scientific community a multithreaded ImageJ plugin taking advantage of multiple core computers. One also may consider the possibility of integrating jCUDA into our plugin allowing the use of Nvidia GPU from ImageJ.

SCIENTIFIC WORKS

INTERNATIONAL CONFERENCES

- [1]. A. DIETERLEN., O. HAEBERLÉ, M. DEBAILLEUL, V. GEORGES, B. SIMON, B. COLICCHIO, A. DE MEYER, E. EL MAALOUF, M. SARMIS
« Some new techniques and advances in 3-D fluorescence microscopy »
Correlation Optics 2009, 20-24 September 2009 Chernivtsi Ukraine
- [2]. E. EL MAALOUF, B. COLICCHIO, AND A. DIETERLEN,
« Fast deconvolution with non-invariant PSF for 3-D fluorescence microscopy »
Photonics Europe 2008, Strasbourg, April 7-11 (2008)
Proc. SPIE 7000, 70001K-70008 (2008)
- [3]. E. EL MAALOUF, B. COLICCHIO, AND A. DIETERLEN,
« 3d thick samples deconvolution in fluorescence microscopy with non-invariant psf » 2011 IEEE international symposium on biomedical imaging, Chicago USA, 30 march -2 april 2011(submitted)
-

NATIONAL CONFERENCES

- [4]. E. EL MAALOUF, B. COLICCHIO, A. DIETERLEN
« Déconvolution d'échantillons biologique 3D épais en microscopie de fluorescence par PSF non invariante »
Colloque Imvie5, Mulhouse 9-10 juin 2009 (CD-ROM)
- [5]. E. EL MAALOUF, L. BALAN, B. COLICCHIO, A. DIETERLEN
« Optical microscopy tool to analyse nanoparticules embedded in photopolymers »
Colloque Imvie5, Mulhouse 9-10 juin 2009 (CD-ROM)
-

POSTERS

- [6]. E. EL MAALOUF, B. COLICCHIO, A. DIETERLEN
« Increase ImageJ plugin performance by using JNI (Java Native Interface) »
ImageJ User and Developer Conference 2008 (6 novembre 2008 - 07 novembre 2008) à Luxembourg
Prix du meilleur Poster.
- [7]. E. EL MAALOUF, B. COLICCHIO, A. DIETERLEN
« Apport à la résolution du problème de la non-invariance spatiale de la PSF en microscopie de fluorescence »
Ecole thématique interdisciplinaire en Microscopie FONctionnelle en BIOlogie (mifobio) du 19 au 25 septembre 2010 à Seignosse
- [8]. E. EL MAALOUF, B. COLICCHIO, A. DIETERLEN
« Fast deconvolution with non-invariant PSF for 3-D fluorescence microscopy »
Présentation à l'école thématique interdisciplinaire en Microscopie FONctionnelle en BIOlogie (mifobio) . (21 au 26
Septembre 2008) à Carqueiranne
- [9]. E. EL MAALOUF, B. COLICCHIO, A. DIETERLEN
« Pseudo-3D Zernike moments applied on point spread function interpolation »
Workshop Zernike Polynominals and beyond, Institut d'Optique 6 et 7 mai, Palaiseau (France)
- [10]. E. EL MAALOUF, B. COLICCHIO, A. DIETERLEN
«3D Fluorescence imagery treatment »
Présentation à la conférence « Les Rencontres Alsaciennes d'Imagerie en Biologie » le 17 décembre 2009
-

PUBLICATIONS

- [11]. E. EL MAALOUF, B. COLICCHIO, A. DIETERLEN
"Fluorescence microscopy 3D depth variant PSF analysis and interpolation using Zernike Moments"
Optics Express (submitted juin 2010)
- [12]. E. EL MAALOUF, L. Balan, A. Dieterlen
Optical microscopy tool, to analyse nanoparticules embedded in photopolymers
Optices Letter (submitted janvier 2010)
- [13]. E. EL MAALOUF, B. COLICCHIO, A. DIETERLEN
"The "EMMA" solution for the depth variant PSF deconvolution in 3-D fluorescence microscopy." (to be submitted)